8-2013

# Complex magnetism in noncentrosymmetric magnets

Nirmal Jeevi Ghimire
nghimire@utk.edu

To the Graduate Council:

I am submitting herewith a dissertation written by Nirmal Jeevi Ghimire entitled "Complex magnetism in noncentrosymmetric magnets." I have examined the final electronic copy of this dissertation for form and content and recommend that it be accepted in partial fulfillment of the requirements for the degree of Doctor of Philosophy, with a major in Physics.

David Mandrus, Major Professor

We have read this dissertation and recommend its acceptance:

Takeshi Egami, Elbio Dagotto, Stephen E. Nagler

Accepted for the Council:

Carolyn R. Hodges

Vice Provost and Dean of the Graduate School

(Original signatures are on file with official student records.)

# Complex magnetism in noncentrosymmetric magnets

A Dissertation Presented for the

Doctor of Philosophy

Degree

The University of Tennessee, Knoxville

Nirmal Jeevi Ghimire

August 2013

*Dedicated to my parents.*

# Acknowledgements

I would like to express my thank and appreciation to my thesis advisor Dr. David Mandrus who made this research possible. I found him to be an excellent advisor. He not only supervised me in conducting the research, but also provided every available opportunity in developing my overall skills. He provided me an independent research environment, yet providing support and suggestions at the time of need. I highly appreciate his time and trust in me. My sincere thank goes to Dr. Michael McGuire. I would like to thank him for teaching me all the synthesis and measurement techniques, discussion, support and guidance throughout my Ph.D research. Thank you for your supervision in the rare earth free permanent magnet project.

Many thanks to Dr. Brian Sales for his support, guidance and enthusiastic discussions and inspiration. I would like to express my thank to Dr. Stephen Nagler for his time, suggestions and guidance in carrying out the neutron scattering experiments. Special thanks to Dr. Jiaqiang Yan for sharing his expertise to help me with single crystal growth techniques.

Many thanks to my collaborators Dr. David Parker, Dr. Veerle Keppens and Dr. Michael Koehler. Thanks to Dr. Adam Aczel for the collaboration, useful discussion and help during the neutron scattering experiments. Thanks to Dr. Lisa Debeer-Schmitt for the wonderful help during the small angle neutron scattering experiments. Also, thanks to Dr. Brian Chakoumakos and Dr. Huibo Cao for their help and support during the experiments at HB-3A. Thanks to Dr. Andrew May for good physics discussion and help in the lab.

Many thanks to my lab mates over the years especially Yuen Yiu, Amal Al-Wahish, Siwei Tang, Lekhnath Poudel, Jieyu Yi, Ling Li and Isaac Bredeson for their help and good company in the lab. Thanks to Doug E. Fielden and Carol Winn for their technical help during the lab set up.

I would like to express my thank to my committee members Dr. Takeshi Egami and Dr. Elbio Dagotto for their time and useful suggestions. I would also like to thank Dr. Marianne Breinig for her helpful advice throughout my graduate studies at the University of Tennessee.

Finally, I would like to thank my wife, Pramila Sharma, for her constant support and inspiration throughout the years. Along with Pramila, I would also like to thank my parents for their love and support and my little daughter Nioma for her beautiful smiles.

# Abstract

Broken inversion symmetry in a crystal lattice allows an extra term called the Dzyaloshinskii-Moriya (DM) interaction in the magnetic Hamiltonian. The DM interaction tends to align spins in perpendicular orientation and therefore competes with the exchange interaction that favors collinear spins. This competition results in different modulated chiral magnetic structures depending on the relative strength of the two interactions. Skyrmion, soliton and magnetic blue phases are some of the anticipated structures. This dissertation extends the search for these exotic magnetic structures using various techniques to study the magnetism in the noncentrosymmetric magnets $Cr_{11}Ge_{19}$ [chromium eleven germanium nineteen], $Cr_{1/3}NbS_2$ [chromium one-third niobium disulphide] and $K_2V_3O_8$ [fresnoite-type potassium vanadate].

Experimental investigations of magnetic, thermal, structural and elastic properties of $Cr_{11}Ge_{19}$ indicate complex itinerant ferromagnetism, evidence of spin wave excitations, and strong magnetoelastic coupling in this material. First principles calculations support the presence of itinerant ferromagnetism and suggest a noncollinear ground state may be expected. In the chiral helimagnet $Cr_{1/3}NbS_2$ the magnetic transition is found to strongly affect the electrical transport. Spin reorientation from the helimagnetic ground state to the commensurate ferromagnetic state is evident in the magnetoresistance. Neutron scattering is used to demonstrate the change in the periodicity of the incommensurate structure and the eventual incommensurate to commensurate transition, in accordance with the theoretical prediction of the soliton

model. The tetragonal easy axis antiferromagnet $K_2V_3O_8$ has been investigated by DC magnetization, AC susceptibility and heat capacity measurements. Based on the comparison of the behaviors observed in these measurements with other well-studied chiral helimagnets, the existence of two different spiral structures – one parallel and one perpendicular to the $c$ axis – is proposed.

# Table of Contents

# List of Tables

# List of Figures

# Chapter 1

# Introduction

With the advancement of present day technology, energy consumption is posing a major problem and there is a great deal of effort to address this issue. Basic science research must be a part of it and hence one of the themes in modern day condensed matter physics has been to address the issue of energy in one way or another. This dissertation, in a broad sense, incorporates this view with the main focus on the underlying physics of novel magnetic materials. The approach adopted is to find new magnetic materials or new magnetic properties. Discovery of new materials or new phenomena opens avenues for testing and verification of existing theories and hypotheses as well as providing direction to possible technological applications. Giant magnetoresistance [1, 2] is a recent example. However, the search, of course, is never easy. Nonetheless, one can develop heuristics that can help point us in the right direction. But still, the search has to be guided by certain principles.

The idea adopted for the search for new materials/phonomena in this dissertation is to look into classes of materials with multiple competing interactions. We can, for illustration, visualize a picture of a multi-way tug of war. An external stimulus applied to even the weakest team, can change the outcome of the game. Likewise, in a system with multiple competing interactions, external parameters such as temperature,

magnetic field, pressure etc., can enhance (or suppress) the effect of one of the interactions and therefore allows possible tuning of properties.

Since our focus is magnetism, we need to find a system with multiple competing magnetic interactions. Noncentrosymmetric magnets fall well within this criteria.

## 1.1 Noncentrosymmetricity

A noncentrosymmetric crystal is a crystal that lacks an inversion center. The presence or absence of a center of symmetry is indicated by the symmetry group of the crystal. It turns out that out of 230 space groups (or 32 point groups) more than half (138 space groups, 21 point groups) lack an inversion center (see Appendix A). Some of the noncentrosymmetric point groups also lack reflection through a plane and roto-inversion symmetry, and thus are non superimposable by pure rotation and translation on its image formed by inversion through a point. These are called chiral point groups [3]. Eleven point groups (65 space groups) are chiral. When the object is superimposable by pure rotation and translation on its inverted image, the object is called achiral. It is to be noted that all the chiral structures (point groups) are noncentrosymmetric but all the noncentrosymmetric structures are not chiral. The relevance of noncentrosymmetricity and chirality here is that a special magnetic interaction called the Dzyaloshinskii-Moriya (DM) interaction (see section 1.2.2) is allowed in all noncentrosymmetric materials but a novel spin structure called skyrmion (see sections 1.3 and 2.3), believed to have root origin to the DM interaction, has been observed, so far, in the materials belonging to only one space group ($P2_13$) that is chiral.

## 1.2 Magnetism and magnetic interactions of interest

The origin of magnetism lies in the orbital and spin degrees of freedom of electrons and their interaction with one another. Each electron has an orbital angular momentum ($l$) and a spin angular momentum ($s$) and their associated magnetic moments. The total angular momentum $J = L + S$ is the sum of the combined sum of orbital angular momentum of all the electrons ($L = \sum l$) and the combined sum of the spin angular momentum ( $S = \sum s$) of all electrons. The Pauli exclusion principle dictates the arrangement of the spins in an orbital, according to which, a maximum of two electrons may occupy each atomic orbital and the two electrons in the same atomic orbital must always have opposite spins. As a result, completely filled orbitals do not have a net magnetic moment as the magnetic moments of up and down spins cancel each other. At the same time, the filling of orbitals by electrons is guided by Hund's rules which state 1) electrons maximize their total spin $S$, meaning that electrons will occupy orbital with one electron per orbital and all the spins parallel until the orbitals contains one electron each. 2) For a given spin arrangement, the configuration with the largest atomic angular momentum $L$ lies lowest in energy. 3) For atoms with less than half filled shells, the lowest energy electronic configuration is the one with the lowest value of $J$. For the case of more than half filled shells, J is maximized. Therefore, the transition metal elements with partially filled $3d$ and $5d$ shells and the lanthanide and actinide elements with partially filled $4f$ and $5f$ shells, respectively, bear the magnetic moments. In a crystalline environment the orbital angular momentum in transition metals is usually quenched ( i.e. $L \approx 0$) whereas the orbital angular momentum is non zero in lanthanides and actinides. Both orbital and spin components contribute to the magnetic moment in these materials.

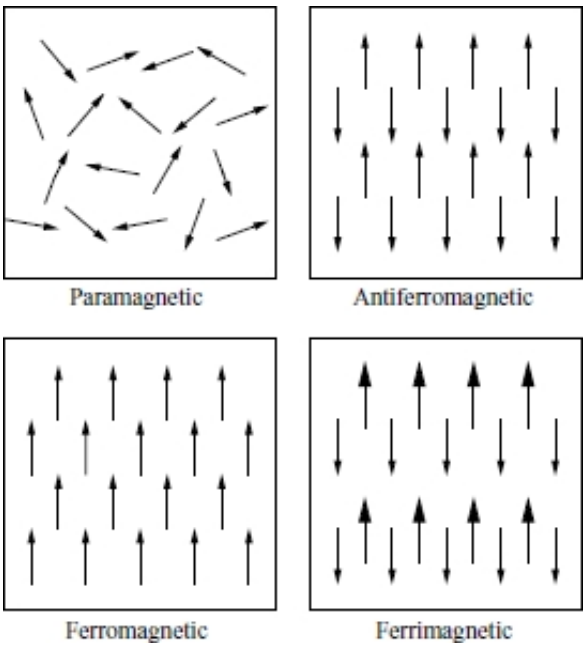


**Figure 1.1:** Ordering of magnetic moments in some common magnetic materials, after Spaldin [4].

Magnetic materials are usually classified by their response to an external magnetic field. On the fundamental level the magnetic materials can be categorized into two types: diamagnetic and paramagnetic. All other complex magnetic behaviors evolve from these basic magnetic phenomena. Diamagnetic substances are characterized by an antiparallel arrangement of the induced moments with applied magnetic field. Diamagnetism arises from the interaction of the applied field with the orbitals containing paired electrons and is a property of all matter. Paramagnetic materials, on the other hand, are characterized by a parallel arrangement of the induced moments with applied magnetic field. Paramagnetism arises due to the interaction between magnetic field and unpaired electrons in atomic or molecular orbitals. Ferromagnetism, ferrimagnetism and antiferromagnetism are the common ordered magnetic states (see Fig. 1.1). Some basic types of modulated magnetic structures include simple spiral (SS), ferromagnetic spiral (FS), skewed spiral ($\widetilde{SS}$), longitudinal spin wave (LSW), transverse spin wave (TSW) and fan structure (FAN), that occurs

only in a magnetic field [5]. These structures are depicted in Figure 1.2. The simple spiral is also know as a helical structure. Above a critical temperature all of these common and modulated magnetic structures show paramagnetism. For a material to be in a magnetically ordered state the magnetic moment on one atom must be coupled to the moment on neighboring atom. The spin coupling can occur through different interactions.

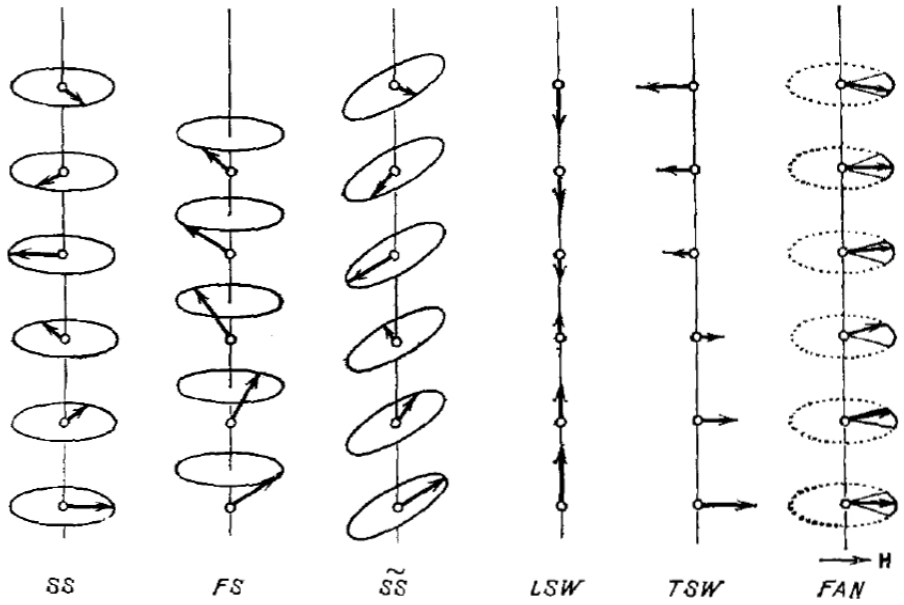


**Figure 1.2:** Basic types of modulated magnetic structures. The arrows indicate the orientation of the magnetic moments (spins). All atomic spins, in a plane, are collinear. Their orientation changes from one plane to another and the phase difference between two neighboring planes is always constant, after Izyumov [5].

### 1.2.1 Exchange interaction

The exchange interaction between two spins is a purely quantum mechanical term proportional to the dot product of the corresponding spin operators. For a single pair, the Heisenberg Hamiltonian is:

$$H_{exc} = -J\mathbf{S}_1 \cdot \mathbf{S}_2, \tag{1.1}$$

where $\boldsymbol{S}_i$ ($i = 1, 2$) is the spin operator located at the lattice site $i$ and $J$ represents the strength of the exchange interaction (also called the exchange constant or coupling constant). The sign of $J$ determines the relative spin orientation. A negative sign of $J$ favors the parallel arrangement of spins and hence a ferromagnetic coupling. Whereas, a positive $J$ results in the antiparallel arrangement of spins with the resultant antiferromagnetic coupling. The interaction represented by equation 1.1 does not require an intermediatory and is called a direct exchange interaction. Besides this direct exchange, there are also some interactions that take place even when there is no direct overlap of the electronic wave functions on magnetic ions. In such cases, the interaction is mediated by a non magnetic ion in insulators or by conduction electrons in metals. These interactions are called indirect exchange interactions. The various indirect exchange interactions are superexchange interaction, Ruderman-Kittel-Kasuya-Yosida (RKKY) interaction, double exchange interaction and anisotropic exchange interaction [6]. The one that is particularly interesting here is the anisotropic exchange interaction called the Dzyaloshinskii-Moriya interaction and is discussed below.

### 1.2.2 Dzyaloshinskii-Moriya (DM) interaction

The Dzyaloshinskii-Moriya (DM) interaction is an anisotropic exchange interaction mediated through spin-orbit coupling [6]. The role of the spin-orbit interaction is to bring one of the magnetic ions into the excited state [7, 8]. Then the ion in the excited state couples to the ground state of the other ion. When acting between two spins $\boldsymbol{S}_1$ and $\boldsymbol{S}_2$ it leads to a term in the Hamiltonian given by:

$$H_{DM} = \mathbf{D} \cdot (\mathbf{S}_1 \times \mathbf{S}_2) \tag{1.2}$$

where $\boldsymbol{D}$ is a vector known as DM vector. $\boldsymbol{D}$ vanishes when the crystal has an inversion symmetry. In a noncentrosymmetric environment, it does not vanish and lies parallel or perpendicular to the line containing the two spins depending on the

symmetry. The form of the interaction is such that it prefers $\boldsymbol{S}_1$ and $\boldsymbol{S}_2$ to be at right angles in a plane perpendicular to the vector $\boldsymbol{D}$ in such an orientation as to ensure a negative energy.

It was Dzyaloshinskii who first realized the importance of broken inversion symmetry in the crystal lattice for magnetism [9]. Based on symmetry analysis he found that the DM term is allowed in the Ginzburg-Landau (GL) free energy functional if the crystal lattice lacks an inversion center, where it takes the form $\boldsymbol{M} \cdot (\nabla \times \boldsymbol{M})$. Later, Moriya extended Anderson's theory of superexchange and found that the microscopic mechanism of spin-orbit coupling is responsible for this interaction [8] and thus the interaction got its name.

## 1.3 Phase diagram of noncentrosymmetric magnets

In section 1.2.2 it was noted that the lack of an inversion center in the crystal lattice allows the DM term in the Hamiltonian. Thus the system involves at least three hierarchial energy scales – the exchange interaction, the DM interaction and the magnetocrystalline anisotropy. The exchange interaction favors the parallel alignment of spins while the DM interaction tends to align those spins perpendicular to each other. In the systems we are interested in, often the DM term having its origin to the spin-orbit coupling is the weaker term and hence the result of the competition is usually a long period helical ground state. The magnetocrystalline anisotropy dictates the direction of the resultant helix.

Modulated magnetic structures, like the helical structure, of one form or another as shown in Figure 1.2 are not particularly unusual. Over 100 different materials with different kinds of modulated structures are presented in Ref. 5. But there is a fundamental difference between the modulated structures formed in a crystal with and without the center of symmetry. The DM interaction is responsible for this

difference. Presence of the DM interaction puts an additional restriction that the spirals can have only one sense of rotation i.e. handedness and hence such spirals are chiral. However, no such restriction exists in the case of materials without DM interaction [10–13].

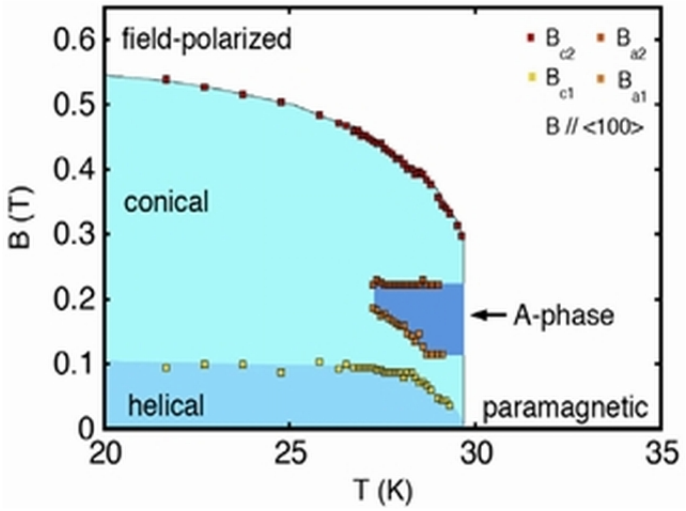


**Figure 1.3:** B-T phase diagram of MnSi, after Pfleiderer *et al.* [14].

Figure 1.3 shows the magnetic phase diagram of a well studied helimagnet, MnSi, that crystallizes in a chiral cubic space group $P2_13$. At ambient pressure MnSi undergoes a magnetic phase transition at about 29 K to a long period helimagnet, with a wavelength $\lambda_h \approx 180$ Å and a propagation axis that is weakly pinned to the cube diagonal <111>. Well below $T_C$ and for fields greater than 1 kOe (0.1 T), the applied field unpins the helical order and aligns its propagation vector parallel to the field. This portion of the phase diagram is known as the conical phase. At low temperatures and for fields greater than 6 kOe (0.6 T) the effect of the DM interaction is suppressed and there is a field polarized ferromagnetic state. Finally, for temperatures just below $T_C$ and for a magnetic field applied along <100> a phase known as the $A$ phase is stabilized [14–16]. Recently, this $A$ phase has been identified as a skyrmion lattice [14, 16]. A skyrmion is a complex spin structure that can

be visualized much like a stable whirl of a hurricane, where the spins are oriented in all directions, with the core and outer spins eventually becoming oriented in the downward (upward) and upward (downward) directions, respectively [Fig. 1.4]. It, in fact, is formed by the superposition of three helices with relative angles of 120° among them (see section 2.3). A similar phase diagram has been found in all the magnetically ordered materials so far studied in the space group $P2_13$, irrespective of the nature of underlying electrical conductivity. MnSi [17], FeGe [18] and $Fe_{0.5}Co_{0.5}Si$ [19] are metals and $Cu_2OSeO_3$ [20] is an insulator. The first three have ferromagnetic ordering and the latter one has ferrimagnetic ordering in a certain plane that modulates along a particular crystallographic direction to form a helical ground state.

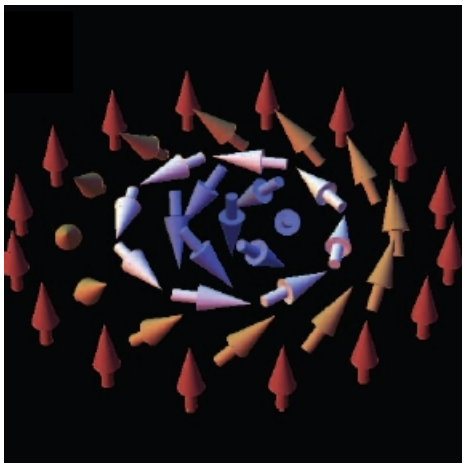

**Figure 1.4:** Schematic of a single magnetic skyrmion showing how the direction of the magnetic moment (arrows) varies in space, after Seki *et al.* [20].

The phase diagram (Fig. 1.3), however, is not universal for noncentrosymmetric magnets. In a system with stronger magnetocrystalline anisotropy, $Cr_{1/3}NbS_2$ (chiral space group $P6_322$) for instance [21], the external magnetic field cannot unpin the helix. Instead, the spins continuously orient in the direction of the applied field which, in turn, evolves another novel spin structure called the soliton. A magnetic soliton, in general, is a moving domain wall or a magnetic kink separating, usually, the regions

of parallel or antiparallel spins in a ferromagnet, or the two different (degenerate) ordered configurations in an antiferromagnet, the motion of which follows the sine-Gordon equation (see section 2.2 for details). The regular repetition of such solitons in a crystal forms a soliton lattice.

The chiral nature of the ground state helical ordering in noncentrosymmetric magnets makes these materials a possible ground for another exotic magnetic phase called the magnetic blue phase, a reminiscent of the blue phases observed in liquid crystals [22, 23] (see section 2.4 for detail). The initial study based on the Ginzburg-Landau (GL) theory ruled out the possibility of formation of the blue phases in the chiral magnets (ferromagnets) on the basis of the energy consideration [22]. However, recent studies have indicated that inclusion of higher terms in the GL energy functional can stabilize such phases [24, 25]. Indication of the blue phase has been realized in MnSi through the Monte Carlo calculations and neutron-scattering experiments in Ref. 26. The blue phase addressed some puzzling features of MnSi, such as partial magnetic ordering, a two-component heat capacity and thermal-expansion anomaly at the magnetic transition (see section 2.4).

## 1.4 Motivation

Interplay among more than two different competing interactions with different hierarchial energy scales makes noncentrosymmetric magnets an interesting class of materials. The theoretical and experimental indication of the possibility of manipulating skyrmions and solitons have pointed out that these structures have potential for technological application, especially in spintronics. Meanwhile, some of the properties like non-Fermi liquid behavior and partial magnetic ordering observed in MnSi, a model system for noncentrosymmetric magnets, are still not understood in the context of the existing theories. Even the origin of skyrmion lattice, observed so far in only one space group $P2_13$, is not well understood. The motivation of this dissertation is to find and study these structures/behaviors in new materials.

Finding an unresolved phenomena in a new family of materials helps provide new insight into the phenomena. Superconductivity is an example. The discovery of high temperature superconductors changed the paradigm of superconductivity based on the BCS theory. A brief account of the potentials of these structures and the existing problems in MnSi, and in general, this class of materials is presented below.

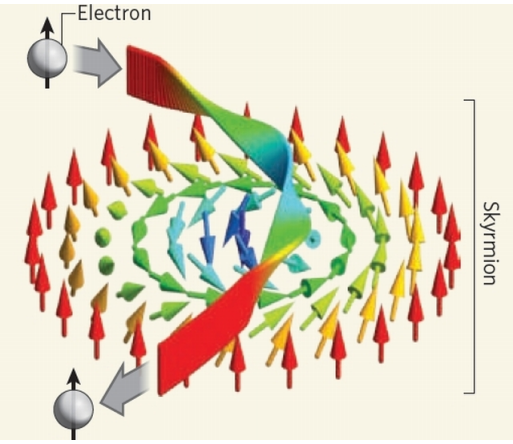


**Figure 1.5:** As an electron travels through a skyrmion, it acquires a topological force. It also exerts a force on the skyrmion, after Pfleiderer *et al.* [27].

A profound consequence of the skyrmion has been found for electronic transport, in particular, coupling between spin and charge. Figure 1.5 shows a schematic illustration of an electron traversing a skyrmion [27]. As the electron adjusts to the local spin structure, it acquires a Berry phase (a topological phase that arises when a quantum-mechanical system is transported on a closed adiabatic journey [28]) and experiences a force perpendicular to its motion similar to the Lorentz force. Such a force is expected to produce a topological Hall effect [a nonvanishing Hall effect in a ferromagnet having a topologically nontrivial (chiral) spin texture] [29] and this was indeed reported for MnSi [30]. Perhaps, even more significantly, however, is that an electronic current will exert a force on the skyrmion lattice and could perhaps change its lattice or domain structure. Indeed, these effects have been observed very recently using neutron scattering experiments. The magnetic diffraction pattern of a

sample of MnSi in the $A$ phase has been clearly observed to change when an electric current was passed through it. Most notably, the current density was over five orders of magnitude smaller than those applied in experimental studies on current driven magnetization dynamics in nano-structures [31]. Such effects are extremely relevant for spintronics applications.

A soliton is basically a moving domain wall, the motion of which is described by the sine-Gordon equation. Thus the spatial periodicity of the soliton lattice is tuneable by external parameters like temperature [32] and magnetic field [21, 33]. In a conducting system, the itinerant electrons can exert force on the soliton producing spin transfer torque that may result in the motion of the soliton. The consequence is that there is a possibility of observing behaviors like spin current induction [34], current-driven collective transport [35], and anomalous magnetoresistance [36] that are considered to be useful in spintronics technology.

Figure 1.6 shows the pressure-temperature phase diagram of MnSi, a material that can be taken as a model system for noncentrosymmetric magnets. The magnetic transition temperature ($T_C$) gets suppressed continuously up to about 12 kbar of pressure, above which the $T_C$ changes abruptly and vanishes at a critical pressure ($p_c$) of about 14.6 kbar. In the ordered state below $p_c$, the temperature dependence of electrical resistivity shows a normal $\rho \approx T^2$ Fermi liquid behavior. However, for $p > p_c$ an anomalous behavior of the resistivity $\rho \approx T^{\frac{3}{2}}$ is observed, suggesting a non-Fermi liquid (NFL) phase. The NFL region (below about 10 K and 14.6 kbar) persists over 3 orders of magnitude in temperature (down to mK range) and to about 30 kbar ($\approx$ twice $p_c$) [14]. The NFL behavior is postulated to exist in some metallic systems like heavy-fermion compounds [37, 38] and in some oxide materials [39–42]. But the NFL behavior observed in the normal state of an itinerant-electron ferromagnet is quite unusual. Neutron scattering experiments [43] have found that for pressures greater than a critical pressure $p_c$, long range magnetic order is lost and a peculiar partial helical order is revived on intermediate time and length scales. Although this partial magnetic ordering is thought to be responsible for the anomalous $\rho \approx T^{\frac{3}{2}}$

behavior, currently there is no generally accepted explanation for this non-Fermi liquid resistivity in MnSi. Also, in spite of some theoretical attempts [12, 25, 26, 44] the nature of the partially ordered state itself is not still well understood.

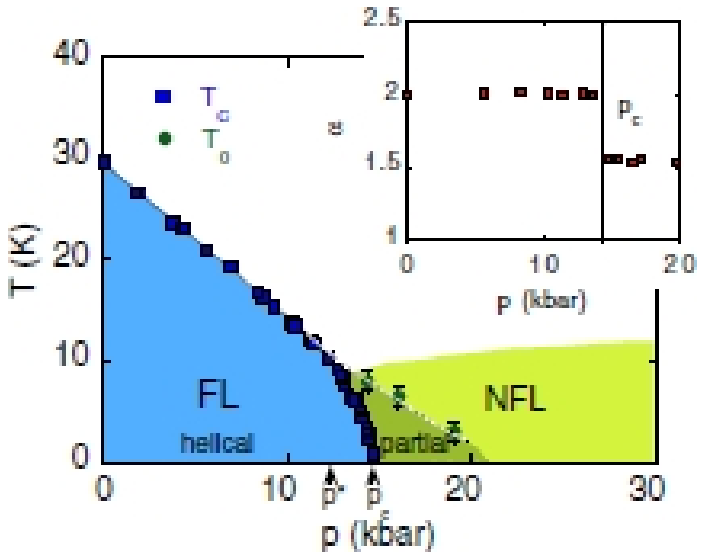


**Figure 1.6:** Pressure ($p$) vs temperature ($T$) phase diagram of MnSi. The transition temperature $T_C$ decreases continuously with increasing pressure and changes abruptly above about 12 kbar and vanishes at the critical pressure ($p_c$) of $\approx 14.6$ kbar. Below $p_c$ the ordered state shows a normal Fermi-liquid (FL) behavior. The non-Fermi liquid (NFL) state appears above $p_c$ and extends at least up to pressure of 30 kbar and down to temperature of 20 mK. The inset shows that in the partially ordered phase, the exponent describing the temperature dependence of the electrical resistivity, $\alpha$, changes abruptly from 2 to 1.5, after Pfleiderer *et al.* [45].

Yet another important aspect of the DM interaction is its role in multiferroic behavior [46–48]. The recent discovery of the multiferroic skyrmion in a noncentrosymmetric insulator $Cu_2OSeO_3$ [20] has provided strong support for the relation between the DM interaction and ferroelectric behavior without the necessity of an obvious structural distortion. $Cu_2OSeO_3$ crystallizes in the space group $P2_13$, same as that of MnSi and has a helimagnetic ground state below about 59 K. A magnetic field of about 1 kOe establishes the skyrmion lattice phase in the bulk sample in a small temperature and field range near the magnetic transition temperature. The field

polarized state is a collinear ferrimagnetic phase. No evidence of structural distortion has been observed down to 10 K. It is observed that this material shows ferroelectric polarization in all the three states – the helimagnetic state, skyrmion lattice phase and the ferrimagnetic state. A density functional theory (DFT) calculation [49] has shown that there is a strong DM interaction between different Cu ions and is responsible for the formation of the first two phases. However, for the ferroelectric polarization in the ferrimagnetic state an unusual mechanism of single-spin-site contribution due to spin-orbit coupling is found responsible. Since the DM interaction is allowed in all noncentrosymmetric magnets, this class of materials thus provides a platform to study the role of DM interactions in multiferroicity.

## 1.5 Outline of thesis

Chapter two presents a literature review of the existing theories related to the formation of a helical ground state, formation of complex magnetic structures – soliton and skyrmion and their experimental observation.

Chapter three deals with a brief description of the theory of elastic neutron scattering and the expected observation in case of a simple ferromagnetic and helical spin ordering.

Chapter four presents the results obtained in the study of a polycrystalline sample of $Cr_{11}Ge_{19}$ by means of DC magnetization, AC susceptibility, electrical resistivity, heat capacity, x-ray diffraction and resonant ultrasound spectroscopy measurements, and first principles calculations.

Chapter five is related to the study of $Cr_{1/3}NbS_2$ in a single crystal form by means of DC magnetization, resistivity, magnetoresistance, heat capacity and Seebeck coefficient measurements, and electronic structure calculations.

Chapter six presents results of single crystal neutron diffraction and small angle neutron scattering experiments conducted on the single crystals of $Cr_{1/3}NbS_2$ carried out to investigate formation of the soliton lattice.

Chapter seven presents the results of DC magnetization, AC susceptibility and heat capacity measurements on $K_2V_3O_8$.

Finally, in chapter eight concluding remarks are made on the basis of the results obtained in all three materials.

# Chapter 2

# Theoretical background and literature review

## 2.1 Ginzburg-Landau theory of chiral helix in noncentrosymmetric crystals

Ginzburg-Landau (GL) theory is a general phenomenological method for discussing the onset of various kinds of order in many-body systems. The theme is that there exists an order parameter which is non-zero in the ordered state, below a critical temperature ($T_C$), and vanishes above it. The order parameter is small in the vicinity of $T_C$ and hence an appropriate energy functional can be expanded as a power series in the order parameter. The expansion is carried out just far enough to ensure the thermodynamic stability. The equilibrium thermodynamics of the system is then obtained by minimizing the energy functional with respect to the order parameter.

In case of a smoothly varying magnetic texture, local magnetization ***M(r)*** is taken as the order parameter. For a simple ferromagnet, in absence of magnetic field, the minimal energy functional takes the form [50, 51]:

$$F(\boldsymbol{M}) = \int_V d\mathbf{r}\ \{\alpha(\boldsymbol{M})^2 + \beta(\nabla \boldsymbol{M})^2 + u(\boldsymbol{M})^4\}, \tag{2.1}$$

where $\int_V$ represents the real space integral over the system volume. $(\nabla \boldsymbol{M})^2$ stands for $\sum_{i,j=1}^{3} \partial_i M_j \partial_j M^j$, with $\partial_i \equiv \partial/\partial x_i$ the component of gradient operator $\nabla \equiv (\partial_x, \partial_y, \partial_z)$. $\alpha, \beta$, and $u$ are the phenomenological parameters that are determined by the microscopic theory of a particular system. The expansion 2.1 takes into account the fact that $F(\boldsymbol{M})$ has the same symmetry as the microscopic Hamiltonian. The last term in the expansion ensures the stability of the system for positive value of $u$. The second term represents the exchange interaction and thus $\beta$ is positive for a ferromagnet. The coefficient of the first term, $\alpha$, determines the phase of the system. For $\alpha < 0$ ($> 0$) the system is in the ordered (disordered) state.

Now, in case of noncentrosymmetric magnets DM term is allowed. In the GL free energy functional it takes the form [10, 52]:

$$F(\boldsymbol{M})_{DM} = \int_V d\mathbf{r}\ 2\ D\ \boldsymbol{M} \cdot (\nabla \times \boldsymbol{M}) \tag{2.2}$$

The minimal GL free energy functional for the noncentrosymmetric magnets thus becomes:

$$F(\boldsymbol{M}) = \int_V d\mathbf{r}\ \{\alpha(\boldsymbol{M})^2 + \beta(\nabla \boldsymbol{M})^2 + 2\ D\ \boldsymbol{M} \cdot (\nabla \times \boldsymbol{M}) + u(\boldsymbol{M})^4\}, \tag{2.3}$$

Here, it can be inferred that the functional 2.3 incorporates three different energy scales - exchange energy which favors a uniform spin polarization, the DM interaction that favors perpendicular orientation of spins and the crystal field interaction described by higher order spin orbit terms which are responsible for locking the magnetic structure to a certain crystallographic direction (not shown).

Minimization of equation 2.3 gives the magnetic ground state and is satisfied for the solution:

$$\boldsymbol{M}(\boldsymbol{r}) = \boldsymbol{M}_o(\hat{\boldsymbol{m}}_1 cos(\boldsymbol{q}_o \boldsymbol{r}) + \hat{\boldsymbol{m}}_2 sin(\boldsymbol{q}_o \boldsymbol{r})), \tag{2.4}$$

where $\boldsymbol{m}_1$, $\boldsymbol{m}_2$ and $\boldsymbol{q}_o$ are mutually perpendicular vectors. Equation 2.4 represents

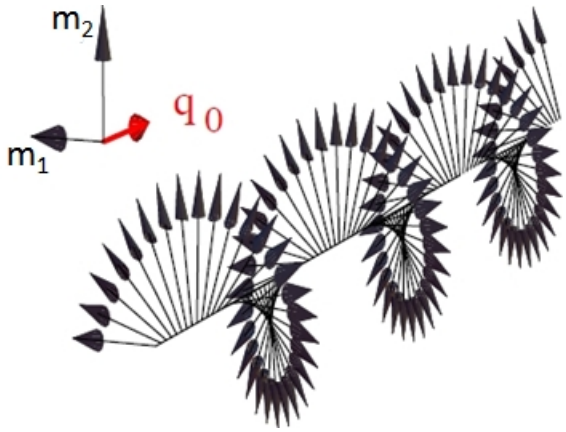


**Figure 2.1:** Helical modulation of the magnetization. The direction of the magnetization twists around $q_o$ - axis, planes of constant magnetization are perpendicular to $q_o$, after Fischer [24].

helical modulation of the magnetization. Thus, the consequence of introducing the DM interaction is that it leads to a helical ground state. The helical order breaks down for $\alpha > D^2/\beta$ and the direction of the helix depends on the sign of $D$ [10]. The spiral is right handed for $D < 0$ and left handed for $D > 0$. The equilibrium value of $M$ and $q_o$ obtained by inserting equation 2.4 in equation 2.3 are $q_o = D/\beta$ and $M_o^2 = -[\alpha/2 - D^2/(2\beta)]/(2u)$. As mentioned above, the pre-factor $D$ is small. Thus, pitch of the helix given by $2\pi/q_o$ is large in comparison to the lattice constants and, in general, incommensurate with the crystal lattice.

There may be some more terms in the GL free energy allowed by the symmetry of the particular crystal structure. For instance, in case of MnSi following terms are allowed by the symmetry of the space group $P2_13$ [10]:

$$\frac{1}{2}B_2[(\partial_x M_x)^2+(\partial_y M_y)^2+(\partial_z M_z)^2]+B_3[(\partial_x^2 M)^2+(\partial_y^2 M)^2+(\partial_z^2 M)^2]+C(M_x^4+M_y^4+M_z^4) \tag{2.5}$$

These terms are responsible for pinning of the helix to a certain crystallographic direction viz. <111> for $B_3 > 0$ and along <100> for $B_3 < 0$ in MnSi.

## 2.2 Soliton in noncentrosymmetric magnets

A soliton by definition is a localized solution of a nonlinear dispersive wave equation that remains invariant upon propagation [53]. It represents a self-localized or self-trapped wave packet and exhibits a particle-like nature [54]. The first observation of a soliton dates back to 1834 when a Scottish engineer John Scott Russell encountered a water wave which he called a "great wave of translation" [55, 56]. However, the first theoretical description was given by Zabusky and Kruskal [57] from where the name "soliton" was established. Since then solitons have obtained widespread attention and are now studied in diverse fields of science such as mathematics, biology, oceanography, meteorology, optics, elementary particle physics, solid state physics and more [58]. Solitons play an important role in the neutral and charge transport in polymers [59]. In biology, a discrete soliton model has been put forwarded to understand the energy transfer in $\alpha$-helices [60, 61]. Likewise, Frenkel-Kontorova models [62], Josephson junction arrays [63], localized modes in anharmonic crystals [64] are some other fields where solitons have been realized. Technological application of solitons has been realized in optical fiber communication [65]. In a review article about the solitons in condensed matter physics Bishop *et al.* [66] even has labeled condensed matter physics as a storehouse of the solitons.

An extensive study of solitons appears in the quasi-one dimensional magnetic chains that are formed in some ionic magnetic compounds. The archetypical materials are $CsNiF_3$ [67, 68] and $[(CD_3)_4N]MnCl_3$ (TMMC) [69, 70]. A magnetic soliton in these materials is basically a thermally excited domain wall or a "kink" separating spin-up and spin-down regimes of a ferromagnetic chain or the two degenerate configurations of an antiferromagnetic chain. The sketch of different solitons in ferromagnetic and antiferromagnetic chains are shown in Figure 2.2.

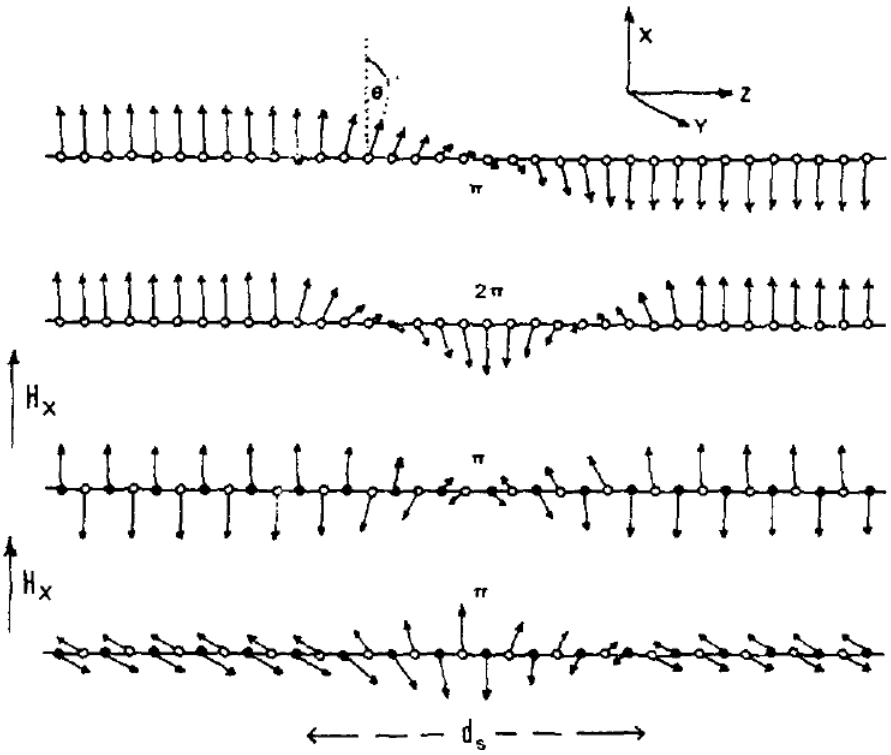


**Figure 2.2:** Schematic of solitons in magnetic chains. From top to bottom are shown: $\pi$- and $2\pi$- soliton in ferromagnetic chain and the antiferromagnetic $\pi$- soliton for H $<$ H$_{SF}$ and H $>$ H$_{SF}$, respectively (H$_{SF}$ is the spin flop field), after de Jongh *et al.* [71].

In fact, soliton is a nonlinear, large amplitude, localized solution $\phi(z,t)$ of the sine-Gordon equation 2.6 for which $\phi(z,t)$ changes by $2\pi$ over a finite width $d = 1/m$ [71]:

$$\frac{\partial^2\phi}{\partial^2 z} - \frac{1}{c}\frac{\partial^2\phi}{\partial^2 t} = m^2 sin\phi, \tag{2.6}$$

where $c$ is the characteristic velocity and $m$ plays the role of the mass. In 1978 Mikeska [67] realized that a one-dimensional ferromagnet with an easy plane anisotropy and a symmetry-breaking magnetic field in the easy plane could be represented by the SG equation 2.6. It represents a $2\pi$-soliton. Soon after, a $\pi$-soliton was realized in antiferromagnetic chains with weak anisotropy [69, 72]. Later, de Jongh [71], based on Enz's relation between a one-dimensional ferromagnetic domain wall and the SG equation [73], made an argument about the existence of $\pi$-solitons in ferromagnets.

Solitons in these systems have been experimentally observed in inelastic neutron experiments [68, 69].

Noncentrosymmetric magnets are another class of materials where formation of soliton is theoretically expected. It is a more elegant system because, unlike in one-dimensional magnetic chains, no thermal excitation is required for the formation of soliton and the soliton evolves directly out of the ordered state with the application of magnetic field or changing temperature. Formation of soliton in a magnetic system without center of symmetry between two magnetic ions was first treated by Dzyaloshinskii in the 1960s [74] and has been discussed by many authors over the course of time [5, 36, 75, 76]. However, experimental observation of soliton in this class of materials is limited only to three materials so far - $Ba_2CuGe_2O_7$ [33], $CuB_2O_4$ [32] and $Cr_{1/3}NbS_2$ [21]. A brief theoretical description of the formation of magnetic soliton lattice in noncentrosymmetric magnets is presented below.

The DM interaction of the form $\boldsymbol{M} \cdot (\nabla \times \boldsymbol{M})$ can be expressed in the form of invariants involving the first derivative of the magnetization known as Lifshitz invariants of the form:

$$M_i \frac{dM_j}{d\eta} - M_j \frac{dM_i}{d\eta}, \tag{2.7}$$

where $M_i$ and $M_j$ are the components of the magnetization vectors that arise in certain combinations in expression 2.7 depending on crystal symmetry.

Izyumov [75] has described the phase transition in the systems admitting these linear Lifshitz invariants basically following what was originally reported by Dzyaloshinskii [74], a brief account of which is presented below:

The assumption made is that the modulus of the order parameter (OP) is constant. So the OP is written as:

$$M_i = \rho e^{i\phi}; M_j = e^{-i\phi} \tag{2.8}$$

where, $\rho$ and $\phi$ are the modulus and the phase of the OP, respectively.

Now, the free energy functional in the case of noncentrosymmetric crystal lattice takes the form

$$\Phi = \frac{1}{V}\int dz[\beta\rho^2(\frac{d\phi}{dz})^2 + 2D\rho^2\frac{d\phi}{dz} + 2w\rho^n cos(n\phi)] \tag{2.9}$$

The first, second and third terms on the right hand side of equation 2.9 represent the exchange energy, Lifshitz invariants describing the anisotropic interactions and the crystallographic anisotropy, respectively. In absence of the crystallographic anisotropy, equation 2.9 simply describes a modulated structure along the $z$ axis as described in section 2.1 with a wavevector given by $q_o = D/\beta$.

In general, the spatial distribution of the phase of the OP satisfies the following equations:

$$\frac{d^2(n\phi)}{dz^2} + vsin(n\phi) = 0, \tag{2.10}$$

where,

$$v = \frac{n^2 w\rho^{n-2}}{\beta} \tag{2.11}$$

Solution of equation 2.10 is given by:

$$\phi = \frac{n}{2}am(qz, x), \tag{2.12}$$

where q = $\sqrt{v}/\chi$ with $\chi$ being the modulus of the elliptic function such that 0$\leq \chi \leq$1. This parameter $\chi$ corresponds to the constant of integration of equation 2.10 and is found by the energy minimization of the system.

The energy of the system can be expressed in terms of the complete elliptical integrals of the first and second kind represented by $K$ and $E$, respectively. Minimization of this energy with respect to $\chi$ yields:

$$\frac{E}{\chi} = \sqrt{\frac{v_c}{v}}, \tag{2.13}$$

where $v_c$=$n^2\pi^2D^2/16\beta^2$. With the help of equation 2.13 analysis of equation 2.12 suggests the following structure represented by the functional 2.9. A periodic structure with a period of $L = 4\chi K/\sqrt{v}$ is produced. This period changes with the change in parameter $v$. At small $v$, the phase of the magnetization $[\phi(z)]$ does not change much and hence corresponds to a helix. When $v$ increases, a section over the length $L$ appears where the phase is almost constant but the phase changes abruptly at the end of the period where change in phase by $2\pi$/n occurs. As $v$ approaches $v_c$, the relative fraction of the constant phase increases. At this time the system contains a nonlinear periodic structure consisting of domains of commensurate phase separated by a narrow region of domain walls. These narrow domain walls are actually the solitons and the periodic arrangement of these nonlinear periodic structures forms the magnetic soliton lattice. With a simple mathematical manipulation expanding $K$ and $E$ in the limiting cases $\chi \to 0$ and $\chi \to 1$, it can be seen that period of the soliton lattice shows logarithmical divergence as $v \to v_c$ and since the wavevector $q_o \propto 1/L$, $q_o \to 0$ as $v \to v_c$ thus marking the incommensurate-to-commensurate (IC) phase transition. The parameter $v$ can depend on external parameters such as temperature and external magnetic field.

In a specific case of a simple helix in an external magnetic field, the energy functional can be expressed as:

$$\Phi = \frac{1}{V}\int [dz\{\beta(\nabla M)^2 + \gamma M_z^2 + 2D(M_x\frac{dM_y}{dz} - M_y\frac{dM_x}{dz}) - MH\} \tag{2.14}$$

At positive and large anisotropy constant $\gamma$ the spins remain in ($x$, $y$) plane as long as $H$ is in the same plane. Now with $M_x = Mcos\phi$, $M_y = Msin\phi$ and $M_z = 0$; and n = 1, $v = h/2\beta$ with $h = H/M$, relation 2.13 in this case takes the form:

$$\frac{E}{\chi} = \sqrt{\frac{h_c}{h}}, \tag{2.15}$$

with $h_c = \pi^2 D^2/8\beta$ which suggests that there is a continuous nonuniform rotation of the spins along the $z$ axis with the increasing magnetic field forming the soliton lattice up to a critical field, above which there occurs an IC phase transition.

More recently, a similar result has been obtained by taking the Hamiltonian of the form [34, 36, 76]:

$$H = -J\sum_n S_n \cdot S_{n+1} + D \cdot \sum_n S_n \times S_{n+1} - 2\mu_B H \sum_n S_n^x, \tag{2.16}$$

where the first and the second term represent the ferromagnetic exchange interaction and the DM interaction between the nearest-neighbor spins. The third term represents the Zeeman term by the transverse magnetic field. The period of the soliton lattice as a function of the applied magnetic field *L(H)* is presented in a more convenient form solely in terms of the elliptic functions of the first and the second kind given by:

$$L(H) = \frac{8K(\chi)E(\chi)}{\pi q_o}, \tag{2.17}$$

with

$$\frac{E(\chi)}{\chi} = \sqrt{\frac{H_c}{H}}, \tag{2.18}$$

where $H_c$ is the critical field at which the IC transition occurs.

In absence of external magnetic field, the modulation is just a helix. So at $H$ =0, the period of the helix is $L(0) = 2\pi/q_o$. The fractional increase in the period during the evolution of the soliton lattice from the ground state helix is thus given by:

$$\frac{L(H)}{L(0)} = \frac{4K(\chi)E(\chi)}{\pi^2}, \tag{2.19}$$

Equations 2.18 and 2.19 give the relation between $L(H)/L(0)$ and $H/H_c$.

### 2.2.1 Experimental observation

Magnetic soliton lattice was observed in the easy axis antiferromagnet $Ba_2CuGe_2O_7$ [33] by means of magnetization measurements and a neutron scattering experiment. $Ba_2CuGe_2O_7$ is a weakly distorted antiferromagnet with all spins confined in the (1, -1, 0) plane. The staggered magnetization rotates upon translation along (1, 1, 0) direction forming a helical state with propagation vector along (1+$\xi$, $\xi$, 0) ($\xi = 0.027$). Zheludev *et al.* [33] found that when magnetic field is applied along the $c$ axis i.e. perpendicular to the helical axis, the propagation vector i.e. the period of the helix changes in accordance with the soliton model as shown in Fig. 2.3.

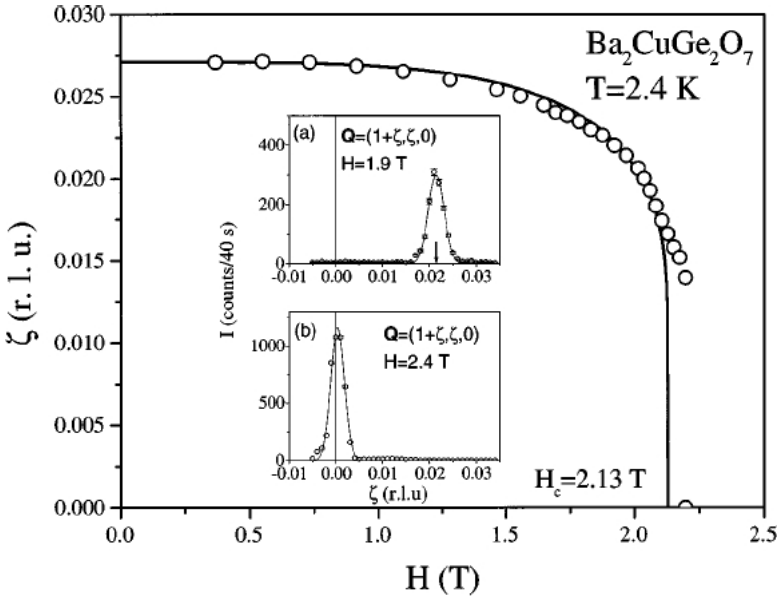


**Figure 2.3:** Magnetic field dependence of the magnetic propagation vector in $Ba_2CuGe_2O_7$ measured at T = 2.4 K. The solid line is a theoretical fit. Inset shows the elastic scan across the antiferromagnetic zone center for two different values of magnetic field applied along the (0, 0, 1) direction, after Zheludev *et al.* [33].

$CuB_2O_4$ is another material that shows the magnetic soliton lattice. This material has two magnetic phases in the ordered state. Between 10 and 20 K, it has a commensurate phase showing a weak ferromagnetic behavior. Below 10 K the

propagation vector changes with temperature according to the soliton model as shown in Fig. 2.4. Here, the soliton lattice is formed in the absence of external magnetic field.

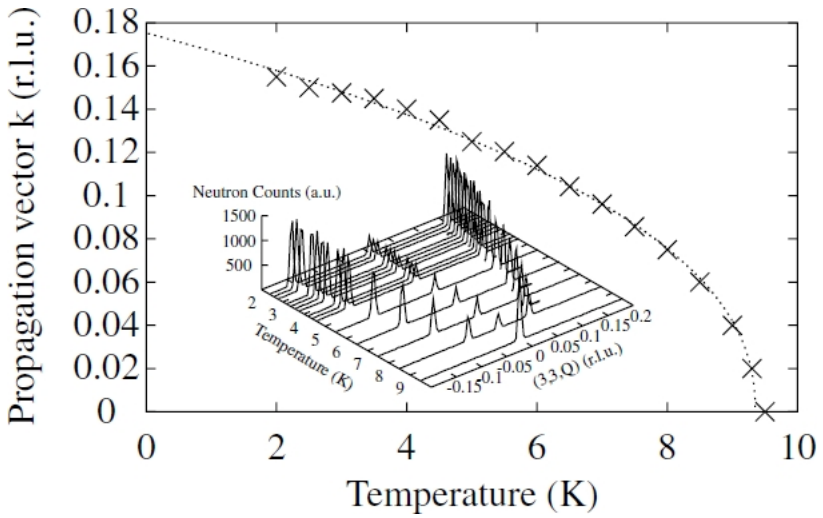


**Figure 2.4:** Temperature dependence of the magnetic propagation vector in $CuB_2O_4$. The line is a theoretical fit. Inset shows the elastic scan along (3, 3, Q) showing the evolution of the magnetic satellites in $CuB_2O_4$ for selected temperatures, after Roessli *et al.* [32].

$Cr_{1/3}NbS_2$ is another material know to have the soliton lattice. The ordered phase below about 127 K is a helimagnetic state with propagation vector along the $c$ axis. Recently, Togawa *et al.* observed the evolution of the soliton lattice with increasing magnetic field below 2.3 kOe by means of a Lorentz force transmission electron microscope (LFTEM) [21]. In absence of applied magnetic field, they observed a sinusoidally varying stripe patters in LFTEM indicating a helical state. With the application of the magnetic field they observed the distance between the patterns changed in accordance with the soliton model as shown in Fig. 2.5.

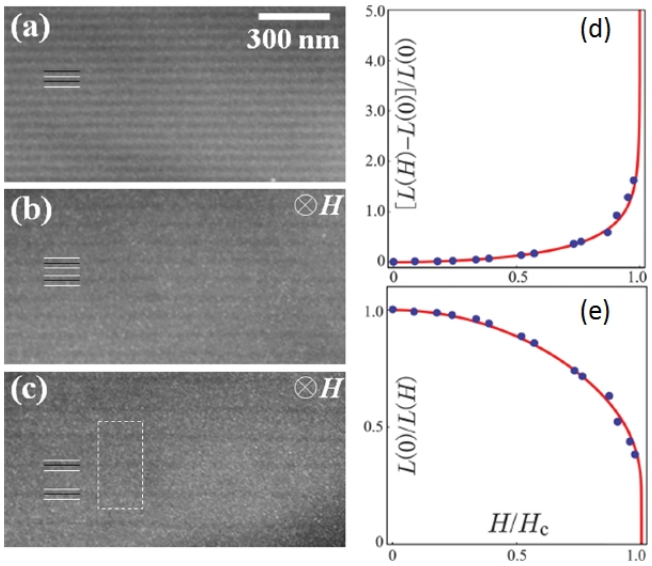


**Figure 2.5:** (a) Underfocused Lorentz micrographs at 110 K in zero applied magnetic field (b) in a perpendicular magnetic field of 2.08 kOe and (c) in a perpendicular field of 2.24 kOe. Sinusoidal line patterns can be seen in (a). In (b) the sinusoidal line patterns change to another periodic pattern. In (c) the separation between these periodic patterns can be seen significantly increased suggesting that the commensurate ferromagnetic phase (region between two white strips) has increased significantly. This pattern was found to disappear above 2.3 kOe. (d) Experimental plot of the relative increase in the period of the structure as compared to the period of helix in zero applied magnetic field as a function of $H/H_c$ with fitting curve, where $H_C$ is the critical field = 2.3 kOe. (e) Fractional change in the periodicity as compared to the period of the helix at zero applied magnetic field as a function of $H/H_c$ along with the theoretical fit, after Togawa *et al.* [21].

## 2.3 Skyrmion in noncentrosymmetric magnets

As stated in section 1.3, a skyrmion is a vortex-like stable spin structure in which the direction of the spins changes continuously from the outer layer to the inner core with an eventual antiparallel configuration between the outer and the core spins as depicted in Figure 1.4. It is named after an English particle physicist, Tony Skryme, who in the early 1960s developed a theory of such structures in the field of particle physics [77, 78]. Such a structure has also been marked in different systems in condensed matter physics, for instance, in quantum Hall liquids [79], superfluid helium 3 [80],

spinor or multi-component Bose-Einstein condensate [81, 82], Abrikosov vortex lattice in type-II superconductors [11], to mention a few.

Magnetic structures similar to the skyrmion namely, "magnetic vortices" have been observed in nanomagnetism, especially in ferromagnetic dots [83]. However, these "magnetic vortices" have different spin structure from that of the skyrmion. The vortex has a continuous variation of magnetization in the plane of the dot with the magnetization of the core being perpendicular to the plane. The origin of these vortices in the ferromagnetic dots lies in the fact that the magnetic objects lower their magnetostatic energy by forming domains and that the domain is not stable in the sub-micron region thus leading to the curling configuration [84]. But the skyrmions in the noncentrosymmetric magnets have a completely different microscopic mechanism that has the root origin in the DM interaction allowed in these crystal structures.

Skyrmions in a chiral magnet was first observed in the $A$ phase of MnSi in a neutron scattering experiment [16]. A six-fold pattern perpendicular to the applied magnetic field and independent of the direction of the applied magnetic field relative to the atomic lattice was observed in the $A$ phase region. However, a magnetic field parallel to the neutron beam was required to observe such a structure. This structure was described by a simple superposition of three helices with relative angles of 120° among them. Thus the $A$ phase or the skyrmion lattice is visualized as a spin crystal approximately characterized by the magnetization given by:

$$\boldsymbol{M}(\boldsymbol{r}) \simeq \boldsymbol{M}_f + \sum_{j=1}^{3} \boldsymbol{M}^h_{\boldsymbol{q}_j}(\boldsymbol{r} + \boldsymbol{\Delta r}_j), \tag{2.20}$$

where

$$\boldsymbol{M}^h_{\boldsymbol{q}_j}(\boldsymbol{r}) = B\{\hat{\boldsymbol{n}}^j_1 cos(\boldsymbol{q}_j \boldsymbol{r}) + \hat{\boldsymbol{n}}^j_2 sin(\boldsymbol{q}_j \boldsymbol{r})\} \tag{2.21}$$

is the magnetization of a single chiral helix with amplitude $B$. The wave vector $\boldsymbol{q}_j$ and the two unit vectors $\hat{\boldsymbol{n}}^j_1$ and $\hat{\boldsymbol{n}}^j_2$ are chosen such that the set $\{\boldsymbol{q}_j, \hat{\boldsymbol{n}}^j_1, \hat{\boldsymbol{n}}^j_2\}$ forms

an orthonormal basis. All three helices have the same chirality i.e $\boldsymbol{q}_j \cdot (\hat{\boldsymbol{n}}_1^j \times \hat{\boldsymbol{n}}_2^j)$ has the same sign. $\boldsymbol{\Delta r}_j$ is the relative shift in the helices.

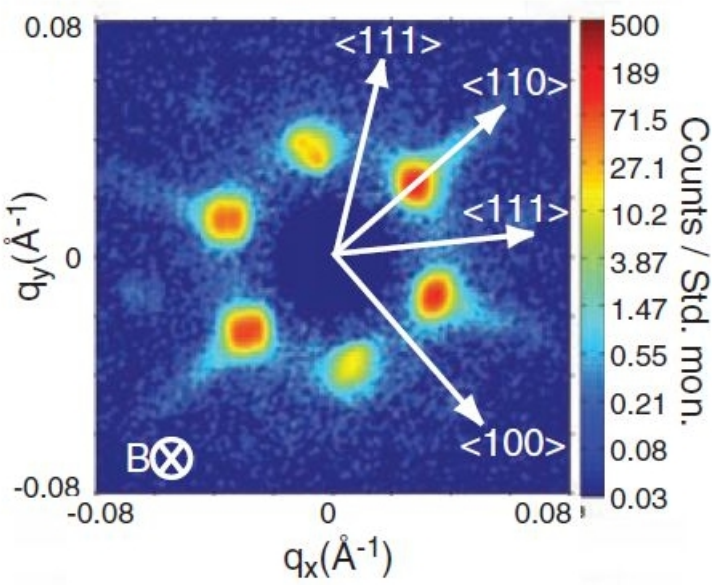


**Figure 2.6:** Sixfold intensity pattern in the $A$-phase of MnSi at T = 26.45 K, B = 1.54 kOe observed in the small angle neutron scattering experiment, after Mühlbauer *et al.* [16].

A similar six fold pattern appears in $Fe_{0.8}Co_{0.2}Si$ [85, 86] as shown in Fig. 2.7. Later skyrmion was observed in the real space using Lorentz TEM in the $A$ phase of $Fe_{0.5}Co_{0.5}Si$ [87] revealing the same hexagonal structure as shown in Fig. 2.8. The same structure has been observed in the $A$ phase of FeGe both in real space [88] and momentum space [89] and also in $Fe_xMn_{1-x}Si$ (x=0.02, 0.08) [90]. Remarkably, the skyrmion lattice has been observed recently in both real space [20] and momentum space [91] in a multiferroic material $Cu_2OSeO_3$. It is interesting that all these materials showing the skyrmion lattice belong to the same space group $P2_13$. All except $Cu_2OSeO_3$ have the B20 crystal structure.

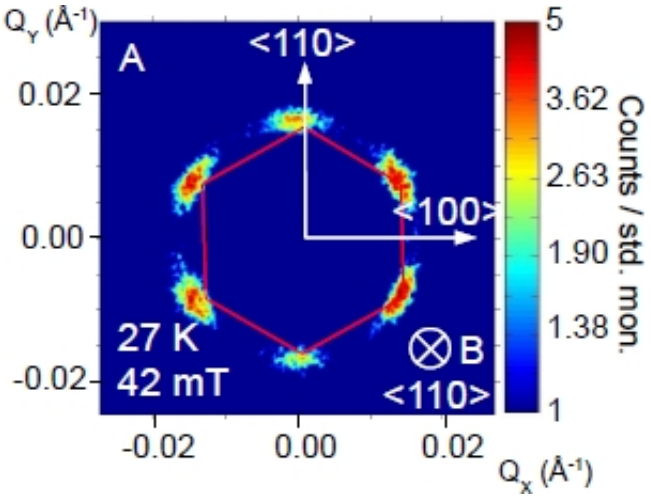


**Figure 2.7:** Typical small angle neutron scattering intensity in the *A*-phase of $Fe_{0.8}Co_{0.2}Si$ showing the clear sixfold diffraction pattern characteristic of the formation of a skyrmion lattice, after Adams *et al.* [85].

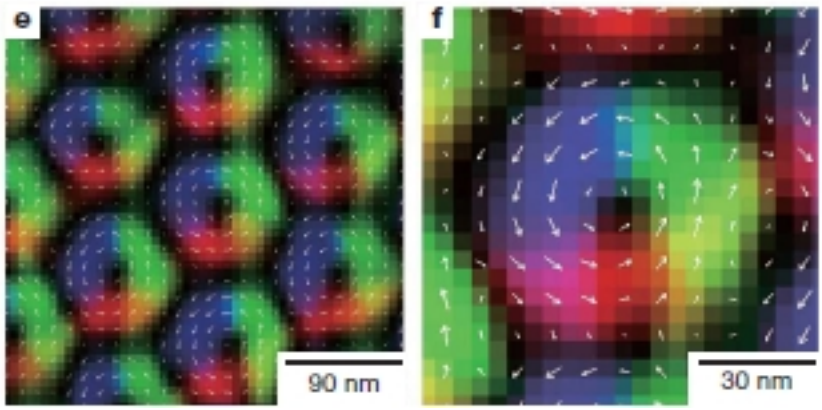


**Figure 2.8:** Experimentally observed real-space images of the skyrmion crystal structure of $Fe_{0.5}Co_{0.5}Si$ measured at a field of 0.5 kOe (left panel). Right panel is the magnified view of the figure in the left panel. The color map and white arrows represent the magnetization direction at each point, after Yu *et al.* [87].

It is worth notifying that two decades before the first experimental observation of a skyrmion lattice in MnSi [16], Bogdanov *et al.* [92–94], in 1989, theoretically predicted that a mixed state of magnets, namely magnetic vortices, a structure reminiscent of the Abrikosov vortices in type-II superconductors, should be stable in

some noncentrosymmetric easy axis ferromagnets and antiferromagnets, in a certain range of temperature and applied magnetic field. The name "skyrmion" was even used for the first time for such a magnetic vortex by the same group later in 2002 [11]. In 1994 the cubic helimagnets MnSi, FeGe, $Fe_xCo_{1-x}Si$ and $Co_xMn_{1-x}Si$ were predicted, again by Bogdanov and Hubert [95], to be promising materials for the search of such magnetic vortices. But it was mentioned that an additional uniaxial anisotropy has to be introduced either by growth conditions or external stress in order to stabilize the vortex states. Skyrmion has been observed in all these materials [16, 87, 88, 90], but without an obvious requirement of the additional uniaxial anisotropy. Till date, skyrmion has been observed in the helimagnets belonging to only one space group $P2_13$.

The idea of the magnetic vortex in noncentrosymmetric magnets originally stemmed from the vortices or the flux line lattices observed in type-II superconductors. The argument presented in the Refs. 92–94 is the following. One of the main differences between the type-I and type-II superconductors is their behavior in the external magnetic field. In the region of the field induced first order transition from superconducting state to the normal state, type-I superconductors show an intermediate state. But in case of type-II superconductors there appears a region of mixed state known as Abrikosov vortices. The surface energy of type-I superconductors increase with increase in the external magnetic field. But in case of type-II superconductors, the surface energy decreases after certain field. Abrikosov pointed out that this negative energy is responsible for the formation of the vortices or the flux line lattices in type-II superconductors.

The superconducting state is a pure diamagnetic state and the normal state is a paramagnetic state. Thus the field induced transition from the superconducting state to the normal state can be interpreted as transition between the two magnetic phases. It is argued that all these domain patterns in the superconductors and the magnets can be treated in the framework of a common theory. The formation of domain walls usually is associated with an additional positive energy. Thus a question was raised

whether there can be some magnetic states with negative domain wall energies as in the case of type-II superconductors. This question was addressed in Refs. 92–94 where it was found that such a state of magnet called the "magnetic vortex lattice", a distinct thermodynamical state is possible in magnetically ordered crystals belonging to the certain crystallographic classes - $C_n$, $D_n$, $C_{n\nu}$, $D_{2d}$ and $S_4$ (n = 3, 4, 6) in a certain range of magnetic field. A common thing among all the mentioned crystallographic classes is that they all are noncentrosymmetric and the key idea is the DM interaction. Such a magnetic vortex or "skyrmion" has not yet been experimentally realized in any of the easy axis ferromagnets and antiferromagnets belonging to the mentioned noncentrosymmetric point groups.

## 2.4 Blue phases in chiral ferromagnets

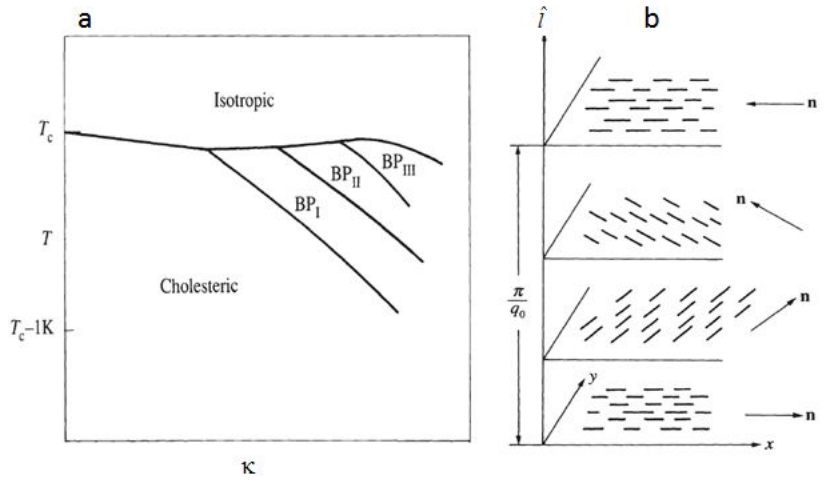


**Figure 2.9:** a) Typical phase diagram of liquid crystal involving an isotropic, a cholesteric and three blue phases in a temperature (T) chirality ($\kappa$) plane. b) The arrangement of molecules in the cholesteric mesophase. The successive planes are drawn for convenience, but do not have any specific physical meaning, after Gennes and Prost [23].

Blue phases are distinct thermodynamic phases that appear over a narrow temperature range ($\sim$ 1 degree) at the helical-isotropic boundary of highly chiral liquid crystals. There can be three blue phases: BPI, BPII and BPIII, the former two having cubic symmetry and the later one being amorphous. Figure 2.9(a) shows a sketch of phase diagram of chiral nematic liquid crystal.

The equilibrium structure of the helical phase is inhomogeneous and has locally uniaxial anisotropy (rod like cylindrical symmetry); characterized at each point by a single preferred axis called director $\boldsymbol{n}(\boldsymbol{r})$. Everywhere, $\boldsymbol{n}$ is perpendicular to a fixed direction, the pitch axis $\boldsymbol{l}$, and is uniform in planes perpendicular to $\boldsymbol{l}$ as shown in Fig. 2.9(b). Moving along $\boldsymbol{l}$, the direction of $\boldsymbol{n}$ twists uniformly about $\boldsymbol{l}$ with respect to distance $p_o = \pi/q_0$ called pitch of the helical phase.

Interestingly, the GL theory for the director of a chiral nematic is similar to that of the vector order parameter of a chiral magnet. Therefor, it has raised question whether there exists similar phases in magnetic systems.

Initial studies on the possibility of the existence of the blue phases in chiral magnets was conducted by Wright and Mermin [22] where they analytically showed that energy cost associated with the absence of stable line defects in chiral magnets does not allow the stability of the blue phases within the Ginzburg-Landau theory. However, recent theoretical calculations have indicated the possibility of blue phases in chiral ferromagnets [24, 26].

Within GL theory, the gradient free energy for the chiral nematics takes the form:

$$\varphi_{grad}^{nm} = 3\kappa^2[\lambda^2(\nabla_i n_j + \frac{1}{2}\epsilon_{ijk}n_k)^2 + \frac{1}{3}(\nabla\lambda)^2] \tag{2.22}$$

And that for the chiral ferromagnet is:

$$\varphi_{grad}^{fm} = \kappa^2[\lambda^2(\nabla_i n_j + \frac{1}{2}\epsilon_{ijk}n_k)^2 + (\nabla\lambda)^2] \tag{2.23}$$

The first term in equations 2.22 and 2.23 form double twist and the second term penalize the amplitude variation. It can be seen that amplitude variation costs three times more in chiral ferromagnets than in case of chiral nematics thus eliminating the possibility of formation of the blue phases in the chiral ferromagnets.

Fischer *et al.* [24] found that retaining higher order terms in spin orbit coupling expansion in the GL theory allowed the destabilization of the helical phase in favor of the crystalline phases that are periodic arrangement of double twist cylinders, analogous to the blue phases in liquid crystals.

GL free energy for chiral ferromagnets up to second order in chiral ferromagnets is given in equation 2.3. With order parameter $\boldsymbol{M} = \lambda \boldsymbol{n}$ it can be expressed as:

$$f(\boldsymbol{r}) = \frac{\beta}{2}\lambda^2(\nabla_i \mathbf{n}_j + \frac{D}{\beta}\epsilon_{ijk}\boldsymbol{n}_k)^2 + \frac{\beta}{2}(\nabla\lambda)^2 - \frac{D^2}{\beta}\lambda^2 + \frac{\alpha}{2}\lambda^2 + \mu\lambda^4 \tag{2.24}$$

Helical state is the lowest energy state for equation 2.24 for constant $\lambda$. In equation 2.24, the term $(\nabla\lambda)^2$ costs energy for the double twist cylinders. However, expanding the GL free energy to higher orders i.e. to the lowest order in spin orbit coupling allows a term of the form $(\sum \boldsymbol{M}_i \nabla \boldsymbol{M}_i)^2 = \frac{1}{4}(\nabla \boldsymbol{M}^2)^2$ to enter the GL free energy. This term acts on the amplitude of the magnetization and thus if the pre-factor of this term is allowed to be negative, it lowers the energy cost for the amplitude fluctuation thus allowing appearance of the blue phases in the chiral ferromagnets.

This attempt was done in an effort to explain the partial magnetic ordering in the NFL state of MnSi. A more recent calculations by Hamann *et al.* [26] showed that simplest DM nearest neighbor interactions are sufficient to induce the magnetic blue phases in the chiral ferromagnets. Their hamiltonian with nearest neighbor spin interaction is:

$$H = -\frac{1}{2N}\sum_{i=1}^{N}[\sum_{ij} J\boldsymbol{S}_i \cdot \boldsymbol{S}_j + \boldsymbol{D}_{ij} \cdot (\boldsymbol{S}_i \times \boldsymbol{S}_j)] \tag{2.25}$$

with $|\boldsymbol{D}_{ij}| = D$ and $\boldsymbol{D}_{ij} = \text{-}\boldsymbol{D}_{ji}$.

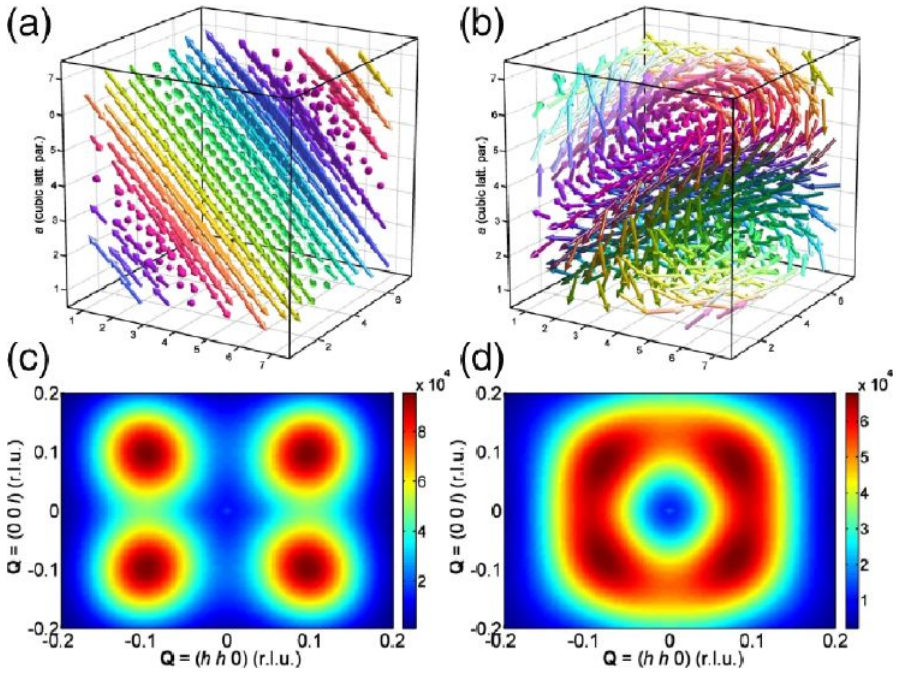


**Figure 2.10:** Calculations for clusters of spins interacting via equation 2.25. a) Helix locked in the cube 111 direction. b) Optimized structure with parallel spins having the same color. c), d) Calculated magnetic SANS intensity of a) and b) respectively, after Hamann *et al.* [26].

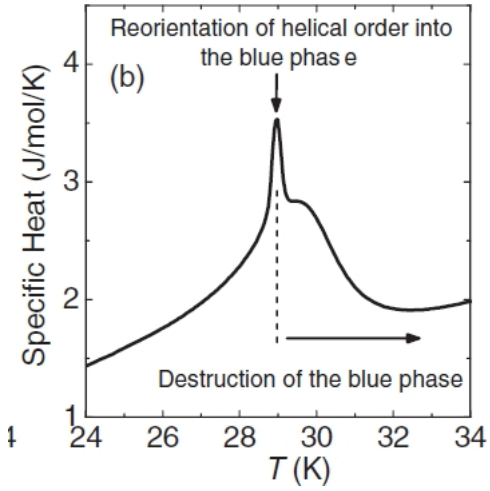


**Figure 2.11:** Temperature dependence of specific-heat of MnSi, after Hamann *et al.* [26].

The firs term represents the ferromagnetic exchange interaction and the second term represents the DM interaction. The results obtained from these calculations were found compatible with the experimental results. In calculated SANS intensity, helical order along <111> gave four diffraction spots whereas blue phase gave the ring as shown in Fig. 2.10. The anomaly observed in the heat capacity as shown in Fig. 2.11 has been understood as the existence of the blue phase. The broad second order tail adjacent to the sharp first order transition has been explained due to the gradual melting of the triple twist clusters.

# Chapter 3

# Principles of Neutron Scattering

Neutrons have zero charge, mass of 1.0087 atomic mass unit (amu), $\frac{1}{2}$ spin and magnetic moment of -1.9132 $\mu_N$ (nuclear magneton). These four properties make neutrons effective probe for condensed matter. Thermal and cold neutrons have total energy of about 25 meV (5 - 100 meV) and 1 meV (0.1 - 10 meV) respectively which correspond to the wavelength of about 1.8 Å and 9.0 Å respectively thus providing ideal probe for the study of structures of microscopic and mesoscopic length scales.

A typical neutron scattering experiment measures the probability that a neutron which is incident on a sample with wave vector $\boldsymbol{k}_0$ is scattered into the state with wave vector $\boldsymbol{k}_1$. The scattering process is governed by the laws of momentum and energy conservations:

$$\boldsymbol{Q} = \boldsymbol{k}_0 - \boldsymbol{k}_1 \tag{3.1}$$

$$E = E_0 - E_1 = \frac{\hbar^2}{2m_N}(k_0^2 - k_1^2) \tag{3.2}$$

where, $k = 2\pi/\lambda$ with $\lambda$ being the wavelength of the neutron beam. $m_N$ = mass of neutron. Momentum transfer is given by $\hbar\boldsymbol{Q}$.

Figure 3.1 shows the geometry of the scattering experiment. The effective scattering of each atom to an incident neutron can be expressed as cross-section. The neutron scattering cross-section corresponds to the number of neutrons scattered

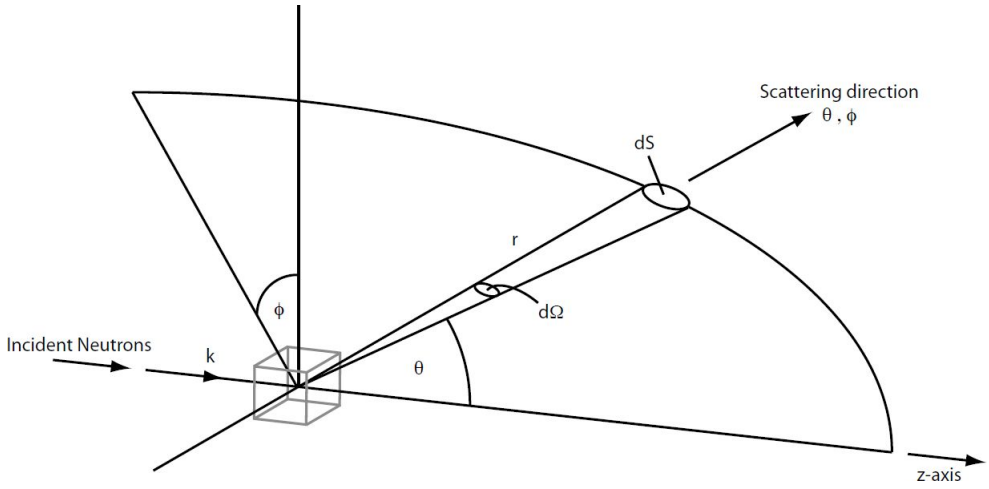


**Figure 3.1:** Geometry of a neutron scattering experiment, after Squires [96].

per second into a small solid angle $d\Omega$ with energy transfer between $\hbar\omega$ and $\hbar(\omega+d\omega)$ divided by the flux of the incident neutrons.

The master formula that lays out the basic principle of the neutron scattering experiments is obtained by using Fermi's Golden rule [97]:

$$\frac{d^2\sigma}{d\Omega dE}|_{\mathbf{k}_0\to\mathbf{k}_1} = \frac{1}{N}(\frac{m_N}{2\pi\hbar^2})^2(\frac{k_1}{k_0})\sum_{\lambda_0\sigma_0} p_{\sigma_0}p_{\lambda_0}\sum_{\lambda_1\sigma_1}|<k_1\lambda 1\sigma_1|\hat{V}|k_0\lambda_0\sigma_0>|^2\delta(E+E_{\lambda_0}-E_{\lambda_1}) \tag{3.3}$$

where, $|\lambda_0>$ denotes the initial state of scattering with energy $E_0$ and the population factor $p_{\lambda_0}$ and its final state is $|\lambda_1>$. $\sigma_0$ and $\sigma_1$ are the spin states of the incoming and the scattered neutrons respectively and $p_\sigma$ is the polarization probability. The $\delta$-function describes the law of energy conservation. $\hat{V}$ is the interaction operator of neutron with the sample which depends on the specific scattering process. In Born approximation, neutrons can be considered as plane waves:

$$|\boldsymbol{k}_0>=e^{i\boldsymbol{k}_0\cdot\boldsymbol{r}};|\boldsymbol{k}_1>=e^{i\boldsymbol{k}_1\cdot\boldsymbol{r}} \tag{3.4}$$

## 3.1 Nuclear Structure

The interaction between a neutron and a nucleus can be approximated by the Fermi pseudopotential [97]:

$$V(\boldsymbol{r}) = \frac{2\pi\hbar^2}{m_N} b_{\sigma\lambda}\delta(\boldsymbol{r} - \boldsymbol{R}), \tag{3.5}$$

where $b$ is the scattering length which, in general, depends on the spin state of neutron-nucleus system and $\boldsymbol{r}$ and $\boldsymbol{R}$ represent the instantaneous positions of neutron and nucleus, respectively. With this definition of the interaction potential, the master formula for unpolarized neutrons (for which case $\sigma_0$ and $\sigma_1$ disappear) becomes:

$$\frac{d^2\sigma}{d\Omega dE} = \frac{1}{N}\frac{k_1}{k_0}\sum_{\lambda_0} p_{\lambda_0} \sum_{\lambda_j} \mid \sum_j b_j < \lambda_1 | e^{i\boldsymbol{Q}\cdot\boldsymbol{R}_j} \mid \lambda_0 >|^2 \, \delta(E + E_{\lambda_0} - E_{\lambda_1}), \tag{3.6}$$

where $\boldsymbol{Q}$ = $\boldsymbol{k}_0$ - $\boldsymbol{k}_1$. With

$$\delta(E + E_{\lambda_0} - E_{\lambda_1}) = \frac{1}{2\pi\hbar}\int_{-\infty}^{\infty} e^{-i(E+E_{\lambda_0}-E_{\lambda_1})t/\hbar} dt \tag{3.7}$$

and decoupling the nuclear states and representing the scattering in terms of only the atomic coordinates appearing in equation 3.6, it can be expressed as:

$$\frac{d^2\sigma}{d\Omega dE} = \frac{1}{N}\frac{k_1}{k_0}\sum_{dd'}\sum_{j\in d, j'\in d'} < b_j^* b_j > S_{jj'}(\boldsymbol{Q}, E), \tag{3.8}$$

where $d$ and $d'$ refer to different elements, <> represents an average over spin and isotope distribution for the corresponding pair of elements and

$$S_{jj'}(\boldsymbol{Q}, E) = \frac{1}{2\pi\hbar}\int_{-\infty}^{\infty} < e^{-i\boldsymbol{Q}\cdot\boldsymbol{R}_j(0)} e^{i\boldsymbol{Q}\cdot\boldsymbol{R}_j(t)} > e^{\frac{-iEt}{\hbar}} dt \tag{3.9}$$

is the scattering function. Neutron scattering experiments essentially measure S($\boldsymbol{Q}$,E).

If the nuclear spins and isotopes are uncorrelated then

$$< b_j^* b_j >=< b_d^* >< b_d > + < b_d^2 > - < b_d >^2 \delta_{jj'}\delta_{dd'} \tag{3.10}$$

which when inserted in equation 3.8 gives two terms - one that gives the sum over all possible pair of atoms each term representing a correlation between the position of atom $j$ at time 0 and that of atom $j'$ at time $t$. This gives the coherent scattering. The other term represents a correlation between the position of $j$ at time 0 and that of same atom at time $t$. It gives the incoherent scattering. The incoherent scattering is isotropic and yields a constant background. On the other hand, coherent scattering provides the information about mutual arrangement of the atoms to the phase factor. In elastic scattering, the coherent scattering cross section is obtained by integrating the coherent scattering part of the double scattering cross-section, obtained form equations 3.8 and 3.10, with respect to $E$ and takes the form:

$$\frac{d\sigma}{d\Omega} = N_0 \frac{(2\pi)^3}{v_0} e^{-2W(\boldsymbol{Q})} \sum_{\boldsymbol{\tau}} \mid F_{\boldsymbol{\tau}} \mid^2 \delta(\boldsymbol{Q} - \boldsymbol{\tau}), \tag{3.11}$$

where $N_0$ is the number of unit cells, $v_0$ is the volume of the unit cell and

$$F_{\boldsymbol{\tau}} = \sum_j b_j e^{i\boldsymbol{\tau}\cdot\boldsymbol{r}_j} \tag{3.12}$$

is called the structure factor, and $\mathrm{e}^{-2W(\boldsymbol{Q})}$ is the Debye-Waller factor that describes the mean squared displacement of the atoms from their equilibrium position. $\boldsymbol{\tau}$ is the reciprocal lattice vector.

The structural information that can be obtained form the neutron diffraction experiment are - a) size and the form of the unit examining the scattering angle $2\theta$ at which Bragg reflection occurs, b) location of atoms within the unit cell from the analysis of the intensity of the Bragg reflections through the structure factor and

c) atomic displacement from the study of the ($\boldsymbol{Q}$) dependence of the Debye-Waller factor.

## 3.2 Magnetic Structure

The interaction potential between neutron with magnetic moment $\mu_N$ and magnetic field due to unpaired electron is given by:

$$V_M(\mathbf{r}) = -\boldsymbol{\mu}_n \cdot \boldsymbol{H} = -\boldsymbol{\mu}_n \cdot (\nabla \times \frac{\boldsymbol{\mu}_j \times \hat{r}}{r^2} - \frac{2\mu_B \boldsymbol{p}_j \times \hat{r}}{\hbar r^2}) \tag{3.13}$$

with $\boldsymbol{\mu}_n$ = -$\gamma\boldsymbol{\mu}_N\boldsymbol{\sigma}$ ($\gamma$ = 1.9132) and $\boldsymbol{\mu}_j$ = -2$\mu_B\boldsymbol{S}_j$, $\boldsymbol{S}_j$ and $\boldsymbol{p}_j$ are spin and moment of the electron. $\boldsymbol{\sigma}$ = pauli spin operator.

Considering only magnetic interaction between the unpolarized neutrons and the identical magnetic ions with localized electrons, and for spin only scattering, substitution of equation 3.13 into equation 3.3 gives:

$$\frac{d^2\sigma}{d\Omega d\omega} = (\gamma r_0)^2 \frac{k_1}{k_0} F_M^2(\boldsymbol{Q}) e^{-2W(\boldsymbol{Q})} \sum_{\alpha,\beta} (\delta_{\alpha\beta} - \frac{\boldsymbol{Q}_\alpha \boldsymbol{Q}_\beta}{Q^2}) S^{\alpha\beta}(\boldsymbol{Q},\omega) \tag{3.14}$$

with

$$\begin{aligned} S^{\alpha\beta}(\boldsymbol{Q},\omega) &= \sum_{j,j'} e^{i\boldsymbol{Q}\cdot(\boldsymbol{R}_j - \boldsymbol{R}_{j'})} \sum_{\lambda_0,\lambda_1} p_{\lambda_0} < \lambda_0 \mid \hat{S}^\alpha_{j'} \mid \lambda_1 >< \lambda_1 \mid \hat{S}^\beta_j \mid \lambda_0 > \\ &\times \delta(\hbar\omega + E_{\lambda_0} - E_{\lambda_1}) \end{aligned} \tag{3.15}$$

the so called magnetic scattering factor. $F_M(\boldsymbol{Q})$ is dimensionless magnetic form factor, $e^{-2W(\boldsymbol{Q})}$ is the Debye-Waller factor and $\hat{S}^\alpha_j(\alpha = x,\ y,\ z)$ is the spin operator of $j^{th}$ ion at site $R_j$. The magnetic form factor falls off with the increasing modulus of the scattering vector $\boldsymbol{Q}$. The polarization factor ($\delta_{\alpha\beta}$ -$\frac{\boldsymbol{Q}_\alpha \boldsymbol{Q}_\beta}{Q^2}$) tells that neutrons can only couple to magnetic moment or spin fluctuations perpendicular to $\boldsymbol{Q}$ which

allows to determine moment directions or to distinguish between different polarization of spin fluctuations.

For elastic scattering ($\lambda_0 = \lambda_1$) the scattering cross-section is obtained by integrating equation 3.14 w.r.t. $\omega$ which takes the form:

$$\frac{d\sigma}{d\omega} = (\gamma r_0)^2 e^{-2W(\boldsymbol{Q})} F_M^2(\boldsymbol{Q}) \sum_{\alpha,\beta} (\delta_{\alpha\beta} - \frac{\boldsymbol{Q}_\alpha \boldsymbol{Q}_\beta}{Q^2}) \sum_{\boldsymbol{l}} e^{i\boldsymbol{Q}\cdot\boldsymbol{l}} < \hat{S}_0^\alpha \hat{S}_l^\beta >, \tag{3.16}$$

where $\boldsymbol{l} = \boldsymbol{R}_j$ - $\boldsymbol{R}_{j'}$

## 3.3 Ferromagnet

Ferromagnet consists of domains with uniform arrangement of spin. However, spins in each domain have different orientations. Considering a single domain with spins oriented in z-direction, we have:

$$< \hat{S}_l^x > = < \hat{S}_l^y > = 0; < \hat{S}_l^z > \neq 0 \tag{3.17}$$

Then equation 3.16 for a Bravis ferromagnet takes the form:

$$\frac{d\sigma}{d\Omega} = N \frac{(2\pi)^3}{v_0} (\gamma r_0)^2 e^{-2W(\boldsymbol{Q})} F_M^2(\boldsymbol{Q}) < \hat{S}^z >^2 \sum_{\boldsymbol{\tau}} < 1 - (\frac{\boldsymbol{\tau}\cdot\boldsymbol{e}}{\tau})^2 > \delta(\boldsymbol{Q} - \boldsymbol{\tau}), \tag{3.18}$$

where $(\delta_{\alpha\beta} - \frac{\boldsymbol{Q}_\alpha \boldsymbol{Q}_\beta}{Q^2}) = 1 - (\frac{Q_z}{Q})^2 = 1 - \frac{\boldsymbol{Q}\cdot\boldsymbol{e}}{Q} = 1 - \frac{\boldsymbol{\tau}\cdot\boldsymbol{e}}{\tau}$, $\boldsymbol{e}$ is the unit vector along the magnetization direction $z$ and $\boldsymbol{\tau}$ is the reciprocal lattice vector. For an arbitrary distribution of domain orientations $< 1 - (\frac{\boldsymbol{\tau}\cdot\boldsymbol{e}}{\tau})^2 > = \frac{2}{3}$.

Equation 3.18 shows that ferromagnetic Bragg scattering occurs at all the reciprocal lattice vectors $\boldsymbol{\tau}$.

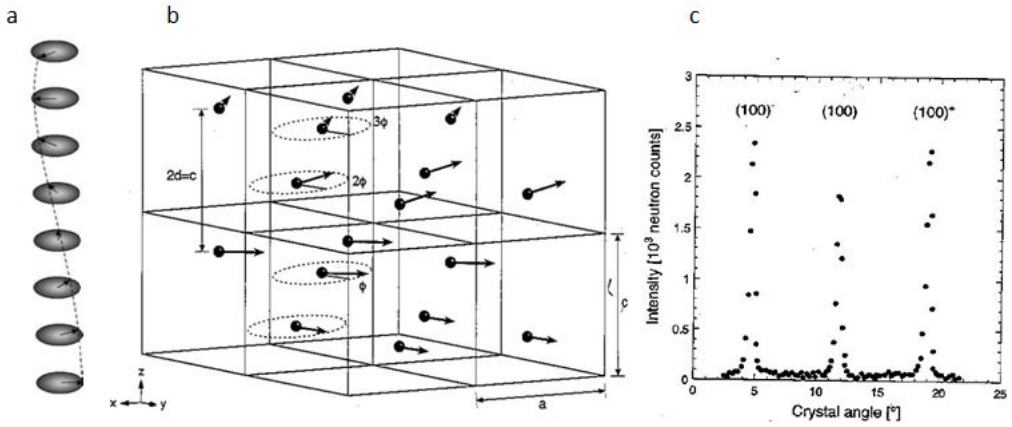


**Figure 3.2:** a) A typical helimagnetic spin structure after Chatterji [98]. b) Helical arrangement of the magnetic moment in Ho below 133 K and c) Rocking curve about the nuclear Bragg reflection (100) in Ho in the helimagnetic state (77K). The magnetic satellites are indexed by $(100)^-$ and $(100)^+$, after Furrer *et al.* [99].

## 3.4 Helical spin structure

Figures 3.2(a) and 3.2(b) show a typical helical spin structure where, within a plane perpendicular to the $c$ axis all the moments are ferromagnetically aligned, but the moment turns direction by an angle $\phi$ between adjacent planes. Let us define spiral vector $\boldsymbol{P}$ as: $\boldsymbol{P}$ is a vector along $z$ direction with length $=\frac{2\pi}{\phi}d$, where $d$ is the distance between adjacent planes. Now, the expectation values of the spin operators are given by:

$$< \hat{S}_l^x > \;=\; < \hat{S} > cos(\boldsymbol{P}^* \cdot \boldsymbol{l}) \tag{3.19}$$

$$< \hat{S}_l^y > \;=\; < \hat{S} > sin(\boldsymbol{P}^* \cdot \boldsymbol{l}) \tag{3.20}$$

$$< \hat{S}_l^z > \;=\; 0 \tag{3.21}$$

with $\boldsymbol{P}^* = 2\pi/\boldsymbol{P}$.

Inserting equations 3.19, 3.20 and 3.21 in equation 3.16 and taking average of the polarization along x and y direction yields:

$$\frac{d\sigma}{d\Omega} = \frac{N}{4}\frac{(2\pi)^3}{v_0}(\gamma r_0)^2 e^{-2W(\boldsymbol{Q})} F_M^2((Q)) < \hat{S} >^2 (1+(\frac{Q_z}{Q})^2) \sum_{\boldsymbol{\tau}} \{\delta(\boldsymbol{Q}+\boldsymbol{P}^*-\boldsymbol{\tau})+\delta(\boldsymbol{Q}-\boldsymbol{P}^*-\boldsymbol{\tau})\} \tag{3.22}$$

Thus, the magnetic Bragg scattering occurs for $\boldsymbol{Q} = \boldsymbol{\tau} \pm \boldsymbol{P}^*$ i.e. each nuclear Bragg peak is flanked by a pair of magnetic satellites as shown in Fig. 3.2(c).

## 3.5 Small angle neutron scattering

The small angle neutron scattering (SANS) is a technique used to study structural properties of materials on the so-called mesoscopic scale covering the length scale of 10 to 1000 $\mathring{A}$. As in any scattering experiment, the measured quantity is the intensity of the scattered monochromatic neutrons as a function of scattering angle by a sample under study, with the aim of determining the scattering cross-section as a function of wave-vector transfer given by:

$$\boldsymbol{Q} = \frac{4\pi sin(\theta)}{\lambda} \tag{3.23}$$

with $2\theta$ being the scattering angle and $\lambda$ the neutron wavelength. The scattered intensity distribution with a width $\simeq 2\pi/R_0$ centered around $Q_0 = 2\pi/R_0$ reflects the presence of the structure of radius $R_0$.

# Chapter 4

# Complex itinerant ferromagnetism in noncentrosymmetric $Cr_{11}Ge_{19}$

A similar version of this chapter appeared as "Complex itinerant ferromagnetism in noncentrosymmetric $Cr_{11}Ge_{19}$", N. J. Ghimire, M. A. McGuire, D. S. Parker, B. C. Sales, J.-Q. Yan, V. Keppens, M. Koehler, R. M. Latture, and D. Mandrus, Phys. Rev. B **85**, 224405 (2012).

## 4.1 Introduction

$Cr_{11}Ge_{19}$ crystallizes in the noncentrosymmetric space group $P\bar{4}n2$ belonging to the point group $D_{2d}^{8}$ and orders ferromagnetically below about 90 K [100–102]. Interestingly, $D_{2d}$ is one of the crystallographic classes in which a ferromagnet is expected to have a thermodynamically stable magnetic vortex phase in a certain range of applied magnetic field [92, 93]. Relatively few studies have appeared on $Cr_{11}Ge_{19}$. In early work, Zagryazhskii *et al.* [101] reported $Cr_{11}Ge_{19}$ to be a semimetallic ferromagnet with a transition temperature of $\sim$ 86 K. Intriguingly, they point out the lack of a lambda anomaly at the ferromagnetic transition temperature in their specific heat measurements. A linear muffin tin orbital (LMTO) calculation of electronic

density of states [103] indicated it to be a low moment itinerant ferromagnet. A study of thermoelectric properties on a single crystal above room temperature reported the material to have a metallic behavior with dominant p-type conductivity and a relatively low resistivity [104].

In this chapter we report magnetization, transport, and thermodynamic properties of $Cr_{11}Ge_{19}$ together with results obtained from electronic structure calculations. Both the experimental results and calculations indicate that $Cr_{11}Ge_{19}$ is a good example of an itinerant electron ferromagnet, with signatures of both spin wave excitations and magnetic fluctuations apparent in the data. Although no direct evidence for a helimagnetic or other exotic magnetic ground state has been found in the polycrystalline samples we have studied, the behavior of this material is unusual in several respects and deserves further study in single crystal form.

## 4.2 Experimental details

Polycrystalline samples were prepared and studied. Stoichiometric amounts of high purity Cr pieces (99.999 %) and Ge pieces (99.9999 %) were arc-melted in an argon atmosphere. The resulting ingot was then sealed in a quartz tube and annealed at 900 $^o$C for one week. The annealed ingot was then ground into fine powder inside a He-filled glove box and pressed into a pellet, which was again sealed in an evacuated quartz tube and annealed at 900 $^o$C for another week.

Single crystal growth was also attempted using two different techniques: a flux method using Ge as a self flux and a modified Bridgman method. Both growths were carried out using a molar ratio of Cr : Ge = 20 : 80 of the starting materials. In the flux method, a total charge consisting of 7 g of Ge pieces (99.9999 % pure) and Cr powders (99.99 % pure) were loaded in a 5 ml alumina crucible. A catch crucible containing quartz wool was mounted on top of a growth crucible and both were sealed in a silica ampoule under vacuum. The sealed ampoule was heated to 1100 $^o$C over 10 hours and homogenized at 1100 $^o$C for 30 hours, furnace cooled to 1000 $^o$C and then

slowly cooled to 910 $^o$C at the rate of 2 $^o$C per hour. Once the furnace reached 910 $^o$C, the excess flux was decanted from the crystals. Single crystals with cubic shape and of an average dimension of about 0.5 mm were obtained. The so called modified Bridgman method was employed by first melting a total charge of 10 g of Ge pieces (99.9999 % pure) and Cr pieces (99.999 %) in an argon atmosphere. The arc-melted ingot was broken into pieces and loaded into a well-cleaned quartz tube of 14 mm inner diameter with a pointed bottom forming a Bridgman crucible. The tube was placed in an upright position inside a box furnace and first heated to 1100 $^o$C over 10 hours and homogenized for 30 hours. It was then cooled quickly to 1000 $^o$C and then slowly cooled to 900 $^o$C at the rate of 2 $^o$C per hour which was subsequently furnace-cooled to room temperature. Tiny cube-shaped crystals with a typical dimension of 0.1 mm were always observed in the middle of the resulting boule.

Room temperature x-ray diffraction on powders from pulverized single crystals confirmed single phase for the crystals obtained in both techniques. The atomic ratio was studied using a Hitachi bench-top scanning electron microscope (SEM) with a Bruker energy dispersive x-ray spectrometer (EDS). The atomic percentages of Cr and Ge observed are 42 at.% and 58 at.%, respectively, which is within the expected uncertainty for standardless measurements on irregular surfaces. Crystals obtained from modified Bridgman method were too small for convenient characterization, while the relatively larger crystals grown by flux method typically had some residual Ge flux on the crystal surface. Therefore in this study we characterized polycrystalline material, which was $\geq$98% pure based on powder diffraction and EDS measurements.

All the measurements were carried out in pieces cut from the same compact polycrystalline pellet that was determined to be 82% of the theoretical density. X-ray powder diffraction was performed at room temperature using a PANalytical X'Pert powder diffractometer for phase identification and structural refinement. X-ray powder patterns were also obtained every 20 K on cooling from room temperature down to 11 K. DC magnetization measurements were performed using a Quantum Design magnetic property measurement system (MPMS). AC susceptibility, specific

heat, and resistivity measurements were conducted in a Quantum Design physical property measurement system (PPMS). AC susceptibility was measured by using a drive coil frequency of 85 Hz and an excitation field of 10 Oe at different applied DC magnetic fields from 0 to 10 kOe. Specific heat measurements were performed on a small piece of 27.5 mg. Resistivity was measured using platinum wires and Epotek H20E silver epoxy in a four-wire configuration on a 1.9×1.2× 1.4 $mm^3$ rectangular bar. The temperature dependence of the elastic moduli was obtained using resonant ultrasound spectroscopy (RUS) on a 1.261 x 2.122 x 3.899 $mm^3$ polycrystalline pellet using a custom designed probe inserted into a Quantum Design Versalab [105].

## 4.3 Results and discussion

### 4.3.1 Crystal chemistry

$Cr_{11}Ge_{19}$ crystallizes in the $Mn_{11}Si_{19}$ structure type in a family of compounds known as Nowotny chimney ladders (NCLs). These are a series of intermetallic compounds with composition $T_nX_m$, where 2>m/n>1.25 [104]. Here $T$ is a transition metal element and $X$ is a main group metal. These compounds have a complex structure in which $T$ atoms form 4-fold helices inside of which $X$ atoms form separate helices [106]. NCLs have been found to follow the 14 electron rule, according to which a NCL compound having 14 valence electrons (VEL) per main group metal atom should be semiconductor and one with VEL less than 14 should be metal [104]. The rule holds for $Cr_{11}Ge_{19}$ as it has total of 12.9 valence electrons per Ge atom and is known to have metallic behavior. Figure 4.1 shows the structure of $Cr_{11}Ge_{19}$. It has a very long c axis (52.321 Å) as shown in Fig. 4.1(a). Figure 4.1(b) shows the view down the c axis. The Cr atoms (black) form helices, shaped like chimneys, within which the helices of Ge atoms (orange) reside. In Fig. 4.1(c) we emphasize the helices of Cr and Ge. The Cr-Cr distance is the shortest along the helix (3.124 - 3.138 Å) [100],

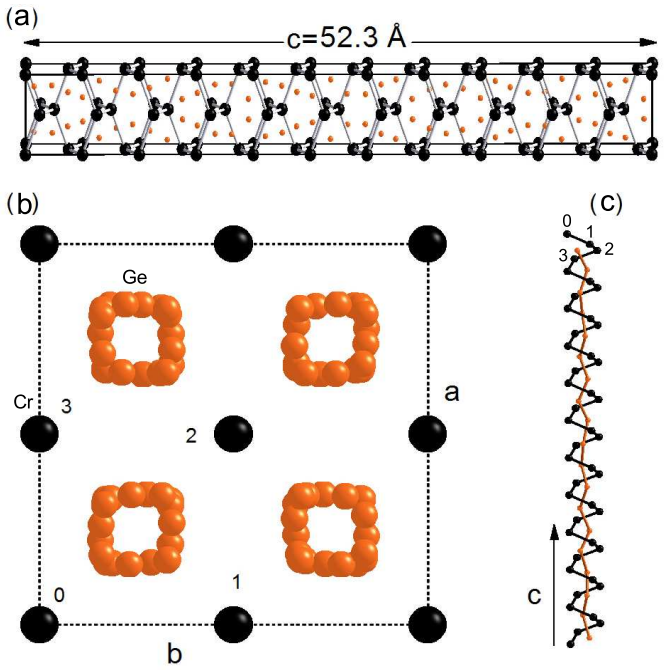


**Figure 4.1:** The tetragonal $Cr_{11}Ge_{19}$ structure. (a) Arrangement of Cr and Ge atoms in the complex Nowotny chimney ladder structure emphasizing the long c axis (52.321 Å). (b) A view down the c axis. One turn of the Cr helix is emphasized on moving from 0, 1, 2, and 3 counterclockwise. (c) A perpendicular view showing a Ge helix within a Cr helix. The Cr atoms are shown as black (larger) balls, and the Ge atoms are shown as orange (smaller) balls.

and hence, substantial Cr-Cr interaction can be expected in the direction of the helix. However, the structure is much more complex due to the presence of large number of atoms (120) in the unit cell. It has 12 inequivalent Cr sites and 10 inequivalent Ge sites. We used the reported structure [100] for the Rietveld refinement of the room temperature x-ray powder pattern. The fit is reasonably good considering the complex structure as shown in Fig. 4.2. Atomic positions and occupancies were not refined because of the difficulty introduced by the large number of atoms in the unit cell. The inset in Fig. 4.2 shows a magnified part of the fit at higher angles in which indexed peaks are seen more clearly. Lattice constants obtained from the fit are a

= 5.805 Å and c = 52.321 Å, which are in good agreement with previously reported values [101, 103].

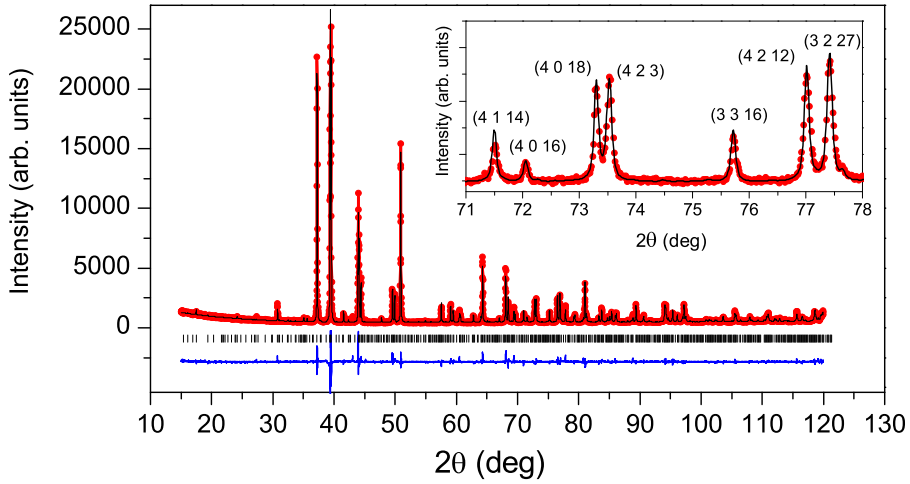


**Figure 4.2:** Rietveld refinement of x-ray powder pattern of $Cr_{11}Ge_{19}$ collected at room temperature.

### 4.3.2 DC magnetization

Figure 4.3 shows the temperature dependence of magnetization of $Cr_{11}Ge_{19}$ in an applied field of 10 kOe. As the sample is cooled the transition from a paramagnetic state to an ordered ferromagnetic state is clearly visible. The inset shows the Curie-Weiss fit of $\chi^{-1} = (T - \theta_{CW})/C$ to the high temperature part of the inverse susceptibility above 220 K. The parameters obtained are Curie constant $C = 5.34\ K\ cm^3\ mol^{-1}\ F.U.^{-1}$ and the Curie-Weiss temperature $\theta_{CW} = 128.6$ K. The effective moment per mole of chromium atom $p_{eff}$ calculated from the Curie constant is 1.97 $\mu_B$.

Figure 4.4(a) shows the magnetization $M$ of $Cr_{11}Ge_{19}$ as a function of field at several temperatures. At low temperatures $M$ saturates above 20 kOe. The saturation

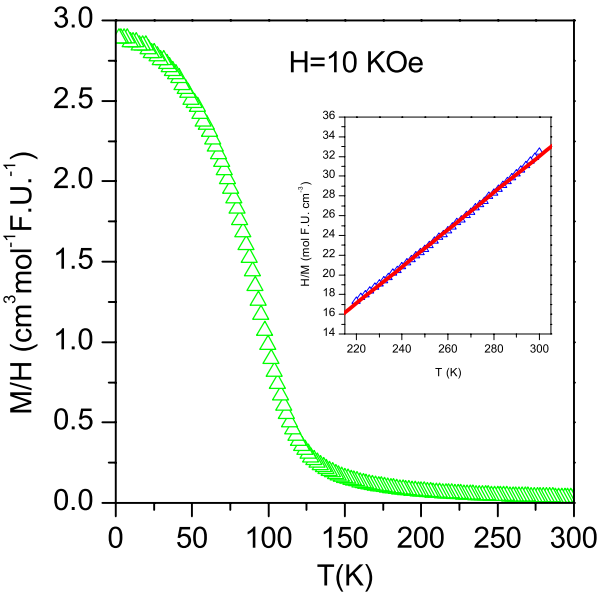


**Figure 4.3:** $M/H$ as a function of temperature measured at an applied field of $H$ = 10 kOe. Inset shows the fit to the Curie-Weiss law.

is suppressed with increasing temperature, and $M$ versus $H$ becomes a straight line at higher temperatures. The saturated magnetic moment obtained in the ordered state is 0.49 $\mu_B/Cr$. Within the Stoner model, itinerant ferromagnets obey the relation

$$M(H,T)^2 = -\frac{A}{B} + \frac{1}{B}(\frac{H}{M(H,T)}), \tag{4.1}$$

where $A$ and $B$ are independent of $H$ [107–109]. $A$ is a temperature dependent term and vanishes at $T_C$. This should give straight lines on an Arrott plot [110], $M^2(H,T)$ versus $H/M(H,T)$, with a straight line passing through the origin at the transition temperature. In Fig. 4.4(b) we show Arrott plots for $Cr_{11}Ge_{19}$. These Arrott plots are not perfectly straight lines as expected and observed in itinerant ferromagnets like $ZrZn_2$, $Ni_3Al$, and NiPt alloys [107]. However, the Arrott plots for $Cr_{11}Ge_{19}$ are similar to those observed in the case of MnSi [111] and the layered itinerant ferromagnet LaCoAsO [112]. Such behavior was explained by Takahashi [113], who in his theory added zero point local spin fluctuations, which were previously neglected.

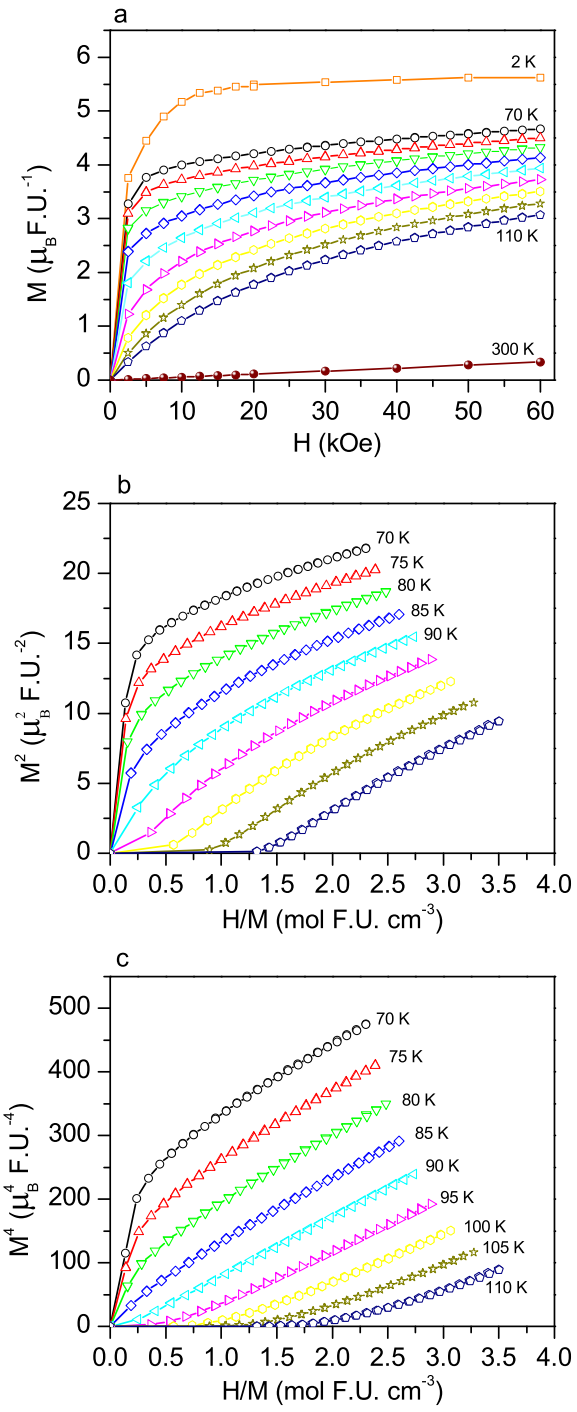


**Figure 4.4:** (a) $M$ versus $H$ for $Cr_{11}Ge_{19}$ at indicated temperatures. The plots from 70 K to 110 K are in the interval of every 5 K. (b) $M^2$ versus $H/M$ (Arrott plot) and (c) $M^4$ versus $H/M$ for $Cr_{11}Ge_{19}$ at indicated temperatures.

This theory predicts

$$h = [\frac{T_A}{3}(2+\sqrt{5})T_c]^2 m^5, \tag{4.2}$$

where h = $2\mu_B$H and m = $2M(T)/N_o$ magnetization per magnetic site. The parameter $T_A$ characterizes the dispersion of the static magnetic susceptibility in wave-vector ($q$) space. From Eq. (2) it can be seen that $M^4$ versus $H/M$ should be a straight line at $T_C$ . Such a linear relation has been confirmed in MnSi and $Fe_{1-x}Co_xSi$ [113, 114]. Figure 4.4(c) shows the $M^4$ versus $H/M$ curve of $Cr_{11}Ge_{19}$ which shows straight line behavior. The plots are almost a straight line between 85 and 90 K. We estimate the Curie temperature to be 88 K.

### 4.3.3 AC susceptibility

Figure 4.5 shows the temperature dependence of the real part of the AC susceptibility measured in the applied DC fields as indicated. At zero applied DC bias field (not shown) the AC susceptibility increases quickly with decreasing temperature in the vicinity of the transition temperature and decreases slightly upon further cooling. The effect of external fields is quite striking. First, the field remarkably suppresses the ac susceptibility. Second, a shoulder appears at lower fields near $T_C$ which is defined by two peaks, one sharp peak in the vicinity of the transition temperature and the other broader peak below $T_C$. With the increase in field, the peak near $T_C$ gets suppressed and shifts slightly towards higher temperature, whereas the broader peak below $T_C$ becomes broader and shifts towards lower temperature and is almost completely suppressed at H = 10 kOe. Similar behavior has been observed in a PdMn alloy [115], $GdFe_2Zn_{20}$ [116], MnSi [117] and FeGe [118]. This AC susceptibility behavior in $GdFe_2Zn_{20}$ has been interpreted as a manifestation of both the itinerant and the local moments in the material as it contains both 4f (local) and 3d (itinerant) moments. In this material, the peak observed near $T_C$ shows the behavior of local moments as observed in $CeAgSb_2$ [116], and the broader peak at lower temperature is reminiscent of itinerant behavior as observed in $ZnZr_2$ [116]. MnSi and FeGe show

similar AC susceptibility behavior, but are known to have no local moments. In these later two materials, the $A$ phase has been tracked out by AC susceptibility measurements conducted on single crystals [117, 118].

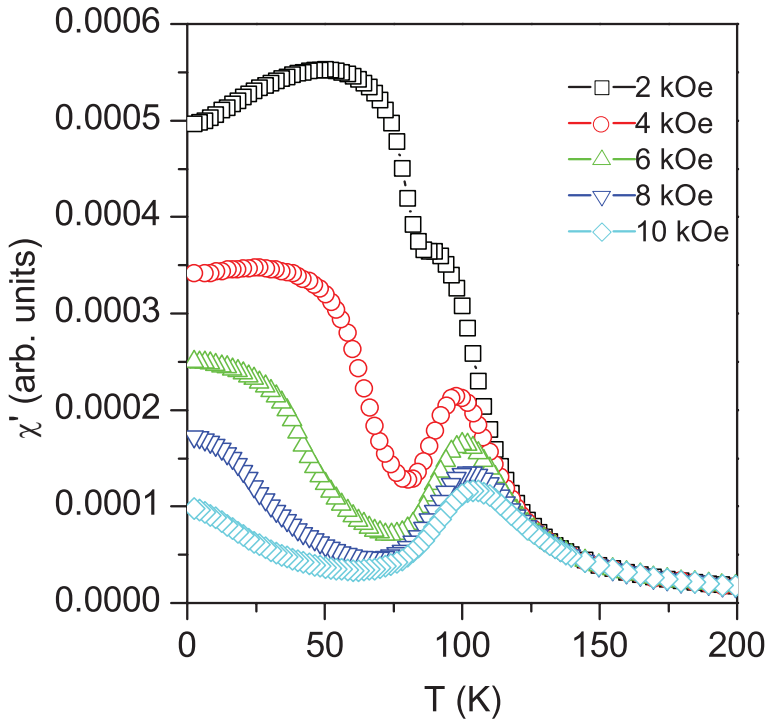


**Figure 4.5:** AC susceptibility of $Cr_{11}Ge_{19}$ as a function of temperature at indicated applied fields.

### 4.3.4 Heat capacity

The molar heat capacity of $Cr_{11}Ge_{19}$ from 2 to 200 K is shown in Fig. 4.6. There is no obvious lambda anomaly near $T_C$, but upon closer inspection $T_C$ is marked by a small kink as shown by the arrow in Fig. 4.6. Zagryazhskii *et al.* reported that they observed a monotonic increase in the specific heat capacity from 55 to 300 K with no lambda anomaly [101]. The small kink observed near $T_C$ is suppressed upon application of the magnetic field. Figure. 4.7 shows the specific heat capacity as a function of temperature between 50 and 110 K measured in zero field and at 50

kOe. The inset shows the difference curve obtained by plotting $\Delta C_p$ (the difference between $C_p$ measured in a 50 kOe field and in a zero applied field) as a function of temperature giving a clear peak near $T_C$.

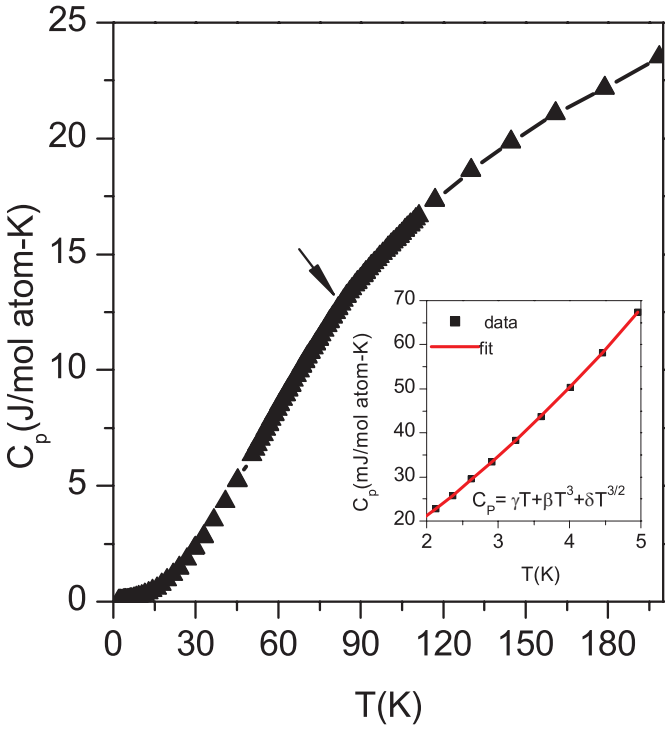


**Figure 4.6:** Temperature dependence of molar heat capacity of $Cr_{11}Ge_{19}$. Inset shows the low temperature fit of the heat capacity.

Mohn and Hilscher [119] have discussed the influence of spin fluctuations on the specific heat of itinerant ferromagnets. In Stoner theory, the magnetic contribution vanishes above $T_C$. In contrast, in systems with spin fluctuations, it is only the macroscopic moment that disappears at $T_C$ as spin fluctuations persist above the ordering temperature. The magnetic contribution to the discontinuity in the specific heat at the transition temperature in case of pure single particle excitations is given by $\Delta C_m = \frac{M_o^2}{\chi_o T_C}$. When spin fluctuations are taken into account, the discontinuity is given by $\Delta C_m = \frac{M_o^2}{2\chi_o T_C}(\frac{1}{2}t_c^4 + t_c^2 + \frac{1}{2})$, where $M_o$ is the spontaneous magnetization, $\chi_o$ is the initial ferromagnetic susceptibility, $T_C$ is the transition temperature, and $t_c$

$= T_C/T_C^s$ with $T_C^s$ being the Curie temperature derived from the pure Stoner type behavior [119]. In $Cr_{11}Ge_{19}$ the discontinuity in the specific heat at $T_C$ calculated for pure Stoner type excitations is 1.2 *J (mol-atom)*$^{-1}$ $K^{-1}$. This value is small enough to explain the absence of a well-defined lambda anomaly in the specific heat capacity near the ferromagnetic transition. But, there is considerable uncertainty in the calculation. The spontaneous magnetization $M_o$ is calculated by using the theory applicable for an itinerant ferromagnet [120] by fitting straight lines obtained at higher fields in the Arrott plot even though the Arrott plot in this material does not behave perfectly as in the case of systems like $ZrZn_2$ [121]. There can also be appreciable uncertainty introduced by $\chi_o$, which might include other components than only the spin susceptibility (e.g., a diamagnetic component). It should be noted that we have not included the contribution due to spin fluctuations in the calculation because of the difficulty introduced by the large number of electrons (1680 per unit cell) in estimating $T_C^s$ from band structure calculations. Inclusion of spin fluctuations further decreases $\Delta C_m$. In case of maximum spin fluctuations $\Delta C_m$ is reduced by a factor of 4. Thus, the presence of spin fluctuations in the material reduces the possibility of getting a sizable discontinuity in specific heat at the transition temperature even if some uncertainty might have been introduced in the calculation of $\Delta C_m$.

The low temperature specific heat data could not be well modeled by $C_p = \gamma T + \beta T^3$. This indicates additional excitations may be contributing to the heat capacity at low temperature. Since this material is magnetically ordered below 88 K, magnetic excitations were considered by inclusion of a term in $C_p$ proportional to $T^{\frac{3}{2}}$ [122]. This resulted in a good fit to the data as shown in the inset of Fig. 4.6. The fit yields the electronic heat capacity coefficient $\gamma = 7.26\ mJ/molK^2$, the phonon specific heat coefficient $\beta = 0.06\ mJ/molK^4$, and the magnetic specific heat coefficient $\delta = 2.18\ mJ/molK^{5/2}$. The Debye temperature determined from $\beta$ is 319 K. Forcing a fit without the magnetic term gives a much lower value for the fitted Debye temperature ($\sim$ 240 K). Elastic constant data presented below give a Debye temperature of 340 K, further justifying the inclusion of spin excitations in modeling the heat capacity.

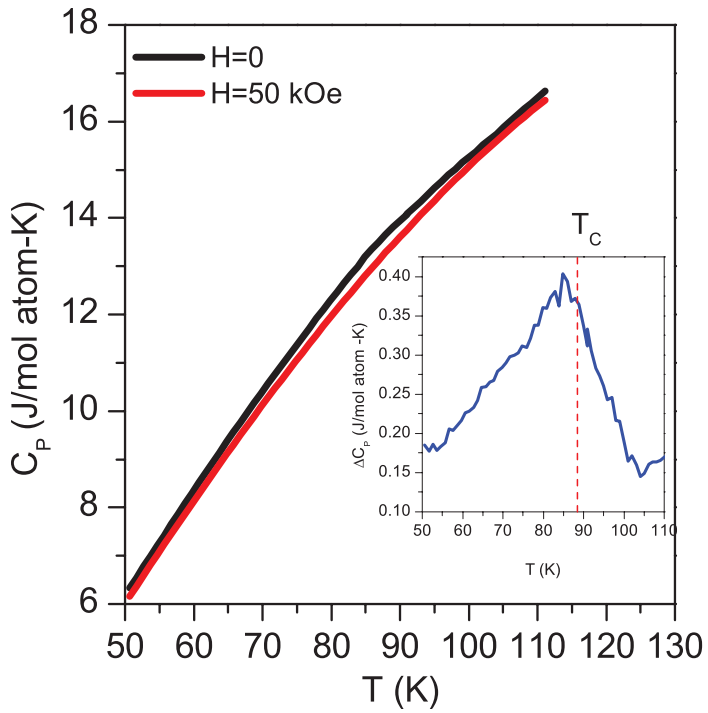


**Figure 4.7:** Heat capacity of $Cr_{11}Ge_{19}$ in ambient field and 50 kOe. The inset shows $\Delta C_p = C_p(H = 0)$ - $C_p(H = 50\ kOe)$.

### 4.3.5 Resistivity and magnetoresistance

Electrical resistivity of $Cr_{11}Ge_{19}$ vs temperature is plotted in Fig. 4.8. The temperature dependence of the resistivity is metallic over the whole temperature range. A slope change is observed at $\sim$ 90 K, which is consistent with a significant loss of spin-disorder scattering upon magnetic ordering. The $T_C$ inferred from resistivity is in good agreement with the value of $T_C$ obtained from magnetization measurements. The room temperature value of electrical resistivity, 0.35 $m\Omega\ cm$, is in good agreement with the value (0.345 $m\Omega\ cm$) reported by Zagryazhskii *et al.* [101] measured on a polycrystal sample and is about a factor of 2 higher than the value reported by Caillat *et al.* [104] on a single crystal sample. The observed excess value of resistivity can be attributed to grain boundary scattering in the polycrystalline sample. The residual resistance ratio ($\rho_{300K}/\rho_{2K}$ ) is large, having a value of 89. The inset in Fig. 4.8 shows

the magnetoresistance defined as $\Delta\rho/\rho$, where $\Delta\rho = \rho_H$ - $\rho$ with $\rho_H$ and $\rho$ being the resistivity measured at 50 kOe and zero applied magnetic field, respectively. Negative magnetoresistance is observed below 150 K with the largest effect in the vicinity of $T_C$ where fluctuations are the strongest.

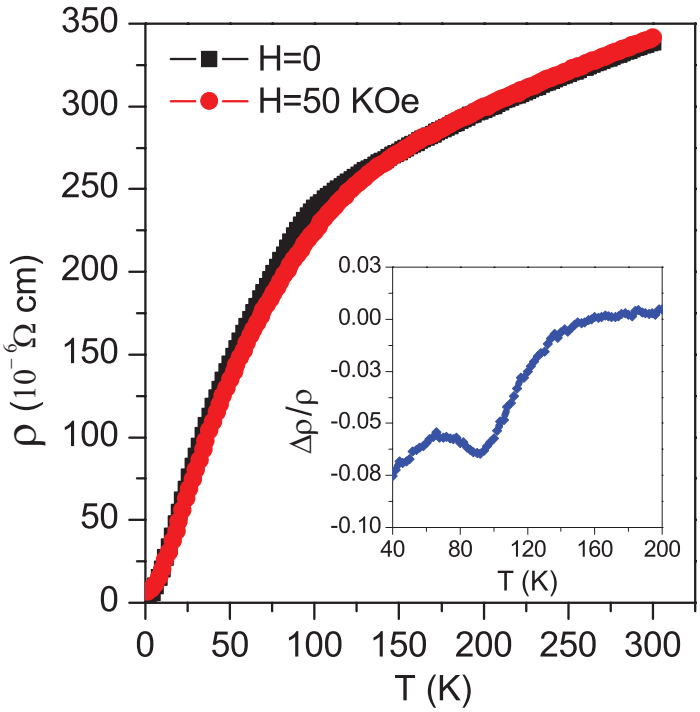


**Figure 4.8:** Resistivity of $Cr_{11}Ge_{19}$ as a function of temperature. Inset shows the magnetoresistance.

### 4.3.6 Thermal expansion and elastic moduli

The temperature dependence of the lattice parameters is plotted in Fig. 4.9. Both *a(T)* and *c(T)* are normalized by dividing with the corresponding room temperature values. No structural phase transition is observed on decreasing the temperature down to 11 K. However, the temperature dependence of the lattice parameters *a(T)* and *c(T)* show dramatic differences below the magnetic ordering temperature. Below $T_C$, *a(T)* decreases continuously down to 11 K, whereas *c(T)* shows a region of negative

thermal expansion. This behavior shows the presence of magneto-elastic coupling. This coupling is also evident in the temperature dependence of elastic constants as discussed below.

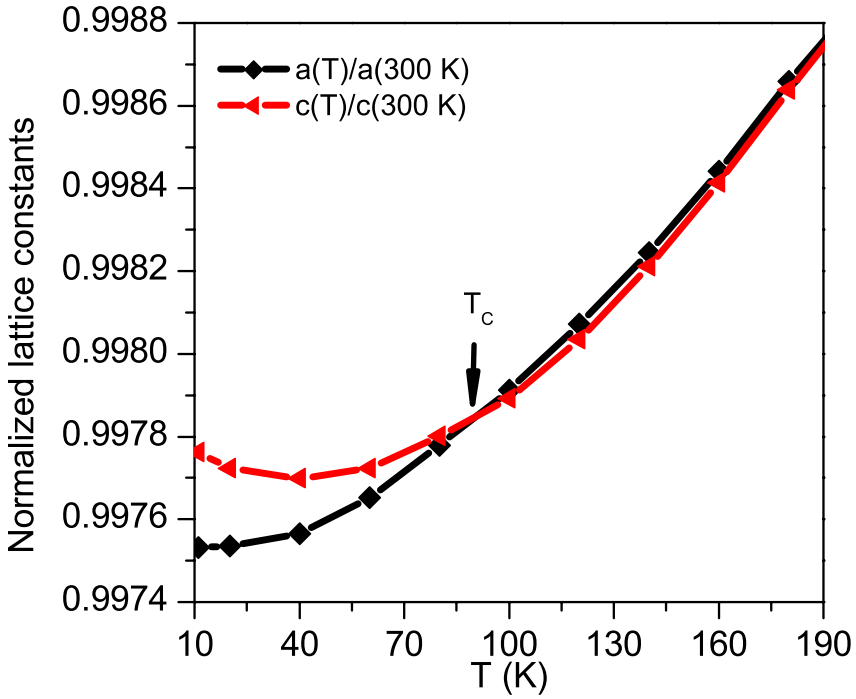


**Figure 4.9:** Temperature dependence of lattice constants of $Cr_{11}Ge_{19}$. The lattice constants are normalized by dividing with values at 300 K.

Resonant ultrasound spectroscopy (RUS) measurements were conducted to obtain the temperature dependence of the longitudinal ($C_{11}$) and shear ($C_{44}$) elastic moduli. $C_{11}$ and $C_{44}$ were used to obtain the shear and longitudinal sound velocities. For polycrystalline samples, the shear velocity is given by [123] $v_s = \sqrt{\frac{C_{44}}{d}}$ and the longitudinal velocity is given by $v_l = \sqrt{\frac{C_{11}}{d}}$, where $d$ is the density of the sample. Anderson's formula [124] was then used to calculate the Debye temperature from the average sound velocity just above the transition temperature (90 K). The Debye temperature obtained is 340 K, which is consistent with the Debye temperature estimated from $C_p$(T) above.

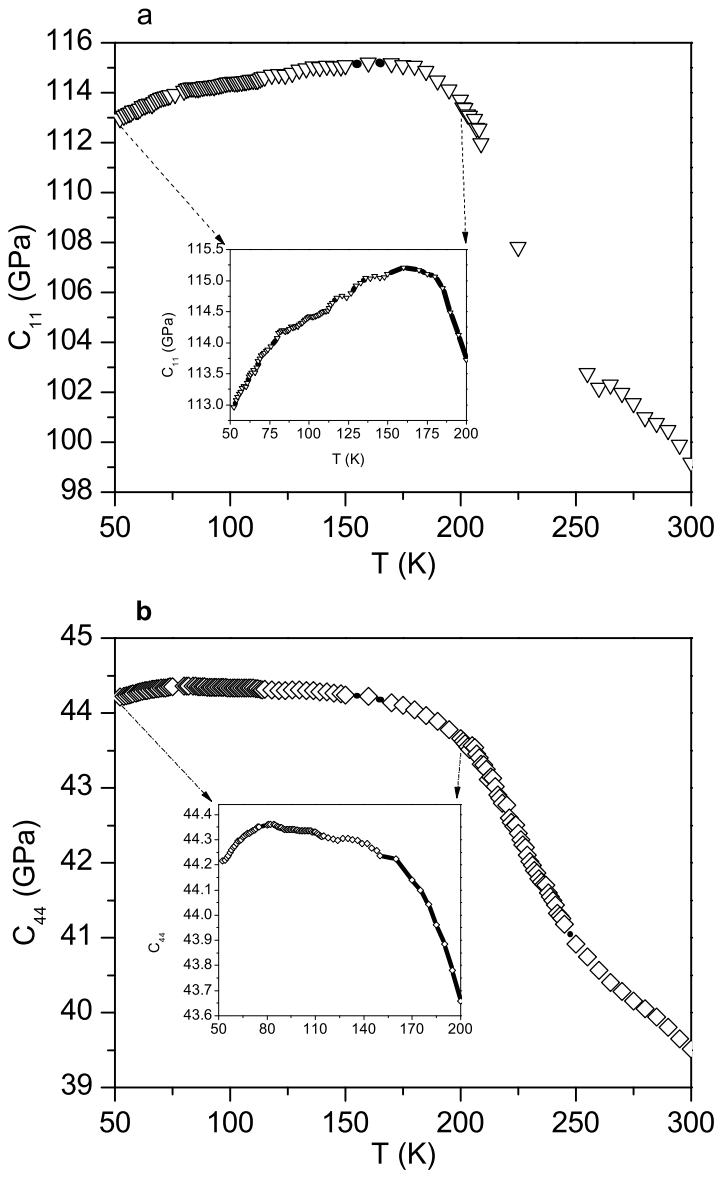


**Figure 4.10:** Variation of elastic moduli (a) $C_{11}$ and (b) $C_{44}$ as a function of temperature.

The temperature dependence of the longitudinal $C_{11}$ and shear $C_{44}$ elastic moduli of $Cr_{11}Ge_{19}$ is plotted in Figs. 4.10(a) and 4.10(b), respectively. In both figures the insets focus on the region from about 50 to 200 K so as to show the behavior near the

Curie temperature. Between 220 and 250 K the ultrasonic absorption in the sample became so great that for several temperatures not enough resonances were observed to allow for an accurate determination of both elastic moduli. However, a few resonances that depend almost exclusively on $C_{44}$ remained visible throughout this region, which allowed us to follow the shear modulus over the entire temperature range. The typical temperature dependence of elastic moduli is that at higher temperatures they increase linearly with decrease in temperature and approach absolute zero with zero slope [125, 126]. In $Cr_{11}Ge_{19}$, deviation from the normal behavior is observed in both the longitudinal and shear elastic constants. $C_{11}$ starts softening well above the Curie temperature without showing any remarkable feature at the transition temperature. $C_{44}$, on the other hand, increases with decreasing temperature down to $T_C$ and then softens upon further cooling. This demonstrates the interaction between the magnetic ordering and the crystal lattice in $Cr_{11}Ge_{19}$. This behavior is reminiscent of the Invar effect in ferromagnetic materials and is in accord with the prediction of Landau's theory of second order magneto-elastic coupling [127].

### 4.3.7 Electronic structure calculations

Experimental results have indicated that some of the properties of $Cr_{11}Ge_{19}$ deviate from what is expected in an ordinary ferromagnet. In an attempt to understand these unusual behaviors we have performed first principles calculations of $Cr_{11}Ge_{19}$ in both a nonmagnetic state and a collinear ferromagnetic state, using the all-electron code WIEN2K [128] in the generalized gradient approximation (GGA) of Perdew, Burke, and Ernzerhof [129]. Atomic sphere radii of 2.41 and 2.13 Bohr radii were used for the Cr and Ge atoms, respectively, and an $RK_{max}$ of 7, where R is the minimum atomic sphere radius and K is the largest plane-wave vector used in the expansion. Calculations proceeded slowly due to the large number (1680) of electrons in the unit cell; final results were converged to within 2 meV per unit cell, a small value considering the large unit cell. We find strong evidence for a magnetic ground state of

$Cr_{11}Ge_{19}$, with the ferromagnetic ordering some 87 meV per Cr atom lower in energy than the nonmagnetic ground state. The ordered moment averages approximately 1 $\mu_B$ per Cr atom, but is unevenly distributed amongst the 12 inequivalent Cr sites in the unit cell, with moment per site ranging from 0.3 to 1.7 $\mu_B$, which we interpret as indirect evidence of the propensity of the system towards a noncollinear ground state. This interpretation of a noncollinear ground state is based upon the DFT constraining of the moments to be collinear, which will necessarily reduce the value of the calculated moment for those spins which in the actual physical system are not collinear. This interpretation is strengthened by the fact that the reported [100] Cr-Cr nearest neighbor distances vary only from 3.124 to 3.138 Å amongst the inequivalent Cr sites, so that the differences in calculated moment are more likely to be an artifact of the collinearity assumed rather than indicative of physically distinct moment values. The calculated average moment is somewhat higher than the observed experimental value of 0.5 $\mu_B$; this overestimation sometimes occurs with the GGA. Due to the time-consuming nature of the calculations we have not carried out additional local density approximation (LDA) calculations, which may better match the actual ordered moment.

To better understand the electronic structure we have calculated the electronic density of states (DOS) in both the magnetic and nonmagnetic states, using the first principles calculated band structure with approximately 300 $k$ points in the full Brillouin zone. These DOS are depicted in Fig. 4.11. The nonmagnetic state [Fig. 4.11(a)] shows a huge peak in the density of states exactly at the Fermi energy, highly favorable towards a Stoner-type ferromagnetic instability (recall the Stoner criterion $IN_0 > 1$, where I is the exchange correlation integral and $N_0$ the Fermi level density of states). This DOS is in rough agreement with the non-self-consistent band structure calculations of Ref. 103. With I for Cr taken from Ref. 130 as 0.38 eV and the Fermi level DOS of approximately 5.7/Cr/eV, the Stoner criterion is well satisfied, and as described earlier this fits with the magnetic ground state we find.

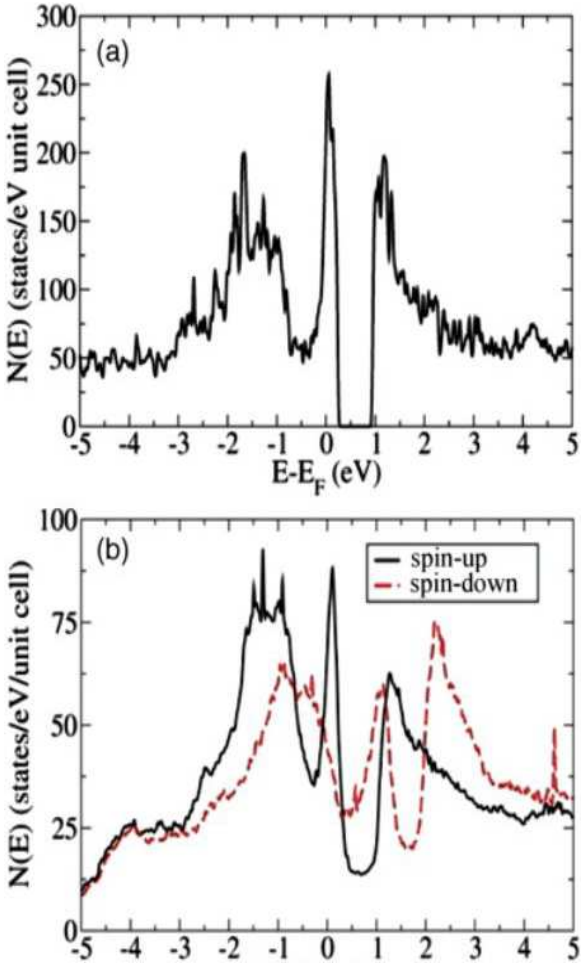


**Figure 4.11:** Electronic density of states of $Cr_{11}Ge_{19}$ in (a) nonmagnetic state and (b) magnetic state.

We turn now to the magnetic state DOS [Fig. 4.11(b)]. The majority spin-up DOS still has a peak very near $E_F$, but this peak is much lower than in the nonmagnetic case. Substantial spectral weight for the spin-up states is transferred below $E_F$, as is expected for the majority spin, while the spin-down DOS is somewhat more equally distributed above and below $E_F$. We note also that the strongly magnetic nature of this system is paralleled by the spin-up and spin-down DOS not coinciding until several eV from the Fermi level. We note also that the band gap has disappeared, with instead a deep minimum in the spin-up DOS just above $E_F$ and a somewhat less

deep minimum in the spin-down DOS. This band gap absence, to be compared with its existence in the nonmagnetic state, is again indicative of the strong magnetism present in this material.

## 4.4 Conclusion

The results presented here, both from experiment and first principles calculations, indicate unusual magnetism in $Cr_{11}Ge_{19}$. The behavior of the magnetization and heat capacity suggest itinerant, noncollinear ferromagnetism with a Curie temperature near 88 K, and this description is supported by first principles calculations. The magnetism appears to be strongly coupled to the crystal lattice, as indicated by anomalous behavior of the lattice parameters and the elastic moduli at and below $T_C$. The influence of spin-wave excitations is observed in the heat capacity at low temperature. Interestingly, some of the properties are similar to those of MnSi and other itinerant ferromagnets. It is interesting to speculate about possible helimagnetism in $Cr_{11}Ge_{19}$, based on the observed properties and the nature of the crystal structure. However, the present data cannot confirm the magnetic structure, and single crystals of suitable size for neutron diffraction are not yet available. Our observations clearly point to complex and interesting magnetism in this compound, and show that further study would be of interest.

# Chapter 5

# Magnetic phase transition in chiral helimagnet $Cr_{1/3}NbS_2$

A similar version of this chapter appeared as "Magneitc phase transition in chiral helimagnet $Cr_{1/3}NbS_2$", N. J. Ghimire, M. A. McGuire, D. S. Parker, B. Sipos, S. Tang, J.-Q. Yan, B. C. Sales, and D. Mandrus, Phys. Rev. B **85**, 104403 (2013).

## 5.1 Introduction

$Cr_{1/3}NbS_2$ crystallizes in a noncentrosymmetric hexagonal space group $P6_322$ belonging to the point group $D_6^6$ [131], one of the symmetry groups in which ferromagnets have been theoretically predicted to have a skyrmion lattice [95]. It orders magnetically into a helimagnetic ground state with a period of about 480 Å below about 116 - 127 K and is known to have metallic behavior below room temperature [132–135]. The spins are arranged ferromagnetically in the *ab* plane and the helix is along the *c* axis. The effect of magnetic field in the *ab* plane has been found to be dramatic with a metamagnetic transition observed at an applied field near 1200-1500 Oe [133]. A nonlinear periodic magnetic state called a soliton lattice was predicted for this material [76, 136] and recently observed in a thin specimen

studied with small angle electron diffraction and Lorentz force microscopy [21]. A magnetic field applied perpendicular to the direction of the helix destabilizes the helical structure gradually into a soliton lattice with an eventual incommensurate-to-commensurate transition into a ferromagnetic state at the critical field of 2300 Oe. Manipulation of the spin spiral with magnetic field has generated interest in this material for spintronics applications [34, 36, 137, 138].

The first helimagnetic ground state in this material was experimentally observed by Miyadai *et al.* [133] by means of small angle neutron scattering conducted on a powder sample, which was in accordance with the prediction of the helimagnetic structure by Moriya and Miyadai [139] based on the magnetic measurements and the subsequent theoretical interpretation in terms of the DM interaction in a noncentrosymmetric magnet. In earlier studies Parkin *et al.* [134, 135] found it to order ferromagnetically below 120 K with the basal plane being the easy axis.

In this chapter, we present experimental results obtained on single crystals of $Cr_{1/3}NbS_2$ together with results from electronic structure calculations. The temperature dependence of dc susceptibility and the magnetization curves is reported both parallel and perpendicular to the $c$ axis. The temperature dependence of electrical resistivity, specific heat capacity, thermal conductivity, and Seebeck coefficient in zero magnetic field and their behavior in magnetic fields applied perpendicular to the $c$ axis are investigated. Results of band structure and density of states (DOS) calculations are presented both in the non-magnetic and magnetic states.

## 5.2 Crystal Chemistry

$Cr_{1/3}NbS_2$ crystallizes in the $Nb_3CoS_6$, hp20 structure type [132]. It forms a hexagonal layered structure, as depicted in Fig. 5.1(a), containing 20 atoms per unit cell. Twelve sulfur atoms occupy the general site. There are six niobium atoms in two inequivalent

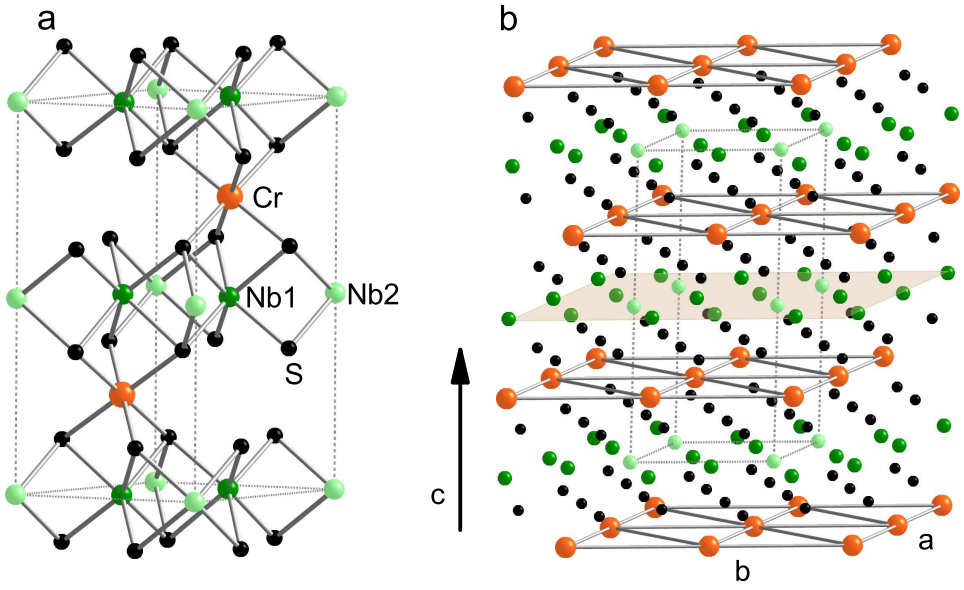


**Figure 5.1:** (a) Hexagonal crystal structure of $Cr_{1/3}NbS_2$. The intercalated chromium atoms occupy the octahedral interstitial holes between the trigonal prismatic layers of 2H-$NbS_2$. (b) Structure of $Cr_{1/3}NbS_2$ emphasizing the layers of Cr atoms in the *ab*-plane. The Cr-Cr distance is shortest in the plane. The dotted lines show the unit cell. The biggest (orange) balls represent Cr atoms, the medium (green) balls represent Nb atoms, and the smallest (black) balls represent S atoms. Nb atoms are in two inequivalent sites labeled as Nb1 and Nb2.

positions: 4f and 2a. The Cr atoms are intercalated in the octahedral holes (2c sites) between the trigonal prismatic layers of 2H-$NbS_2$. The unit cell parameters obtained from the x-ray data collected from the powdered crystals are $a$ = 5.741 Å and $c$ = 12.101 Å which are in good agreement with the reported values [132, 133]. The Cr-Cr distance is closest within the layer in the *ab* plane (5.741 Å). Along the $c$ axis, the nearest Cr-Cr distance is 6.847 Å. $Cr_{1/3}NbS_2$ belongs to a large family of layered materials that are formed by intercalation of transition metal elements within the layers of the first row transition metal dichalcogenides. The structure depends on the amount of intercalation in the layer. In the absence of intercalated atoms, the host transition metal dichalcogenide layers are coupled through weak van der

Waals bonds. The intercalation of a transition metal strengthens the bonding with the possibility of charge transfer from the intercalated atoms to the transition metal atoms in the layer, which brings about strong changes in the electronic structure and corresponding changes in the electrical transport and magnetic properties [140].

## 5.3 Experimental details

Crystals of $Cr_{1/3}NbS_2$ were grown by chemical vapor transport using iodine as the transport agent [133]. Single crystals of various sizes with dimensions as large as 8 mm $\times$ 7 mm $\times$ 1 mm were obtained. X-ray diffraction from powdered crystals confirmed the $P6_322$ structure and revealed no impurity phases. Energy dispersive x-ray spectroscopy (EDS) results along with the magnetic transition temperature clearly distinguish these crystals to be $Cr_{1/3}NbS_2$ [134, 141]. No iodine was detected in the crystals by the EDS measurements. Magnetic properties were measured using a Quantum Design Magnetic Property Measurement System (MPMS) adopting a field cooling approach. Resistivity, magnetoresistance, thermal conductivity and Seebeck coefficient were all measured in a Quantum Design Physical Property Measurement System (PPMS). A four wire configuration with platinum wires and Epotek H20E silver epoxy were used for the resistivity and magnetoresistance measurements.

## 5.4 Results and Discussion

### 5.4.1 Magnetic properties

Figure 5.2 shows $M/H$ as a function of temperature with the applied magnetic field perpendicular [see Fig. 5.2(a)] and parallel [see Fig. 5.2(b)] to the $c$ axis. With the magnetic field applied perpendicular to the $c$ axis, at the lower field (1 kOe), a small kink is observed at about 117 K. This kink is not observed at 10 kOe. No such kink is observed in $M/H$ versus $T$ when the magnetic field is applied parallel to the

$c$ axis. These results are consistent with previous measurements by Miyadai *et al.* [133]. As the material is known to have helimagnetic ordering in lower fields with the helix directed along the $c$ axis [21], the kink may represent the onset of the helical state. Such a kink has also been observed in other known helimagnets such as MnSi [111], FeGe [142], and $Fe_{1-x}Co_xSi$ [19]. $Cr_{1/3}NbS_2$ follows Curie-Weiss behavior at higher temperatures. The inset in Fig. 5.2(a) shows the Curie-Weiss fit of $\chi = \frac{C}{T-\theta_{cw}}$ to the high temperature part of data measured with an applied field of 1 kOe. The parameters obtained are the Curie constant $C = 2.4$ K cm$^3$ mol $^{-1}$ Cr$^{-1}$ and the Curie-Weiss temperature $\theta_{CW} = 127$ K. The effective moment per mole of chromium atoms, $p_{eff}$, calculated from the Curie constant is 4.4 $\mu_B$, which is consistent with the values reported by Parkin *et al.* [141] (4.3 $\mu_B$ and 4.1 $\mu_B$ for field applied parallel and perpendicular to the $c$ axis, respectively).

The anisotropic nature of the low-temperature magnetism in $Cr_{1/3}NbS_2$ is evident in Fig. 5.3. Applying a field along the $c$ axis [see Fig. 5.3(b)] simply rotates the ordered moments out of the $ab$ plane. This results in a nearly linear increase in $M$ with $H$ up to $H = 20$ kOe. When the field is applied in the $ab$ plane [see Fig. 5.3(a)], more complex behavior is observed, which will be addressed further in the following discussion. The moment saturates to the same value of about 3.2 $\mu_B$/Cr, close to the expected value of 3 for $S = 3/2$, in both orientations. But this occurs at a much lower field when $H$ is applied in the $ab$-plane, indicating a strong preference for the moments to remain perpendicular to the $c$ axis.

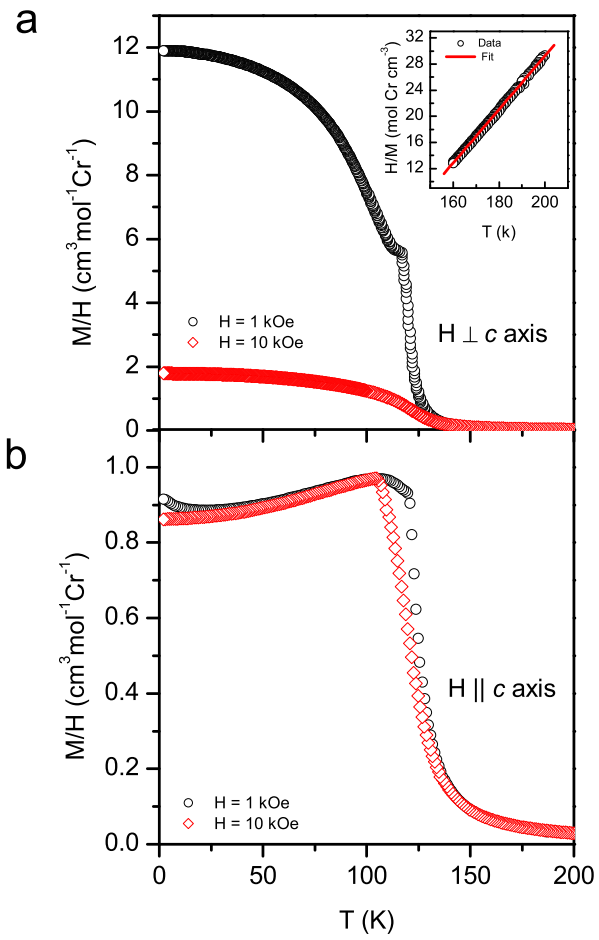


**Figure 5.2:** $M/H$ as a function of temperature at the fields indicated with the magnetic field applied (a) perpendicular to the $c$ axis, and (b) parallel to the $c$ axis. Inset in (a) shows the fit to the Curie-Weiss law for the data taken at 1 kOe above 160 K.

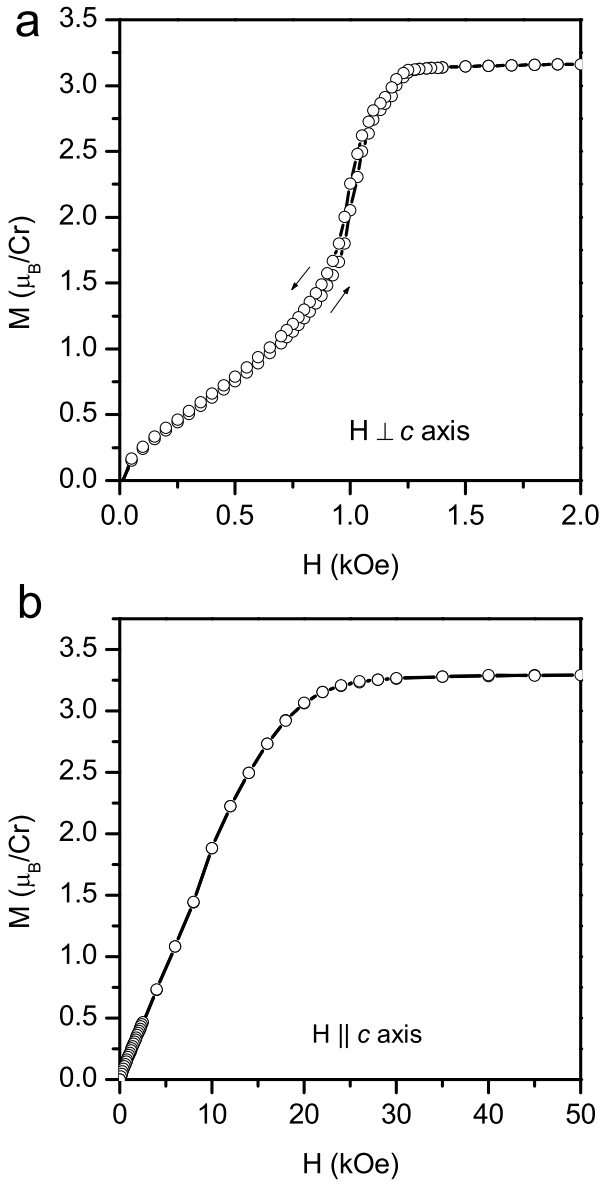


**Figure 5.3:** $M$ vs. $H$ measured at a temperature of 2 K with the magnetic field applied (a) perpendicular, and (b) parallel to the $c$ axis. Note the different scales on the x-axis.

Figure 5.4 shows various magnetic properties near the magnetic ordering temperature with the magnetic field applied perpendicular to the $c$ axis, i.e. perpendicular

to the helical axis. $M/H$ as a function of temperature at the indicated magnetic fields are depicted in Fig. 5.4(a). The kink due to the onset of helimagnetic ordering is not observed for H $\geq$ 1200 Oe. At 119 K, $M$ versus $H$ [see Fig. 5.4(b)] increases linearly at low field. At around 500 Oe, it shows a change in slope. Another slope change is observed around 1000 Oe. The region between 500 - 1000 Oe shows a steeper slope. With the decrease in temperature, the lower end of the steeper slope moves towards higher field and a sharp change is observed around 1000 Oe. The moments saturate above about 1300 Oe. This behavior is not observed at higher temperatures. A contour plot of $M$ versus $H$ and $T$ near the phase transition region is shown in Fig. 5.5. This provides a useful visualization of the magnetic phase diagram for $Cr_{1/3}NbS_2$. The magnetization values are highest in the red area (upper left) and lowest in the blue areas. The solid white line is a guide to the eye, and follows the temperature and field dependence of the ferromagnetic transition (white circles) determined from the measured saturation field at a fixed temperature [see, for example, the 110 K curve in Fig. 5.4(b)]. These points separate the soliton lattice (SL) phase from the ferromagnetic (FM) phase. The details of how the complex helimagnetic (HM) and SL phases evolve upon cooling from the paramagnetic (PM) phase have not been determined. Here, we observed the transition from the soliton phase to the ferromagnetic state at a field of about 1300 Oe for temperatures below about 117 K. A phenomenological description explains the evolution of the soliton lattice under an external magnetic field [5, 74, 75]. Over a certain range of the magnetic field applied perpendicular to the helical axis, the helimagnetic ground state gets distorted slowly into an inhomogeneous helicoid, however, the period does not change significantly. With further increase in the applied field there appears a sharp crossover when the 360-degree turns become discernible as solitonic kinks. But they are still bound and there is no real phase transition. It is a non-linear crossover behavior within the same modulated phase. The lower set of points (open circles) in the phase diagram (see Fig. 5.5) represent these states at different fields and temperatures. On further increasing the applied field, the core of the kinks remain almost stable in shape,

but their tails rapidly increase to resemble domains with magnetization in the field direction. This is the range of rapidly increasing magnetization between the lower and the upper set of points in the phase diagram. The magnetic phase transition from soliton lattice to the ferromagnetic state (or the free soliton state) is reached when the solitons become unbound. During this process, in reality, not all the solitons are pushed out of a finite crystal, rather they can be preserved as a gas of free solitons or remain somewhere pinned at defects in the crystal [143]. Therefore, depending on the maximum field value reached above this transition, cycling the field up and down through such a nucleation transition may eventually show a hysteresis, as remaining solitons may or may not enter back into the crystal and bind together to form a lattice again. This explains the observed hysteresis in the $M$ versus $H$ measurements as observed in Figure 5.3(a) which, otherwise usually represents a discontinuous phase transition. But, the heat capacity measurements (see Fig. 5.9) show a second-order phase transition in all range of magnetic fields measured. However, this SL-FM transition is apparent in the thermal and transport properties discussed below.

Figure 5.4(c) shows variation of $M^2(H,T)$ as a function of $H/M(H,T)$ at different temperatures in the region of the magnetic transition. These Arrott plots in the ferromagnetic state (at higher fields) are linear. The isothermal line in the Arrott plot passing through the origin represents the transition temperature. Thus, the Curie temperature ($T_C$) for $Cr_{1/3}NbS_2$ is taken to be 120 K.

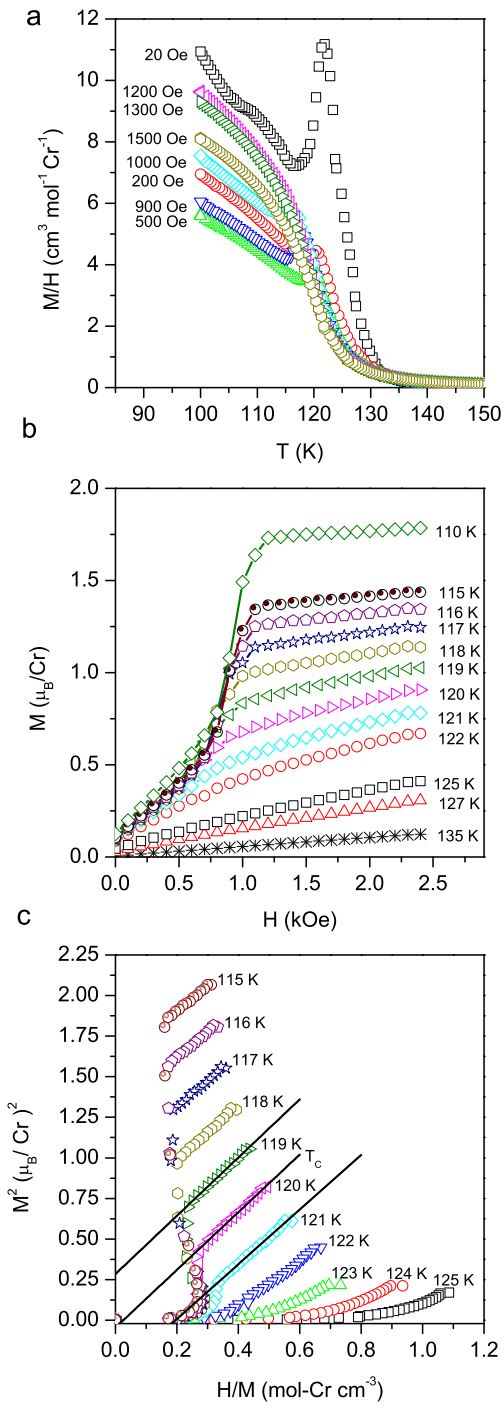


**Figure 5.4:** Magnetic properties of $Cr_{1/3}NbS_2$ near the transition temperature in low magnetic field applied perpendicular to the $c$ axis. a) $M/H$ as a function of temperature at indicated fields. b) $M$ vs. $H$ at selected temperatures, and c) Arrott plots. The solid lines are the extrapolation of the $M^2$ vs. $H/M$ data at higher fields.

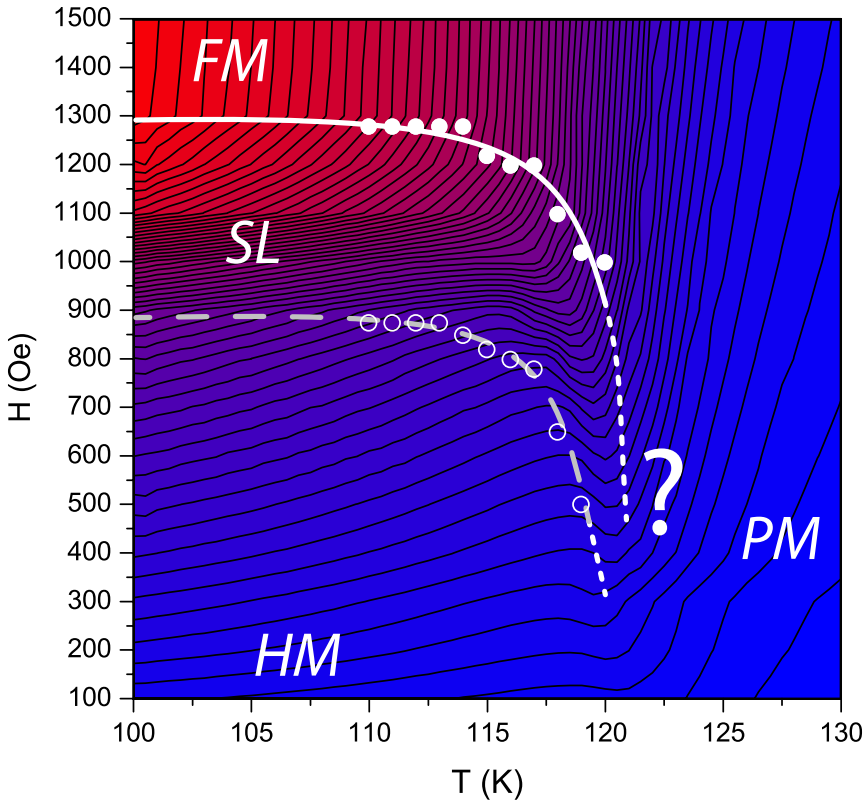


**Figure 5.5:** Contours of $M$ $(H,T)$ determined from $M$ vs $T$ measurements at fields from 100 to 1500 Oe applied in the $ab$ plane. The white data points were determined from $M$ versus $H$ measurements at temperatures from 110 to 120 K. The question mark "?" represents the region of transition form a paramagnetic (PM) to a helimagnetic (HM) phase. The details of this phase evolution have not yet been determined.

### 5.4.2 Transport properties

Electrical resistivity as a function of temperature is depicted in Figure 5.6(a). Interestingly, there is an abrupt and large change of the resistivity in the vicinity of the magnetic transition temperature. Above $T_C$, up to the measured temperature of 300 K, there is a slight decrease in the resistivity with temperature. It contrasts with the behavior of conventional metallic ferromagnets where there is a decrease in the resistivity on cooling over the entire temperature range and a change in slope or a kink near the magnetic transition temperature due to reduction in the

spin disorder scattering. Hall effect measurements at 200 K with the current in the *ab* plane and the magnetic field along the *c* axis gave a Hall coefficient of $2\times10^{-2}$ cm$^3$ C$^{-1}$ at 200 K (for a single band, this would correspond to $10^{20}$ holes cm$^{-3}$). This along with the measured resistivity values near 2 m$\Omega$ cm above the transition, suggests the material may be described as low carrier concentration metal or heavily doped semiconductor. The decrease in $\rho$ with increasing temperature at the highest temperatures investigated indicates that this is not a simple metal in the paramagnetic state. Similar high temperature behavior has been observed in some metallic, uranium-based, ternary compounds $UPt_2Si_2$ [144], $UPd_2Si_2$ [145], and $URh_2Si_2$ [146]. Comparison of the transport properties with those reported in Ref. 134 shows that the crystals studied here have higher resistivity and higher Hall coefficients than those previously studied.

Figure 5.6(b) shows the temperature dependence of the resistivity at various magnetic fields up to 140 kOe. As expected the effect of the magnetic field is strongest near the magnetic transition temperature. The sharp change observed at lower fields near $T_C$ are skewed to higher temperatures by magnetic field, as may be expected for a ferromagnet. However, a strong suppression of the resistivity upon cooling is still seen at 140 kOe. The inset of Figure 5.6(b) shows the magnetoresistance obtained by subtracting the resistivity measured at zero applied magnetic field from the resistivity measured at the magnetic field of 140 kOe. A very large magnetoresistance of about 55% is observed at the Curie temperature.

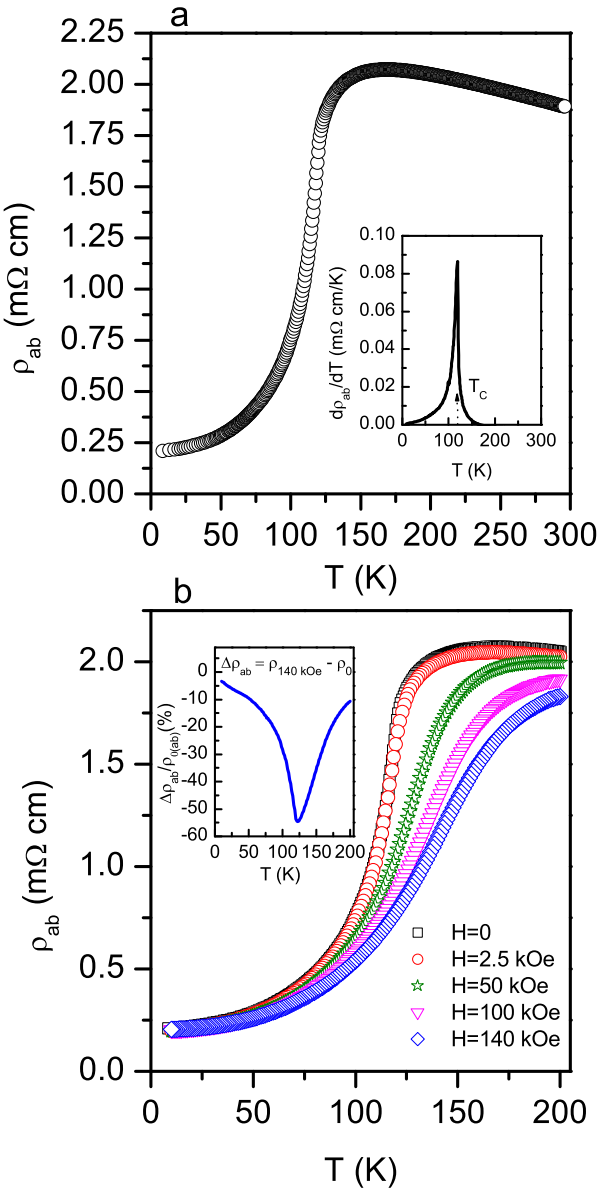


**Figure 5.6:** (a) Electrical resistivity of $Cr_{1/3}NbS_2$ as a function of temperature measured in the *ab* plane. Inset shows the temperature derivative of the resistivity. (b) Temperature dependence of electrical resistivity of $Cr_{1/3}NbS_2$ measured in the *ab* plane at indicated magnetic fields applied parallel to the plane. Inset shows the magnetoresistance where $\Delta\rho_{ab} = \rho_{140kOe}$-$\rho_0$.

Figure 5.7(a) shows the magnetoresistance measured at 2 K up to an applied magnetic field of 3 kOe. It shows a maximum magnetoresistance of about 5.5%. The change in magnetoresistance around 1 kOe is quite sharp and coincides with the SL phase indicated by magnetization measurements. At 2 K a small hysteresis is observed [upper inset in the Fig. 5.7(a)] and it appears in the same region where hysteresis is seen in the magnetization measurements [see Fig. 5.2(a)]. The hysteresis persists up to 100 K (not shown). The lower inset shows the derivative of the resistivity with respect to the applied magnetic field which clearly shows the sharp change occurring at the applied field of 1 kOe. This behavior in the resistivity also seems consistent with the soliton model. As discussed above, as the applied magnetic field starts aligning the moments towards its direction, spin disorder scattering decreases thereby reducing the electrical resistivity. As the magnetic field causes the transition from the soliton phase to the ferromagnetic state, all the moments are aligned in the direction of the field and thus no further change is seen in the resistivity at higher fields. The low-field magnetoresistance behavior is found to be qualitatively similar at all temperatures measured below 100 K. Figure 5.7(b) shows the normalized resistivity defined by $\rho_H/\rho_{H=0}$ as a function of magnetic field. Above 120 K, the resistivity varies little with field, while below 120 K, the resistivity behavior is similar to that observed at 2 K [cf. Fig. 5.7(a)]. Interestingly, at $T_C = 120$ K $\rho(H)$ has a strong field dependence but, unlike at lower temperatures, it does not saturate near 1 kOe. The origin of this behavior is unclear, and highlights the lack of detailed understanding of the complex behavior of helimagnetic materials near their critical temperatures.

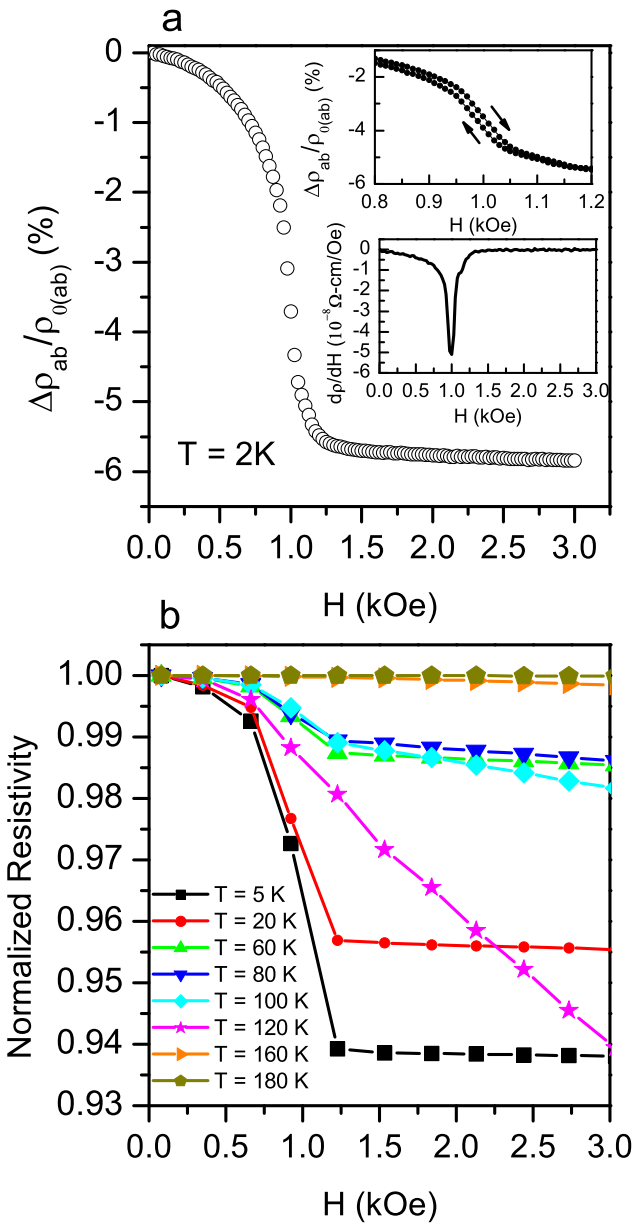


**Figure 5.7:** Low-field magnetoresistance of $Cr_{1/3}NbS_2$ measured in the *ab* plane with magnetic field applied parallel to the plane. (a) Magnetoresistance measured at $T = 2$ K. The upper inset shows the change in slope in the magnetoresistance in the vicinity of the field where the metamagnetic transition is observed in the magnetization measurements. The lower inset shows the derivative of the resistivity with respect of the field. It shows that the sharp change occurs at 1 kOe. (b) Normalized resistivity measured in the *ab* plane as a function of magnetic field applied parallel to the plane at indicated temperatures.

The temperature-dependent thermal conductivity $\kappa$(T) of $Cr_{1/3}NbS_2$ is shown in Fig. 5.8(a). Upon heating, $\kappa$ increases up to about 65 K above which it decreases slightly up to 200 K. In general, the thermal conductivity of a metal is the sum of electronic and lattice terms. The electronic contribution to the thermal conductivity can be estimated by the Wiedemann-Franz law: [147] $\kappa_e\rho/T = L$, where $\kappa_e$ is the electronic part of the thermal conductivity, $\rho$ is the electrical resistivity, and $L = 2.45\times10^{-8}$ W$\Omega$K$^{-2}$ is the Lorenz number. The maximum value of $\kappa_e$ estimated from Wiedemann-Franz law occurs around 65 K and is less than 5 *mW/cm-K*. This indicates that the thermal conductivity is mainly due to phonons.

Figure 5.8(b) shows the temperature dependence of the Seebeck coefficient ($S$). At all temperatures measured, the Seebeck coefficient is positive. However, it shows a remarkable minimum slightly below the magnetic transition temperature. The Hall coefficient of $Cr_{1/3}NbS_2$ [134] is reported to be positive above 180 K and below 20 K, and negative between these temperatures, with a sharp minimum at 115 K. This coincides with the region of minimum observed in S in Fig. 5.8(b). $Cr_{1/3}NbS_2$ is metallic with multiple bands contributing to the Fermi surface (see Sec. IV D). This complicates the interpretation of Hall and Seebeck coefficient data. In the simplest interpretation, the Hall data suggest electron dominated transport between 20 and 180 K, and primarily hole conduction at higher and lower temperatures. The Seebeck coefficient is positive over this entire temperature range, but the observed minimum is consistent with increased electron contribution peaking near 115 K. The data may indicate multiple bands near the Fermi energy with contributions to the transport properties which vary with temperature due to changes in band energies with temperature, or the probing of bands further from the Fermi energy at higher temperatures. In addition to changes in the electronic structure, changes in charge carrier scattering and mobilities may be associated with the magnetic ordering in $Cr_{1/3}NbS_2$. This could also contribute to the temperature dependence of the Hall and Seebeck coefficients near the transition temperature. Interestingly, the resistivity and Seebeck coefficients shown in Figures 5.6 and 5.8 show some similarity to the

reported behavior of LaFeAsO [148], $BaFe_2As_2$ [149] and related materials near their structural/magnetic phase transitions. The Seebeck coefficient is found to have a magnetic field dependence at 116 K. With the external magnetic field applied perpendicular to the $c$ axis, $S$ decreases up to about 20 kOe, above which it remains constant [see Fig. 5.8(b)], which suggests either a spin-entropy contribution to $S$, a strong influence of $H$ on the band structure, or the effects of the magnetic field on the scattering of carriers.

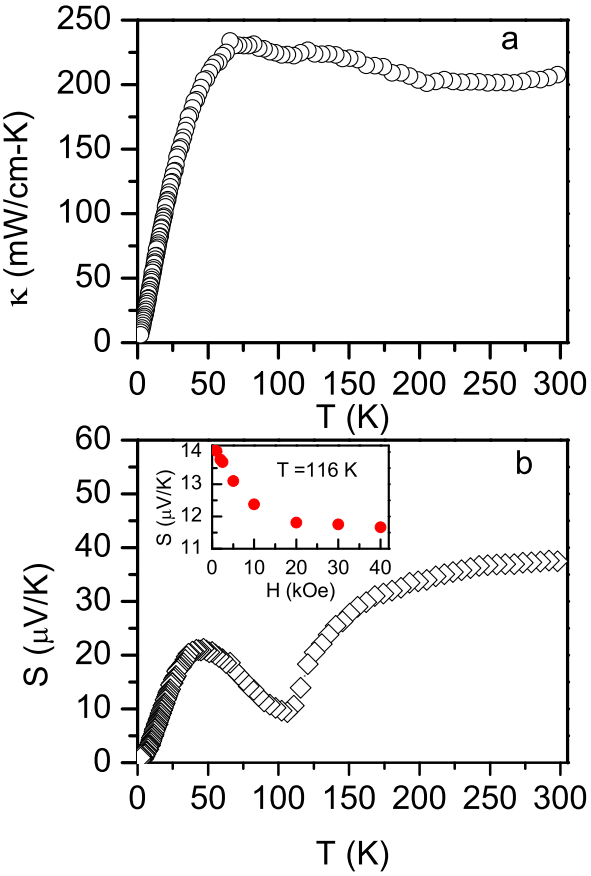


**Figure 5.8:** a) Temperature dependence of thermal conductivity measured in the *ab*-plane, and b) Temperature dependence of Seebeck coefficient measured in the *ab*-plane. Inset shows the magnetic field dependence of the Seebeck coefficient at T = 116 K with magnetic field applied parallel to the *ab*-plane

### 5.4.3 Heat capacity

The temperature dependence of specific heat shows clear lambda anomaly in the vicinity of the magnetic ordering temperature at ambient field as shown in Figure 5.9(a). The magnetic field dependence of the heat capacity anomaly is depicted in [Fig. 5.9(b)]. The lambda peak does not change significantly up to 800 Oe. However, it is found to decrease clearly at a field of 1500 Oe. The peak is suppressed with the further increase in the magnetic field and is not observed above 50 kOe. Application of a magnetic field increased the heat capacity above the magnetic transition temperature (120 K) and suppressed the heat capacity below it. A decrease in the lambda peak is found to occur in the ferromagnetic state when the moments are aligned in the direction of the magnetic field. This behavior is consistent with the results obtained in the magnetization and magnetoresistance measurements.

The low-temperature specific heat can be modeled well with electronic and phononic contributions. The inset of Fig. 5.9(a) shows a fit to $C/T = \gamma + \beta T^2$, where, $\gamma$ is the Sommerfeld coefficient and $\beta$ is the phononic heat capacity coefficient. The fit yielded $\gamma = 0.40 \pm 0.25\ mJ\ mol^{-1}\ K^{-2}$ and $\beta = 0.0263 \pm 0.0047\ mJ\ mol^{-1}\ K^{-4}$. The electron density of states at the Fermi energy ($E_F$) and the Debye temperature ($T_D$) can be estimated from $\gamma$ and $\beta$ using the relations $N(E_F) = 3\gamma/\pi^2 k_B^2$ and $T_D = (5\beta/12R\pi^4)^{-1/3}$, respectively, where $k_B$ is the Boltzmann constant and $R$ is the universal gas constant. The calculated values are $N(E_F) = 3.40$ states (eV-u.c.)$^{-1}$ and $T_D = 419$ K. The experimentally determined DOS at the Fermi energy is comparable to the value [2.76 states (eV-u.c.)$^{-1}$] obtained from the electronic structure calculations in the magnetic state presented below (Fig. 5.12).

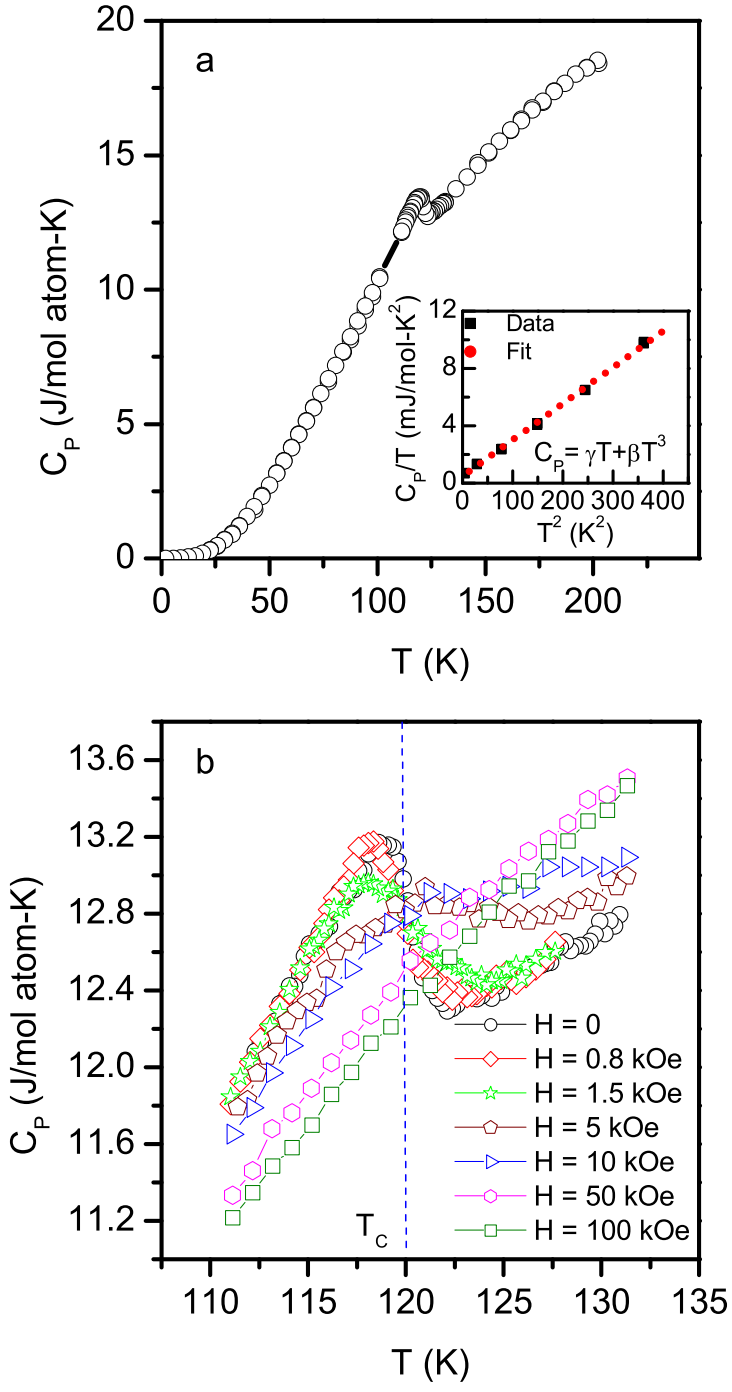


**Figure 5.9:** (a) Heat capacity of $Cr_{1/3}NbS_2$ as a function of temperature at zero applied magnetic field. (b) Temperature dependence of the specific heat near the magnetic transition temperature measured at indicated magnetic fields applied perpendicular to the $c$ axis.

### 5.4.4 First principles calculations

In order to understand theoretically the effect of the magnetic ordering we have performed first principles density functional theory calculations, using the generalized gradient approximation of Perdew, Burke and Ernzerhof [129] as implemented in the all electron code WIEN2k [128]. We have used the experimental hexagonal lattice constants and internal parameters; no relaxation was performed. Calculations in both a non-magnetic and a magnetic spin-polarized state were performed, using 120 $k$ points in the irreducible Brillouin zone and LAPW sphere radii of 2.07 $a_0$, 2.33 $a_0$ and 2.34 $a_0$ for the S, Nb and Cr atoms respectively (here $a_0$ is the Bohr radius = 0.529177 $\AA$). An $RK_{max}$ of 7, where R is the minimum atomic sphere radius and $K$ the largest plane-wave vector used in the expansion, was used.

Regarding the spin-polarized calculations, a brief discussion is in order. As reported previous experimental evidences [21, 133] that the ground state of $Cr_{1/3}NbS_2$ is a very long wavelength ($\sim 480\AA$) spiral with adjacent spins in the spiral very nearly parallel, such a magnetic structure, if one attempted to study it in a "brute-force" computational framework, would result in a calculation involving several hundred atoms and several thousand electrons, which would present a nearly intractable problem for standard first principles approaches. However, a simple observation allows one to perform a much simpler calculation which should be very close in energy and ground-state properties to the actual ground state. The origin of the DM interaction lies in the spin-orbit interaction [8, 9]. The energy scale of the relativistic term believed to be responsible for the spiral state is much weaker (a quantitative estimate suggests between one and two orders of magnitude smaller) than the ordinary ferromagnetic Heisenberg nearest-neighbor exchange energy. Thus it is highly likely that the actual energies and properties, such as the density of states of the real spiral magnetic ground state, can be described as very nearly those of an ordinary spin-polarized ferromagnetic ground state, with the "spin-up" and "spin-down" contributions simply summed. The DM interaction can be treated as a

small perturbation to the main ferromagnetic interaction, so that the actual energy eigenvalues of the physical electrons will not be significantly affected by it. It is then an excellent approximation to take a true ground-state physical observable, such as the density of states, as the *sum* of the separate "spin-up" and "spin-down" contributions. Again, a quantitative estimate suggests that the effect of the DM interaction on the Kohn-Sham eigenvalues is less than 10 meV, which is much smaller than all other relevant energy scales and virtually invisible on the plots presented below.

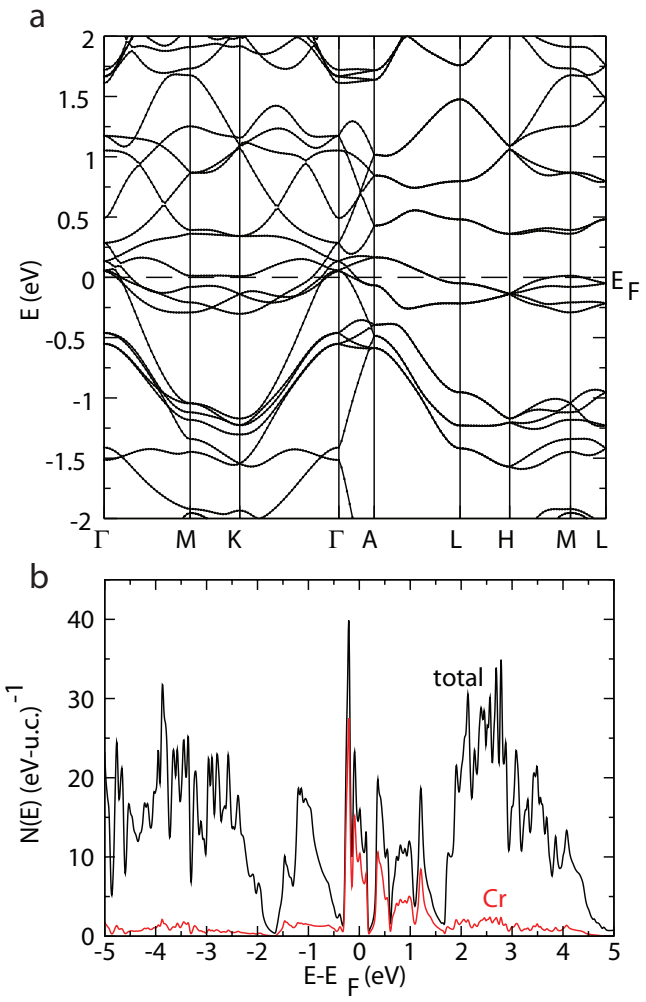


**Figure 5.10:** (a) The calculated band structure and (b) density of states of $Cr_{1/3}NbS_2$ in the nonmagnetic state. Note the many Fermi level crossings and corresponding high density of states at $E_F$.

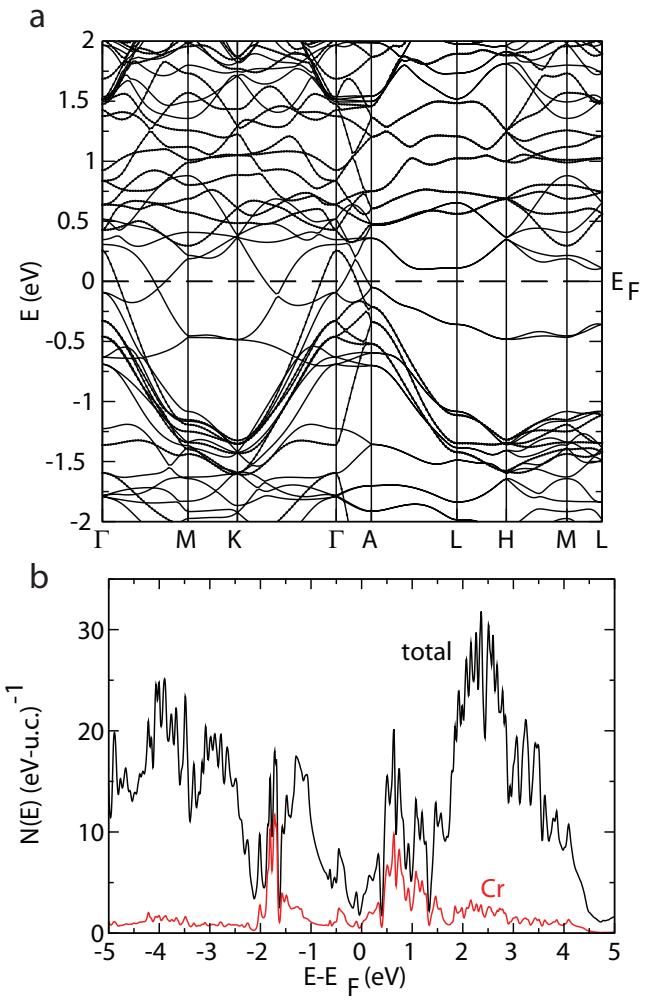


**Figure 5.11:** (a) The calculated band structure and (b) density of states of $Cr_{1/3}NbS_2$ in the assumed magnetic state. Most of the Fermi level crossings have disappeared and the density of states shows a substantial pseudogap at $E_F$.

We begin with the calculated nonmagnetic band structure and density of states, presented in Fig. 5.10 below. There are several bands crossing the Fermi level, and in addition flat bands virtually abutting the Fermi level from $M$ to $K$ and $H$ to $M$. There is also a fairly complex structure around the Γ point. As might be expected this band structure leads to a high density of states at the Fermi level, presented in Fig. 5.10(b). The Fermi level sits near the middle of a region of fairly elevated DOS, with Fermi level DOS of approximately 15 states/eV-unit cell and approximately

10 states/eV-unit cell chromium. Given the two Cr atoms in the unit cell and the exchange correlation value $I$ of 0.38 eV for Cr [130], one finds the Stoner criterion $N_0 I > 1$ well satisfied, with $N_0 I$ on a per Cr basis having the value 1.9. The majority, but not entirety, of the DOS character near $E_F$ is Cr, suggesting some hybridization of the chemical bonds.

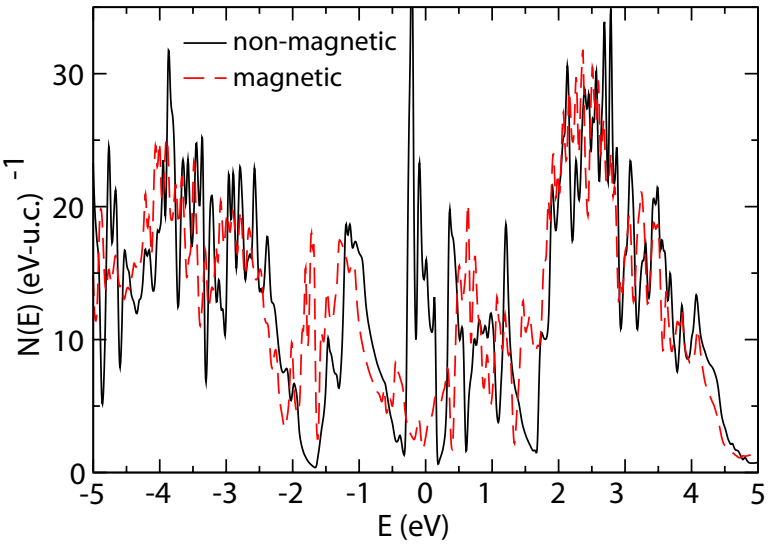


**Figure 5.12:** The calculated density of states of $Cr_{1/3}NbS_2$ in the magnetic and non-magnetic states.

Moving to the magnetic state calculations previously described, we find strong evidence for a magnetic ground state, with the magnetic state some 311 meV per formula unit in energy lower than the non magnetic state. In Fig. 5.11 we present the calculated band structure and density of states for this ground state; as outlined above we have simply summed the "spin-up" and "spin-down" contributions to the DOS and plotted both band structures on the same plot. The band structure demonstrates far fewer Fermi level crossings, and accordingly examining the density of states we find a substantial loss of spectral weight around $E_F$. It is instructive to directly compare the magnetic and non magnetic DOS, and this is presented in Fig. 5.12. We note that, the significant changes to the DOS are confined to an energy range of $\pm$ 2

eV around $E_F$, despite the large energy gain of nearly an electron-volt formula unit. The DOS at $E_F$ in the magnetic state is found to be 2.76 states (eV-u.c.)$^{-1}$ which is consistent with the experimental value extracted from the low temperature heat capacity presented above.

## 5.5 Summary and Conclusions

We have determined the temperature and magnetic field dependence of the magnetic, transport, and thermal properties of $Cr_{1/3}NbS_2$ single crystals. Contours of constant magnetization are utilized to identify key features in the magnetic phase diagram near the transition region (see Fig. 5.5). The material is magnetically ordered below about 120 K. Below this temperature, increasing the magnetic field applied in the *ab* plane results in a transition from helimagnetic to ferromagnetic order, with evidence from the previously reported soliton lattice phase at intermediate fields [21]. Evidence for these field- and temperature- induced phase transitions is also seen in resistivity, Seebeck coefficient, and heat capacity results. The resistivity responds strongly to the magnetic ordering, decreasing upon cooling through the magnetic transitions by more than a factor of four. A sharp drop in the Seebeck coefficient is observed upon cooling near 120 K as well. Significant effects of applied magnetic field on these transport properties are also seen in the ordered state, especially near the ordering temperature. Observations include large magnetoresistance (-55% at 140 kOe and 120 K) and $\rho(H)$ data that mimic the *M(H)* behavior below 120 K, but are anomalous at 120 K. These findings suggest that the magnetic transitions are accompanied by large changes in the electronic structure, which is confirmed by DFT calculations. The calculated DOS in the magnetic state is strongly suppressed relative to the value from non-magnetic calculations. Since the resistivity decreases upon entering the magnetically ordered state, changes in magnetic scattering of charge carriers are also likely to be important in determining the transport behavior. The large change in the resistivity suggests strong scattering by spin fluctuations above 120 K. Analysis of the

heat capacity results indicate a small Sommerfeld coefficient of 0.4 $mJmol^{-1}K^{-2}$, in agreement with the magnetic DFT calculations, and a Debye temperature of 419 K. A lambda-like anomaly in the heat capacity near the magnetic transition is suppressed strongly at fields above about 1.5 kOe, when the material is in the ferromagnetic state.

# Chapter 6

# Incommensurate-commensurate magnetic phase transition and soliton lattice in bulk crystals of $Cr_{1/3}NbS_2$

## 6.1 Introduction

In chapter 5 we presented the magnetic, thermal and transport properties of $Cr_{1/3}NbS_2$ along with the results from the first principles calculations. Here we present the magnetic measurements and the neutron scattering experiments results explaining the bulk magnetic measurement behaviors in terms of the microscopic spin structures observed in the neutron experiments. We have studied two sets of crystals with slightly different ordering temperature and have shown the evolution of soliton lattice in these crystals in an external magnetic field applied perpendicular to the pitch of the ground state helix with an ultimate incommensurate-to-commensurate phase transition.

As described in chapter 2 a soliton, in general, is a nonlinear traveling wave pulse that comes as a solution of a nonlinear partial differential equation and was first described by John Scott Russell [58]. Formation of a soliton in a magnetic magnetic material was described theoretically by Dzyaloshinskii, as a solution of the Landau thermodynamical potential in 1960s and has since been discussed by several authors [5, 74–76]. In fact, it is a nonlinear periodic structure of domain walls. The interesting part of this nano scale magnetic structure is that its periodicity is tunable by external parameters, especially, temperature or magnetic field, which makes it, especially in conductors, a potential candidate for spintronics application with interesting magneto transport behavior.

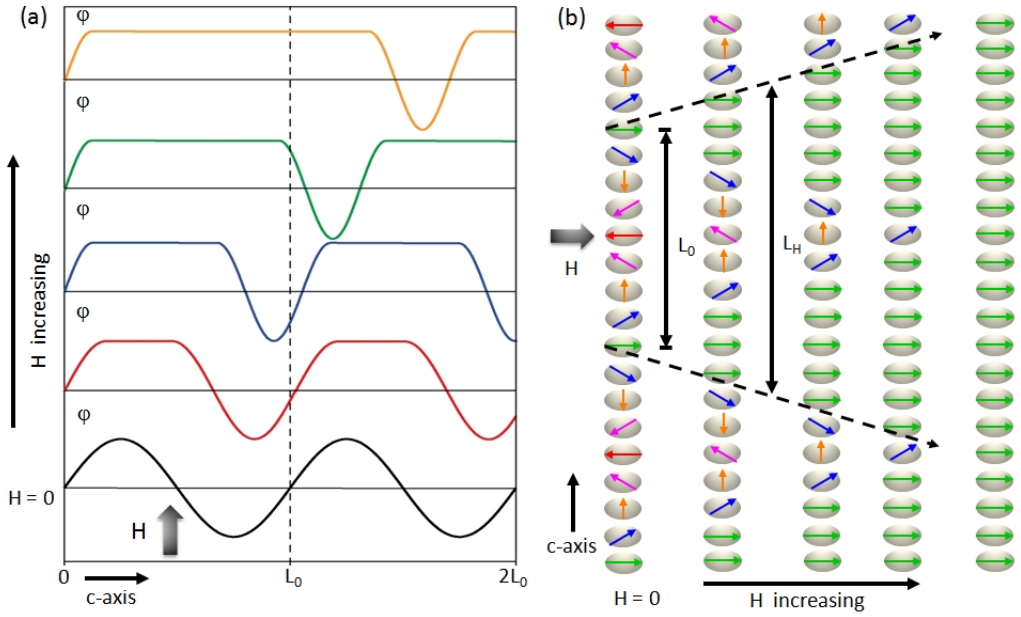


**Figure 6.1:** Cartoon showing the effect of magnetic field applied perpendicular to the helical axis. (a) Evolution of the magnetic soliton lattice from the helical ground state with the application of magnetic field as described in the text. (b) The period of the nonlinear spiral increases with an eventual transition to the ferromagnetic commensurate state.

Soliton lattice is expected to form in some magnets lacking the center of symmetry in the crystal lattice [74, 75]. The noncentrosymmetric crystal lattice allows an additional Dzyaloshinskii-Moriya (DM) term of the form $\boldsymbol{D}\cdot(\boldsymbol{S}_1\times\ \boldsymbol{S}_2)$ ($D$ is the DM vector, and $\boldsymbol{S}_1$ and $\boldsymbol{S}_2$ are nearest neighbor spins) in the Hamiltonian which tends to rotate the spins in the perpendicular orientation. It is given by the Lifshitz invariant in Landau thermodynamical potential and has a microscopic origin in the relativistic spin orbit coupling [8]. This antisymmetric DM interaction competes with the stronger symmetric exchange interaction $\boldsymbol{J}(\boldsymbol{S}_1\cdot\ \boldsymbol{S}_2)$, $J$ being the exchange coupling constant, usually resulting in a long period incommensurate helical state. The magnetocrystalline anisotropy dictates the direction of the helix. The length of period of the helix is given by $L_0 = 2\pi/\mathrm{q}_0$, where $q_0 \propto D/J$ is the magnitude of the wave vector of the helical structure in the momentum space. The external magnetic field tends to align the helically arranged spins along its direction, the angular evolution of which is described by the Sine-Gordon equation [74, 75]. In small magnetic field applied perpendicular to the wave vector of the helix the angular phase between the spins $\varphi = q_0\mathrm{z}$ does not change significantly. With further increase in the field, the phase is almost constant over a certain length but changes abruptly by $2\pi$. As the applied magnetic field ($H$) approaches the critical field ($H_C$), the relative fraction of the constant-pase section increases. Thus the system can be represented by a periodic structure of domains of commensurate phase separated by domain walls. Above $H_C$ the spins attain the commensurate state. The critical field thus marks the incommensurate-to-commensurate phase transition point. Cartoons of this phenomenon with the eventual transition into the ferromagnetic commensurate state is shown in Figure 6.1. As discussed in section 2.2, in the simple case of the helix along the $z$ direction and magnetic field applied perpendicular to the pitch of helix, the period of the intermediate non linear structure is given by $L_H = 8K(\chi)E(\chi)/(\pi q_0)$, where $K(\chi)$ and $E(\chi)$ are the elliptical functions of the first and the second kind, respectively, and $\chi$ is the elliptic modulus such that $0 \leq \chi \leq 1$ [5, 34, 74–76]. Thus

the increase in the length of the period of the nonlinear spiral as compared to the period of the ground state helix is given by a simple relation:

$$\frac{L_H}{L_0} = \frac{4K(\chi)E(\chi)}{\pi^2}, \tag{6.1}$$

with (see section 2.2)

$$\frac{E(\chi)}{\chi} = \sqrt{\frac{H_c}{H}}, \tag{6.2}$$

Equations 6.1 and 6.2 allow to plot *L(H)/L(0)* as a function of $H/H_c$. The quantity *L(H)/L(0)* can also be obtained experimentally.

$Cr_{1/3}NbS_2$ is an ideal system to realize this behavior of spins. Various transition temperatures have been reported for $Cr_{1/3}NbS_2$ ranging from about 116 K to about 170 K [21, 76, 133, 134, 140, 150]. One of the possible reasons for this may be slight variation in the amount of Cr atoms intercalated within the layers, which to some extent, depends on the synthesis environment. This material has a layered hexagonal structure in which the Cr atoms are intercalated in the octahedral holes (2c sites) between the trigonal prismatic layers of 2H-$NbS_2$ layers. The structure is described in chapter 5 in detail. It can be a separate topic of investigation. However, here the focus is in the study of the microscopic spin structure responsible for the observed behavior.

## 6.2 Experimental details

The two sets of samples studied are labeled as sample *A* and sample *B*. Transition temperature of sample *A* is 118 K and that of sample *B* is 131 K. In both sets of samples DC magnetic properties were measured using a Quantum Design Magnetic Property Measurement System (MPMS). Single crystal neutron diffraction was conducted in sample *A* using a four circle neutron diffractometer at beam line HB-3A at High Flux Isotope Reactor (HFIR) at Oak Ridge National Laboratory (ORNL). A neutron wavelength of 1.542 Å was used from a bent perfect Si-220

monochromator. The high resolution mode was used (mbend = 50) [151] to measure the satellite peaks at the distance of about 0.01 $Å^{-1}$ from the nuclear peak. Small angle neutron scattering was conducted on both samples at the beam line CG-2 also at HFIR at ORNL. A neutron wavelength of 4.75 Å was used. For the part of sample $A$, multiple crystals were stacked along the $c$ axis while in case of sample $B$ a single crystal of dimensions of about 5 × 4 × 0.11 mm was used. In both cases, a copper sample holder was used. A horizontal magnet was used such that the applied magnetic field was always parallel to the neutron beam. The detector was kept at a distance of 18.5 m from the sample. Rocking scans were carried out for the vertical axis between ±10°. Data analysis was done using Graphical Reduction and Analysis SANS Program (GRASP)[152].

Magnetic measurements of both the samples as a function of temperature and magnetic field is shown in Figure 6.2. In both cases, magnetic field was applied perpendicular to the $c$ axis. The *M(T)* data were collected while cooling in an applied magnetic field of 1 kOe. From Figure 6.2(a), the transition temperature, defined to be the temperature where the cusp appears, is seen to be 118 K for sample $A$ and 131 K for sample $B$. At high temperatures, both the samples follow a Curie-Weiss behavior. A difference has been found in the effective moment $\mu_{eff} = g\mu_B[s(s+1)]^{1/2}$ of the two samples. $\mu_{eff}$ per mole of Cr atom in sample $A$ is found to be 4.4 $\mu_B$ and that in sample $B$ is found to be 3.90 $\mu_B$. It suggests that sample $A$ has slightly more Cr atoms intercalated in the layer but essentially keeping the structure same and is consistent with the fact that the (00l) peaks of sample $A$, as compared to those of sample $B$ were shifted towards lower angle in x-ray patterns collected on the $ab$ plane.

The behavior of the magnetization as a function of field at a temperature of 2 K is shown in Figure 6.2(b). Both the samples show the similar behavior. The moments increase abruptly and remain constant after a certain field, termed as the critical field ($H_C$), with the further increase in the field. The critical field, however, is different in the two samples. $H_C$ for sample $A$ is about 1.3 kOe and that for sample $B$ is about

1.8 kOe. The critical fields represent the transition from an incommensurate spiral state to the commensurate ferromagnetic state.

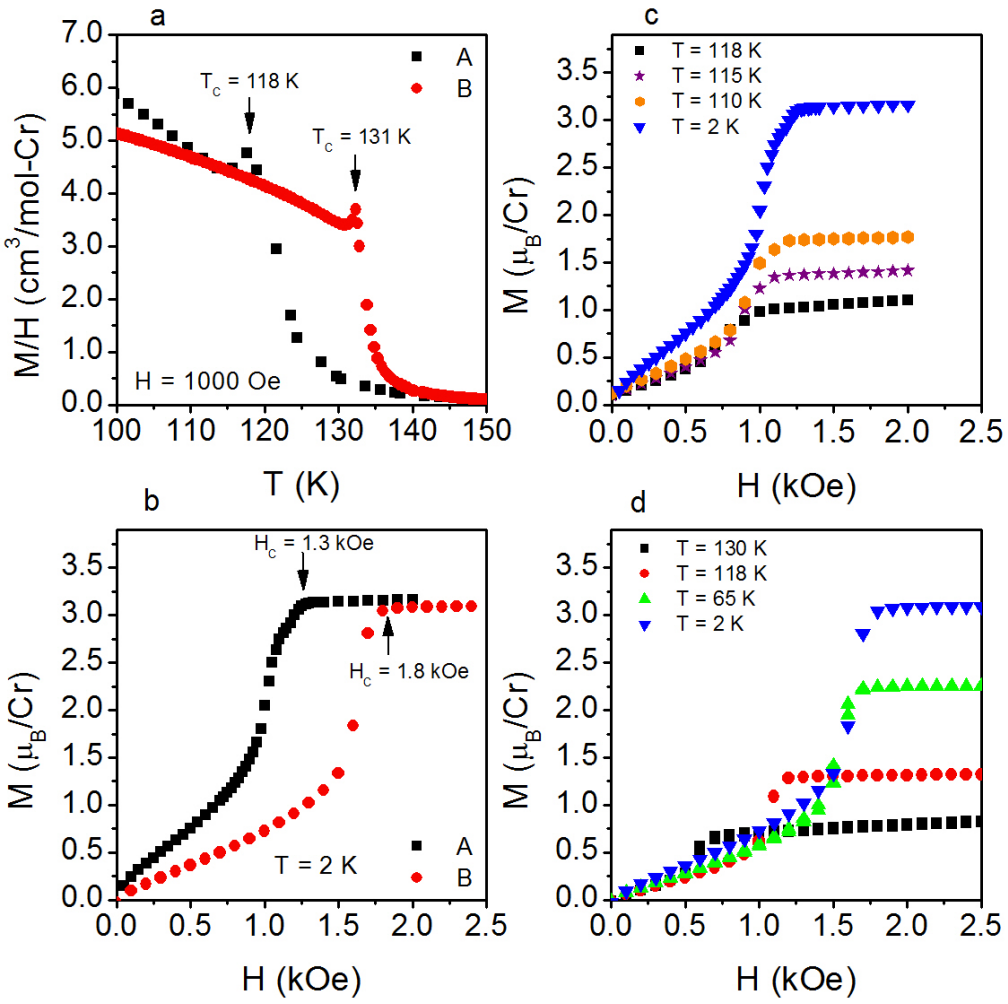


**Figure 6.2:** Magnetization measurements on the two samples of $Cr_{1/3}NbS_2$. (a) Temperature dependence of the $M/H$ of samples $A$ and $B$ showing different transition temperatures for the two samples, (b) Magnetic field dependence of magnetic moment of samples $A$ and $B$ showing different critical fields for the two samples, (c) Magnetic field dependence of the magnetic moment of sample $A$ at indicated temperatures, and (d) Magnetic field dependence of the magnetic moment of sample $B$ at indicated temperatures.

## 6.3 Single crystal neutron diffraction

In order to investigate the microscopic spin arrangement, we first conducted a single crystal neutron diffraction experiment on sample $A$. We found that that the intensity of the nuclear Bragg peaks (002) and (101) increased on cooling below the transition temperature. It is consistent with the easy plane type magnetization as reported and observed in the magnetization measurements [133]. Intensity of (101) nuclear Bragg peak is very weak in comparison to that of (002) nuclear peak. But, magnetic contributions in these peaks are same in case of a complete in-plane ferromagnetic state [133]. As the propagation vector of the helical state is known to be small, there is more likelihood of observing the satellite peaks due to the helical spin arrangement around the (101) nuclear Bragg peak. It is to be noted that, in a neutron diffraction experiment a helical spin structure gives a pair of satellite peaks on either side of the nuclear peak at a distance of q = $2\pi/L_H$ in the momentum space, where $L_H$ is the period of the helix. Thus, (101) Bragg peak was followed with the high resolution mode of the diffractometer. Figure 6.3(a) shows the onset of the satellite peaks on either side of (101) nuclear Bragg peak below the transition temperature. The satellite peaks are at a distance of 0.0102 $\text{Å}^{-1}$ from the nuclear peak suggesting a helical spin arrangement with period of 616 Å. A magnetic field of 0.9 kOe was applied perpendicular to the $c$ axis. In this case, as depicted in Figure 6.3(b) satellite peaks seem to disappear, however, the observed peak is still broader than that of the nuclear peak measured above $T_c$ and much more intense. It suggests that at 0.9 kOe, the period of the helix has increased and thus the satellite peaks have shifted towards the central nuclear peak falling within the resolution limit of the diffractometer.

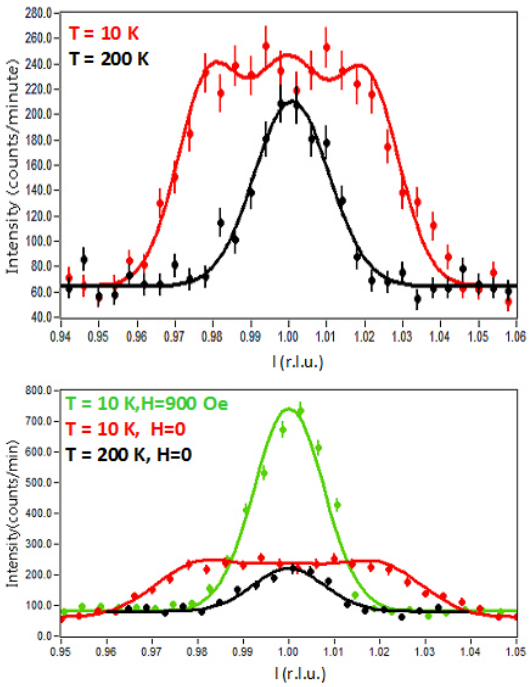


**Figure 6.3:** Elastic neutron scattering in $Cr_{1/3}NbS_2$ showing the l scan of (101) nuclear Bragg peak (a) above and below the transition temperature in zero applied magnetic field, (b) above and below the transition temperature in zero applied field and below the transition temperature in an external magnetic field of 0.9 kOe applied perpendicular to $c$ axis.

## 6.4 Small angle neutron scattering

In order to investigate a detailed effect of the magnetic field on the spin spiral, we conducted a small angle neutron scattering experiment on sample $A$. Again in a SANS experiment, helix with a period of $L_H$ gives magnetic satellite peaks at a distance of $q_0 = \pm\ 2\pi/L_H$ from the beam center. Figure 6.4 shows the results of the SANS experiment. In zero applied magnetic field [Fig. 6.4(a)] the satellite peaks are at $q_0 = \pm\ 0.0101$ Å$^{-1}$ suggesting the helix with a period of 622 Å, which is consistent with the result obtained from the diffraction experiment. It is found that with the increase in the magnetic field, the satellite peaks move closer towards the center [Fig. 6.4(b,c)]. At 1.3 kOe [Fig. 6.4(d)], the satellite peaks disappear. It suggests that the

period of the helix increases gradually with the increasing magnetic field. The helix is completely destabilized at 1.3 kOe with a transition into the ferromagnetic state. This critical field is consistent with that observed in the $M$ vs $H$ measurement. The period of the helix measured at 0.9 kOe is 825 Å.

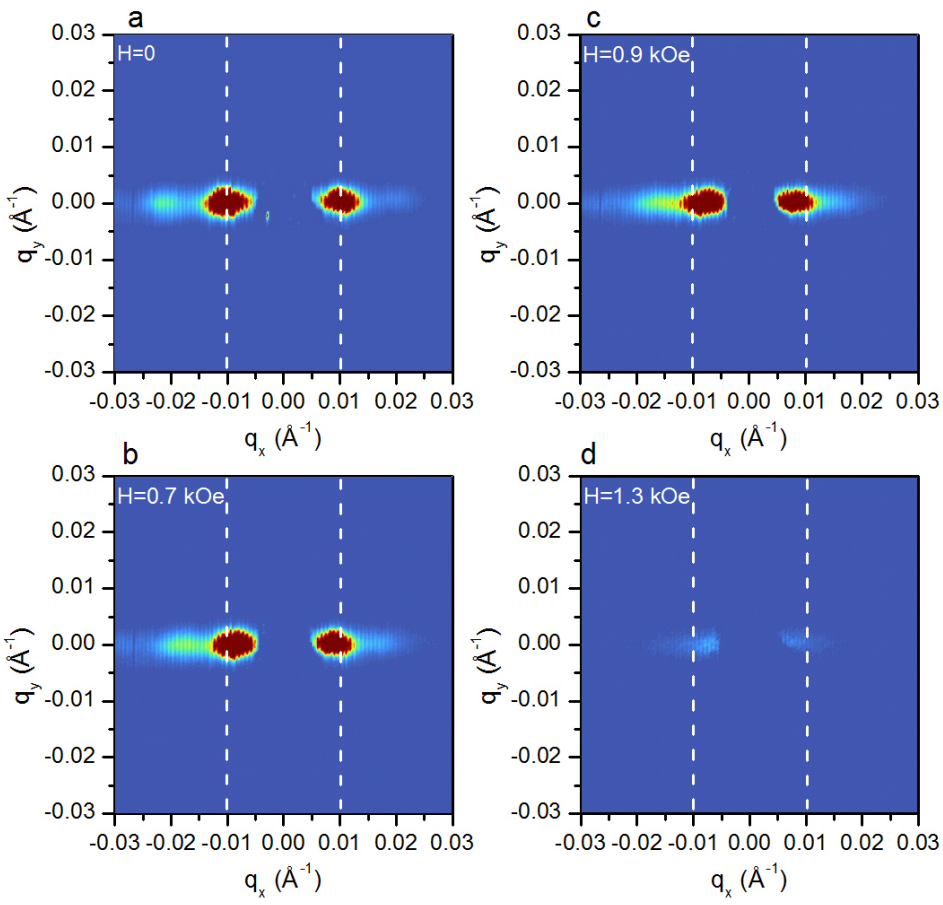


**Figure 6.4:** Small angle neutron scattering intensity of $Cr_{1/3}NbS_2$ (sample $A$) at a temperature of 2 K and with the magnetic fields applied perpendicular to the $c$ axis. (a) $H = 0$, (b) $H = 0.7$ kOe, (c) $H = 0.9$ kOe, (d) $H = 1.3$ kOe. The plots are obtained by subtracting the data collected at $T = 2$ K from the background data collected at $T = 150$ K. The white dashed lines are meant to guide the eye to observe the shift of the satellite peaks towards the beam center.

A more detailed study was conducted in sample $B$. First, SANS data were collected in zero magnetic field near the transition temperature. The data were also collected at various temperatures (2, 65, 118 and 130 K) in the applied magnetic field. Figure 6.4 shows the temperature dependent SANS scan in zero applied magnetic field. The satellite peaks are not observed at 132 K [Fig. 6.5(d)] but appear at 130 K [Fig. 6.5(c)] and become more prominent with the decreasing temperature [Fig. 6.5(b,a)]. Comparing this behavior with Figure 6.2(a), the cusp observed at 131 K in the $M/H$ vs $T$ curve represents the onset of the helimagnetic ordering. This kind of behavior in the temperature dependence of magnetization was shown theoretically by Kishine *et al.* [76] in case of chiral magnets. Such a cusp has also been observed in several other helimagnets - MnSi [111] FeGe [142], $Fe_{1-x}Co_xSi$ [19] and $Cu_2OSe_2O_3$ [91].

In the magnetic field dependent study at $T = 2$ K, magnetic field was increased at the step of every 0.2 kOe above 0.1 kOe. The satellite peaks were visible up to 1.7 kOe and disappeared at 1.9 kOe. As in the case of sample $A$, it was seen that the magnetic satellite peaks moved closer to the beam center with the increasing magnetic field before disappearing at 1.9 kOe, again indicating that the period of the helix gradually increased up to about 1.7 kOe above which an incommensurate to commensurate transition occurred. The plot of the relative increase in the period of the solitonic spiral relative to the period of the ground state helix $(L_H - L_0)/L_0$ as a function of $H/H_C$, where $H_C$ is the critical field marking the IC magnetic transition is depicted in Figure 6.6 (represented by solid squares). It also shows the theoretical plot of $(L_H - L_0)/L_0$ vs $H/H_C$ (represented by solid line) obtained using the relation between equations 6.1 and 6.2. Here we used $H_C$ =1.72 kOe in plotting the experimental data as the satellite peaks disappear between 1.7 and 1.9 kOe. The excellent agreement between the theoretical curve and the experimental data confirms that the soliton lattice evolves with the increase in the magnetic field with an ultimate transition to the ferromagnetic state at the critical field. In case of sample $B$, the period of the ground state helix is found to be 520 Å, smaller than that in the case of sample $A$.

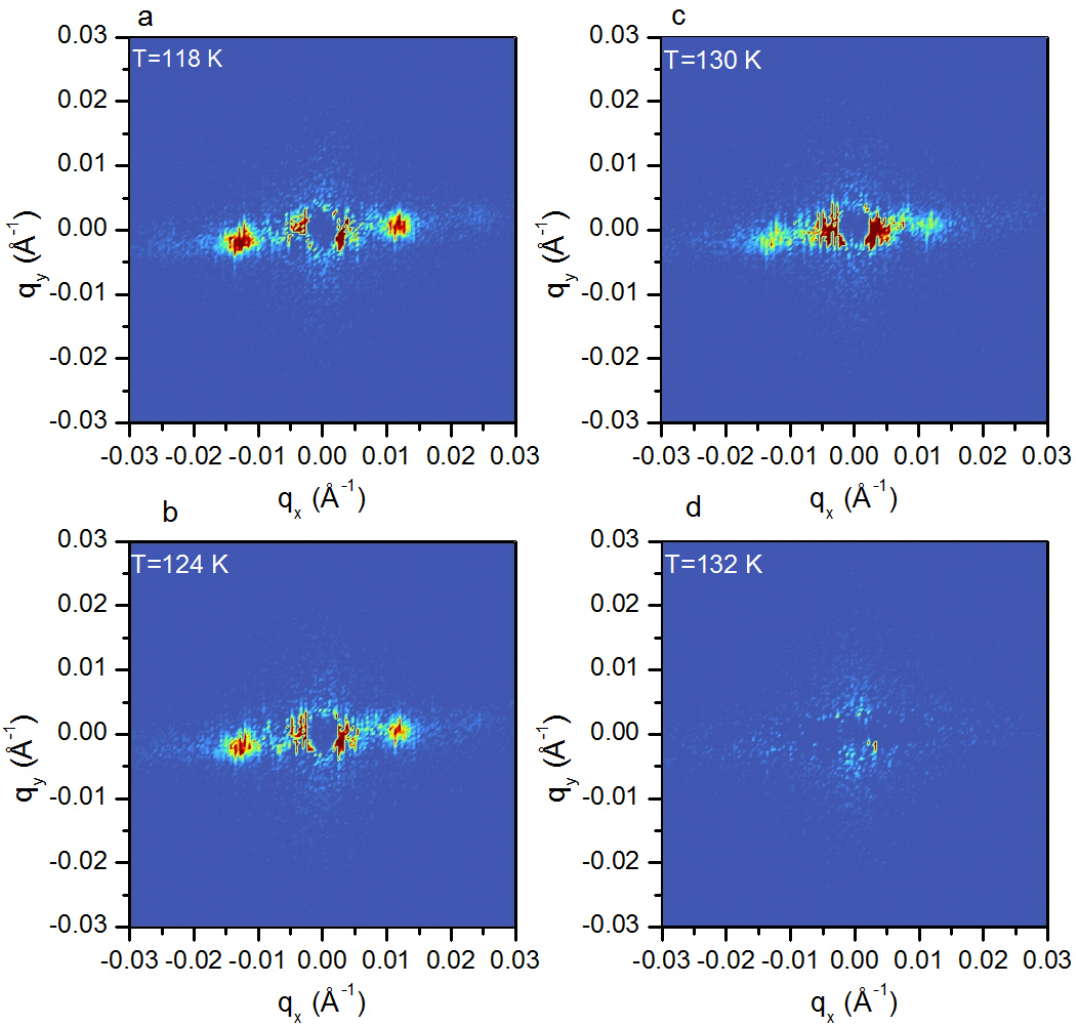


**Figure 6.5:** Small angle neutron scattering intensity of $Cr_{1/3}NbS_2$ (sample $B$) measured in a zero applied magnetic field at the indicated temperature. The plots are obtained by subtracting the data collected at the indicated temperature from the background data collected at $T = 150$ K.

We did not find significant variation in the periodicity of the ground state helix with temperature. However, the critical field has temperature dependence. In the SANS scans of sample $B$ measured at different magnetic fields, the satellite peaks were found to disappear at different magnetic fields at different temperatures. The observed critical fields are about 1.9, 1.8, 1.2 and 0.6 kOe at temperatures 2, 65, 118

and 130 K, respectively. The values of these critical field are consistent with those observed in the magnetic fields dependent magnetization measurements on the same sample shown in Figure 6.2(d).

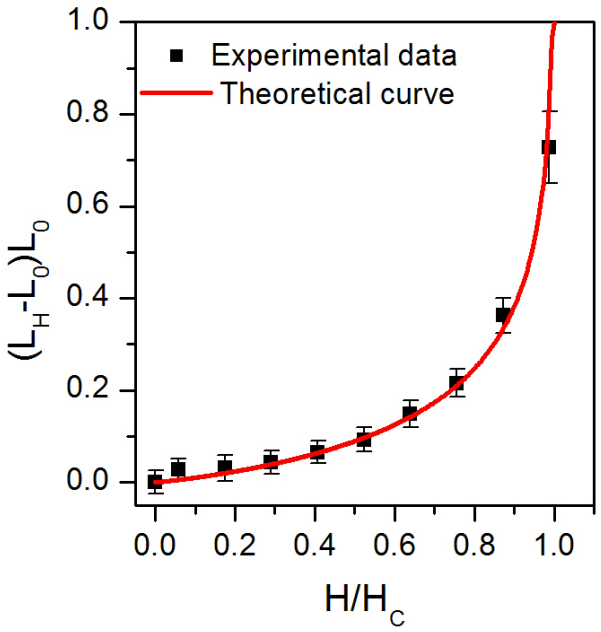


**Figure 6.6:** The relative increase in the periodicity of the solitonic spiral as compared to the period of the zero field helix $(L_H$ - $L_0)/L_0$ as a function of $H/H_c$. The solid line is the theoretical curve obtained from equations 6.1 and 6.2 showing an excellent qualitative agreement with the experimental data.

## 6.5 Summary

Here we basically found that the ground state helix is longer in sample $A$ than in sample $B$. It is also found that the critical field required to attain a complete commensurate state is smaller in sample $A$ than in sample $B$ and that $T_C$ of sample $A$ is smaller than that of sample $B$. This observation suggests that the DM interaction is relatively weaker in sample $A$ than in case of sample $B$ as the period of the helix is inversely proportional to the DM constant ($q_0 \propto D/J$ ). It is consistent with the

fact that the $c$ axis of sample $A$ is slightly larger than that of sample $B$ as mentioned above. It also explains the difference observed in $T_C$ of the two samples. For a weaker DM interaction, a lower temperature is required to set the helical state. As the external magnetic field, through the Zeeman term, weakens the DM term or the spin orbit coupling, smaller field can destabilize the longer helix as compared to the shorter one. Another important observation is that the critical field decreases with the increasing temperature, although the period of the helix remains almost the same. It suggests that spin fluctuation plays important role in such a structure at higher temperatures and near $T_C$. As the fluctuation becomes more pronounced less field is required to attain the commensurate phase. The increasing level of noise with the increase in the temperature in the SANS scans near the transition temperature as observed in Figure 6.5 may be an indicative of the underlying spin fluctuation.

# Chapter 7

# Magnetic and thermal properties of 2D antiferromagnet $K_2V_3O_8$

## 7.1 Introduction

As discussed in chapter 2 we know that Dzyaloshinskii-Moriya (DM) interaction in a certain class of noncentrosymmetric magnets can lead to the so called "mixed state of a ferromagnet" both in the easy axis-ferromagnets and antiferromagnets [92–94]. In 1994 a prediction was made that such a state, which later was termed as skyrmion, can be obtained in some particular noncentrosymmetric magnets including the cubic B20 helimagnets MnSi, FeGe $Fe_xCo_{1-x}Si$ and $Co_xMn_{1-x}Si$ with an additional requirement of a uniaxial anisotropy [95]. Later in 2002, skyrmion was found in MnSi [16] and subsequently in other cubic DM helimagnets [20, 86–88, 90], but without an obvious requirement of the uniaxial anisotropy. Thus, a puzzle still exists why the skyrmion is observed so far only in the space group $P2_13$. Observation of skyrmion in other systems is, therefore, important to help understand the mystery.

Easy axis ferromagnets and antiferromagnets are thus the target set of materials for such modulated complex spin structures because of the obvious uniaxial anisotropy. In 1997 a soliton lattice was observed in an easy axis antiferromagnet

$Ba_2CuGe_2O_7$ in a neutron scattering experiment [33]. With the external magnetic field applied parallel to the $c$ axis, before the spin flop transition, the propagation vector was found to change direction in accordance with the soliton model put forward in 1960s [74]. More recent experiments have shown an unexpected antiferromagnet cone phase in this material [153, 154]. Likewise, a magnetic soliton lattice has also been observed in another easy axis antiferromagnet $CuB_2O_4$ [32]. But, skyrmion has not yet been observed in any of these materials, so far. $K_2V_3O_8$ is another anticipated material in this respect. It is one of the materials predicted to have the rare coexistence of weak ferromagnetism and spin spiral texture, and skyrmion lattice [11].

$K_2V_3O_8$ is an easy axis antiferromagnet with a noncentrosymmetric tetragonal crystal structure. Magnetization measurements and neutron scattering experiments have shown antiferromagnetic behavior below 4 K with the moments pointing in the $c$ direction and a weak ferromagnetic behavior in the $ab$ plane [155]. The same study reports that application of the external magnetic field along the $c$ axis induces a conventional spin flop transition at about 8.5 kOe while along $ab$ plane there occurs an unusual spin reorientation. The spins continuously move from $c$ axis to the $ab$ plane remaining normal to the direction of the applied field. However, the possibility of long period helical structure has not been explored yet.

In this chapter we present the results of a detail magnetic and thermal property measurements. It is observed that when the magnetic field is applied along the $c$ axis, the spins rather move continuously with increasing magnetic field forming a possible chiral spiral in the $ab$ plane before the spins flop into the $ab$ plane. At the same time, a nearly ferromagnetic chiral helix may exist along the $c$ axis which gets destabilized continuously due to the spin reorientation from $c$ axis into the $ab$ plane when the magnetic field is applied along the $ab$ plane. No obvious sign of skyrmion is observed, which usually shows up as a softening in the real part of the ac susceptibility measurement as a function of the applied magnetic field [20, 118, 156].

## 7.2 Crystal and magnetic structure

$K_2V_3O_8$ crystallizes in a tetragonal space group P4bm and has a fresnoite-type structure with lattice constants $a$ = 8.870 Å and $c$ = 5.215 Å [157]. The room temperature structure consists of vanadium oxide planes separated by the $K^+$ layer as depicted in Figure 7.1(a). The vanadium oxide layer consists of vanadium atoms belonging to two different inequivalent crystallographic sites labeled as V1 and V2 in the figure. The V1 atoms occupying 2a site are in the 4+ oxidation state and bear magnetic moment while the V2 atoms in 4c site are in 5+ oxidation state and hence are non-magnetic. The magnetic V1 atoms form S = 1/2 $V^{4+}$ -$O_5$ square pyramid and V2 atoms form $V^{5+}$ -$O_4$ tetrahedra. A slight structural modulation occurs at around 115 K with an unusual behavior observed in $a$ axis [158]. The $a$ axis first expands on cooling and abruptly begins to contract below 115 K. This structural phase transition has also been marked in the thermal conductivity measurements [159]. Optical properties measurements have shown anomalies in the local structure of $VO_5$ square pyramids below about 110 K [160].

Lumsden *et al.* [155] in the magnetization measurements, observed an easy axis type antiferromagnet behavior in this material below 4 K with a broad maximum visible centered at about 10 K attributed to the two dimensional nature of the crystal structure as described above. Their neutron diffraction experiment found a two sublattice antiferromagnet structure with the moments pointing along the $c$ axis. The corner and the face-centered moments within the basal plane in a magnetic unit cell are aligned antiparallel. In Figure 7.1(b) the black arrows show the reported magnetic structure in absence of an external magnetic field. The same study found that when magnetic field is applied along the $c$ axis, the moments flop from the $c$ axis into the $ab$ plane at 8.5 kOe, the spin-flop field ($H_{SF}$). On the other hand, external magnetic field applied in the $ab$ plane shows an unusual spin reorientation behavior. The moments continuously move from $c$ axis into the $ab$ plane with increasing magnetic field always remaining normal to the direction of the applied

field. The spin reorientation completes at the spin-reorientation field ($H_{SR}$) of 6.5 kOe. The green arrows in Figure 7.1(b) show this final spin arrangement with field applied in the *ab* plane. These behaviors of spin flop and spin reorientation have been explained on the basis of spin exchange model incorporating Heisenberg and DM interactions and *c* axis anisotropy [155].

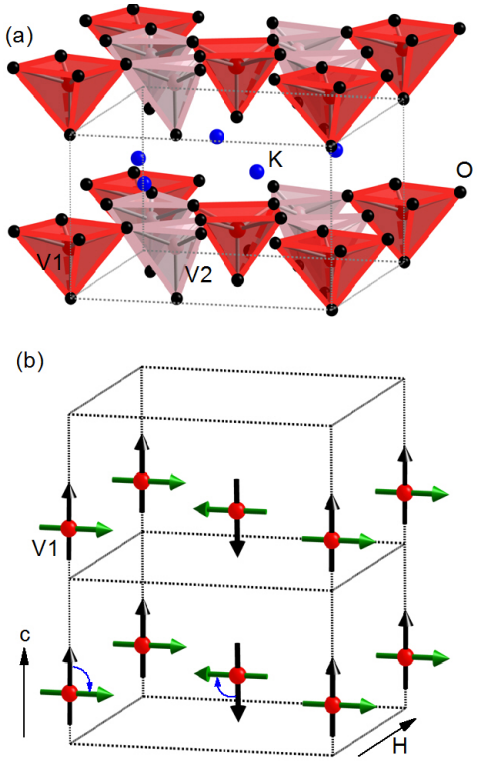


**Figure 7.1:** (a) Crystal structure of $K_2V_3O_8$ showing the layers of vanadium oxide separated by a layer of potassium. The vanadium oxide layer consists of magnetic $V^{4+}$-$O_5$ pyramids and non-magnetic $V^{5+}$-$O_4$ tetrahedra. (b) Reported magnetic structure of $K_2V_3O_8$. The black arrows represent the spin orientation in the absence of external magnetic field. With the application of the magnetic field in the *ab* plane, moments reorient continuously from *c* axis to the *ab* plane. The spin reorientation completes at a field of about 6.5 kOe called the spin reorientation field ($H_{SR}$). When magnetic field is applied along the *c* axis (not shown) the spins flop from *c* axis to the *ab* plane at the field of about 8.5 kOe called the spin flop field ($H_{SF}$).

## 7.3 Experimental details

Single crystals of $K_2V_3O_8$ were grown by using $KVO_3$ flux as described in Ref. 161. Plate like crystals of various sizes were obtained with an average dimension of about $5\times5\times1$ mm$^3$. DC magnetic properties were measured using a Quantum Design Vibrating Sample Magnetometer SQUID using field cool approach. $M$ vs $H$ was measured while both increasing and decreasing the the magnetic field. We did not see any significant hysteresis in the measurements both parallel and perpendicular to the $c$ axis. AC susceptibility and heat capacity were measured using a Quantum Design Physical Property Measurement System (PPMS). AC susceptibility measurement was conducted with AC field of 10 Oe and at frequencies of 100, 1000 and 10000 Hz. The data in the entire range of measurement was frequency independent. Every time, the measurement was done while cooling from above the transition temperature.

## 7.4 Results and Discussion

### 7.4.1 DC Magnetization

Figure 7.2(a) shows the temperature dependence of $M/H$ as a function of the magnetic field applied along both parallel and perpendicular to the $c$ axis at an applied field of 0.1 kOe. Long range magnetic ordering is clearly visible below 4 K. Above this temperature, the magnetic moment increases with increasing temperature. It is due to the short range order transition at a higher temperature. There is a broad hump centered at around 10 k (not shown). Above about 5.5 K $M/H$ shows the same behavior in the measurements both parallel and perpendicular to the $c$ axis. But this behavior is quite different at lower temperatures in the two directions. When magnetic field is applied along the $c$ axis, the transition is marked by a kink and the magnetic moment decreases on further cooling - a normal behavior usually shown by the antiferromagnetic ordering. The behavior with field applied perpendicular to the $c$ axis is remarkable. The moment abruptly increases below about 5 K deviating from

the behavior observed along the $c$ axis, makes a cusp at 4 K with a slight decrease followed by a small increase with the further decrease in the temperature. It is to be noted that in case of a simple antiferromagnet, there is deviation in the $M/H$ behavior in the two directions. However, in the case of field perpendicular to the easy axis the moments remains almost constant below the transition temperature. The increase of magnetic moments here indicates a weak in-plane ferromagnetic behavior. This kind of temperature dependence of magnetic moments as observed, here, in the $ab$ plane has been a characteristic behavior of the known DM helimagnets - MnSi, FeGe, $Fe_{1-x}Co_xSi$, $Cu_2OSe_2O_3$, and $Cr_{1/3}NbS_2$ [19, 91, 111, 142]. In chapter 6 we verified the onset of helical ordering right below the temperature of the cusp by means of magnetic properties measurements and small angle neutron scattering experiment in case of $Cr_{1/3}NbS_2$ when magnetic field is applied perpendicular to the direction of the helix.

Magnetic field dependence of the magnetic moments at 2 K is depicted in Figure 7.2(b). When the external magnetic field is applied along the $c$ axis, the moment first increases linearly followed by a more rapid change in the moment that completes at 8.5 kOe, above which the moment again increases linearly. 8.5 kOe is the spin flop transition field at which the moments pointing along the $c$ axis are reported to flop into the $ab$ plane [155]. However, when the magnetic field is applied perpendicular to the $c$ axis, the moments increase linearly with increasing magnetic field up to 6.5 kOe, above which it shows a change is slope. Again, in neutron scattering experiments a spin reorientation from $c$ axis into the $ab$ plane was found to be completed at this field. These behaviors were previously reported by Lumsden *et al.* [155]. Below we will show that these behaviors are consistent with the presence of long period helical ordering. AC susceptibility and heat capacity measurements presented in subsections 7.4.2 and 7.4.3 provide further support.

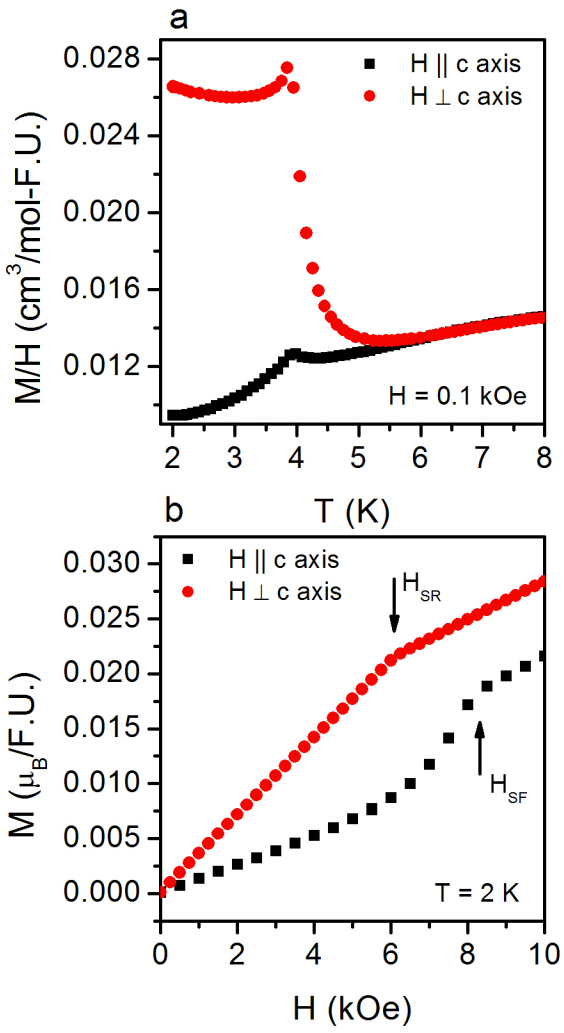


**Figure 7.2:** (a) $M/H$ as a function of temperature measured in the indicated external magnetic field applied parallel and perpendicular to the $c$ axis. (b) $M$ vs. $H$ measured at a temperature of 2 K with the magnetic field applied parallel and perpendicular to the $c$ axis.

Magnetic susceptibility defined as $M/H$ as a function of temperature is presented in Figure 7.3. In case of the field applied parallel to the $c$ axis [Fig.7.3(a)] on increasing the magnetic field up to 5 kOe, the behavior observed in the absence of external field [see Fig.7.2(a)] does not change much. At 8.5 kOe the behavior changes. Below 4 K, the moment increases all the way down to 2 K. Likewise, when the magnetic field is applied perpendicular to the $c$ axis, the cusp at the transition temperature observed

in the absence of external field is gradually diminished and pushed towards the lower temperature with the increase in the magnetic field. At 8.5 kOe, which is above $H_{SR}$, no such cusp is observed at all.

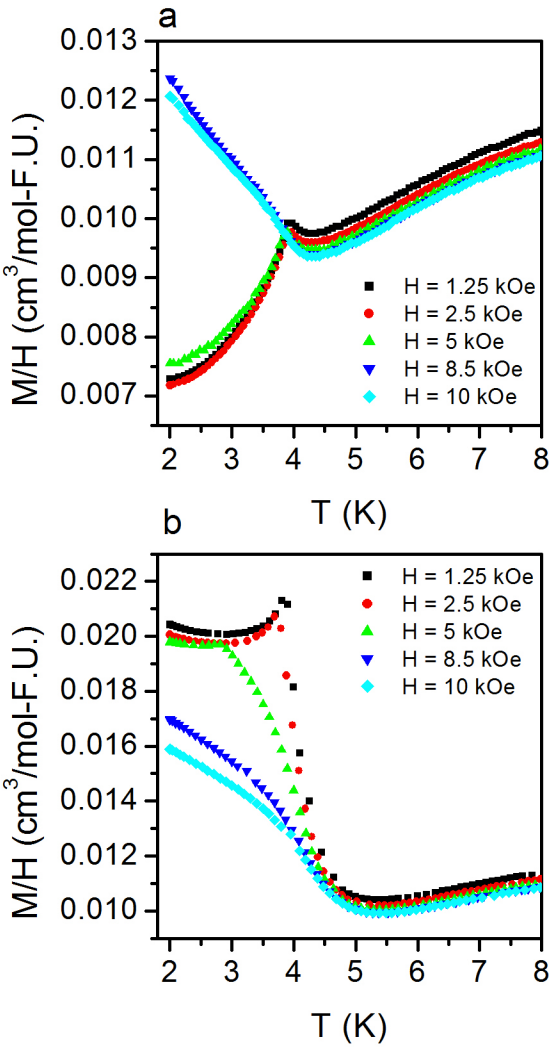


**Figure 7.3:** $M/H$ as a function of temperature measured in the indicated external magnetic field applied (a) parallel and (b) perpendicular to the $c$ axis.

### 7.4.2 AC susceptibility

The behavior observed in the AC susceptibility measurements is quite remarkable. Figure 7.4 shows the temperature dependence of the real part of the AC susceptibility ($\chi'$). In the case of the measurement along the $c$ axis [Fig.7.4(a)] we found that up to the applied magnetic field of 8.5 kOe there is a gradual change in the behavior of $\chi'$ in the ordered state. At lower fields up to 5 kOe, $\chi'$ decreases below the transition temperature. On further increasing the magnetic field, $\chi'$ slowly starts increasing with the decrease in temperature. The change becomes maximum at 8.5 kOe, and at and above 10 kOe no significant change is observed. AC susceptibility is sensitive to very small changes in the magnetic moment. Therefore, this observation is important. In the DC magnetization measurement [see Fig.7.3(a)] the moments increase even at 10 kOe. Comparison of the DC magnetization and AC susceptibility behaviors at 10 kOe suggests that the increase of moment in this field is linear in DC measurement so that the rate of change as picked up by $\chi'$ is almost zero. This change is non-linear at lower fields. It is a clear indication of the fact that there exists some sort of weak magnetic ordering at the lower fields that gets destabilize at 8.5 kOe with a sudden flop of spins into the $ab$ plane. We can interpret this result by making a comparison to the magnetic structure of a well studied uniaxial antiferromagnet $Ba_2CuGe_2O_7$, also having a noncentrosymmetric tetragonal crystal lattice [33, 162]. Although $K_2V_3O_8$ and $Ba_2CuGe_2O_7$ crystallize in different space groups and have different point group symmetries, both of these uniaxial antiferromagnets support the formation of the helical structures theoretically from the symmetry point of view with only a slight difference in the form of helix [11]. In case of $Ba_2CuGe_2O_7$ the spins are in the (1 -1 0) plane forming a spin spiral with propagation vector along (1+$\xi$, $\xi$, 0) with $\xi = 0.027$. Magnetic field applied along the $c$ axis gradually changes the direction of the propagation vector forming a soliton lattice before inducing an incommensurate-commensurate phase transition marked by a spin flop at a field of 2.3 kOe [33, 162]. The AC susceptibility behavior of $K_2V_3O_8$ measured along $c$ axis

indicates a similar spiral structure. It is supported by the similarity observed in the heat capacity behavior of $K_2V_3O_8$ and $Ba_2CuGe_2O_7$ measured in the external magnetic fields applied along the $c$ axis discussed in section 7.4.3 below.

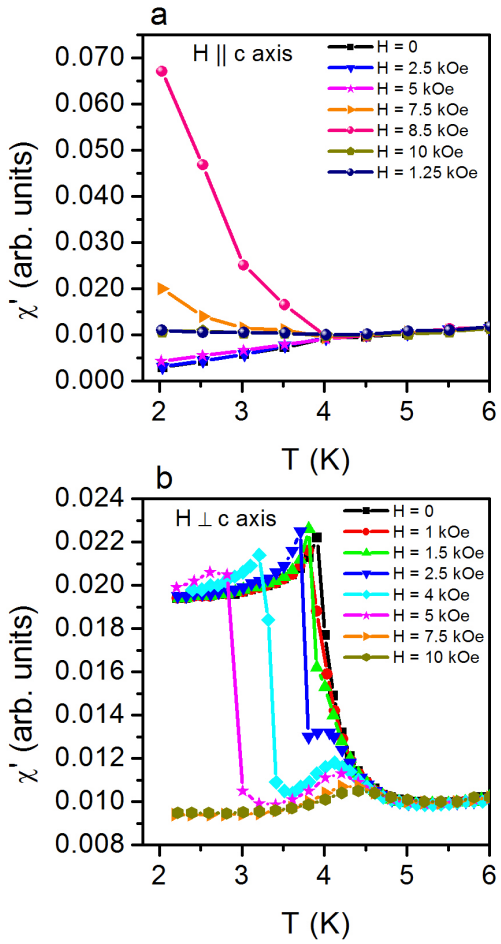


**Figure 7.4:** Real part of AC susceptibility as a function of temperature measured with the indicated external magnetic field applied (a) parallel and (b) perpendicular to the $c$ axis.

Real part of the AC susceptibility as a function of magnetic field applied parallel to the $c$ axis is depicted in Figure 7.5(a). Below the long range ordering temperature of 4 K, $\chi'$ remains almost constant at lower fields and starts increasing on approaching the spin flop field ($H_{SF}$), becomes maximum at ($H_{SF}$) then drops abruptly. The spin flop

field increases with increasing temperature towards the transition temperature. At 4 K there is no change in $\chi'$. Phase diagram of another easy axis antiferromagnet $MnF_2$ shows a similar behavior. No modulated or spiral spin structure has been reported in $MnF_2$. It is to be noted that $MnF_2$ has a centrosymmetric crystal structure. But an intermediate phase has been found between the antiferromagnetic and the spin flop phases [163].

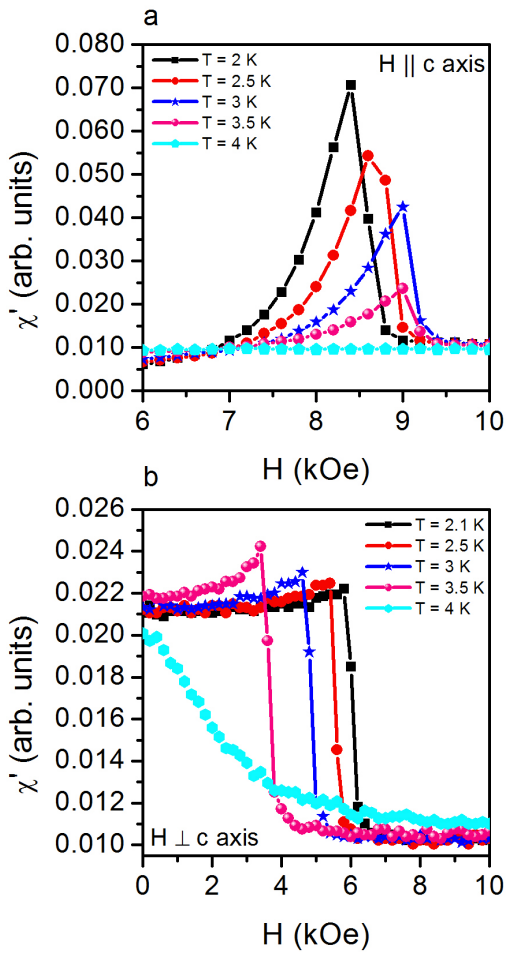


**Figure 7.5:** Real part of AC susceptibility as a function of external DC magnetic field applied (a) parallel and (b) perpendicular to the $c$ axis at the indicated temperatures.

The AC susceptibility shows a completely different behavior in the $ab$ plane. Figure 7.4(b) shows the temperature dependence of the real part of AC susceptibility

measured in the *ab* plane. In the absence of external magnetic field, $\chi'$ is similar to the DC magnetization [see Fig. 7.2(a)]. With the increase in the magnetic field, the sharp increase and cusp at the transition temperature is pushed towards lower temperatures. Meanwhile, from the field of about 1.5 kOe a relatively broad peak emerges neat 4 K. This peak moves to higher temperatures with increasing applied field, and a local minimum exists between it and the sharp cusp. The broad peak is found to get pronounced on approaching the spin reorientation field. Above $H_{SR}$, i.e. at 7.5 kOe, the sharp increase and cusp is found to get completely suppressed. The broad peak still keeps shifting towards higher temperature but with reduction in the peak height. This is a typical behavior of $\chi'$ observed in the known DM helimagnets. In case of MnSi [14], there is a helical ordering up to a field of 6 kOe. Up to the external field of about 1 kOe, the helix is fixed along <111> direction. Between 1 kOe and 6 kOe the helix unpins and starts to align parallel to the direction of the magnetic field. Above 6 kOe there is a field induced commensurate ferromagnetic state. The first peak in $\chi'$ is present up to 6 kOe and disappears at 7 kOe. Likewise, in FeGe [118] the first peak is found to be completely suppressed at a field of 1.5 kOe which completely destabilize the helical state into the polarized ferromagnetic state. In the case of FeGe also, the helix gets unpinned and start aligning in the direction of the the external magnetic field. Such a state is called conical state. A similar, but not exact, behavior of $\chi'$ has been observed in $Cr_{1/3}NbS_2$ in the *ab* plane [164]. The first peak is completely suppressed as soon as the spiral state is destabilize into the commensurate ferromagnetic state. On this basis, it can be interpreted that there exists a nearly ferromagnetic helical ordering with the pitch of the helix in a direction perpendicular to the *ab* plane that gets destabilized above $H_{SR}$. This kind of nearly ferromagnetic spiral has been recently predicted in $Ba_2CuGe_2O_7$ due to the effect of the z-component of the DM interaction to the spins in the almost cycloidal structure lying closest to the *ab* plane. In case of $K_2V_3O_8$, such a nearly ferromagnetic helical behavior observed in the *ab* plane provides support for the canted antiferromagnetic

arrangement in the other direction ($c$ axis). Such a spiral state should be easily detectable in a small angle neutron scattering experiment.

Figure 7.5(b) shows $\chi'$ as a function of magnetic field applied in the $ab$ plane. At lower temperatures, $\chi'$ changes very little with increasing magnetic field and abruptly drops at the critical field $H_{SR}$. Near 2 K $H_{SR}$ is found to be 6.5 kOe. It decreases with increasing temperature as expected. On approaching transition temperature a slight increase in $\chi'$ is observed near $H_{SR}$. This feature is not seen at and above 4 K. In these measurements, both parallel and perpendicular to $c$ axis, we did not see any region with a softened $\chi'$, which would have been the indication of a skyrmion lattice.

### 7.4.3 Heat capacity

Heat capacity as a function of temperature below 20 K is depicted in Figure 7.6. A broad hump corresponding to the magnetic short range ordering due to the 2D nature of the system is observed between 12 and 6 K. At 4 K, a lambda anamoly is observed marking the onset of the magnetic ordering.

When the magnetic field is applied parallel to the $c$ axis the lambda peak remains almost unchanged up to about 2.5 kOe [Fig.7.7(a)]. With the further increase in the field, the lambda peak gets diminished and shifts towards lower temperatures. The lambda peak is clearly observed up to 8.5 kOe. However, at 10 kOe, the transition is marked just by a kink. On further increasing the magnetic field the kink starts to move towards the higher temperatures. It becomes larger and wider and continuously shifts towards the higher temperatures becoming almost equal to the zero field lambda peak at the field of 20 kOe [Fig. 7.7(a)]. This peak is found to grow further with further increase in the magnetic field [Fig. 7.7(b)]. A similar behavior of the heat capacity has been observed in $Ba_2CuGe_2O_7$ with the magnetic field applied along the $c$ axis [154]. Note that $Ba_2CuGe_2O_7$ has a helical ground state with the pitch of helix perpendicular to the $c$ axis which gets distorted with the application of the magnetic

field along the $c$ axis forming a soliton lattice and an eventual spin flop at a field of about 2.4 kOe.

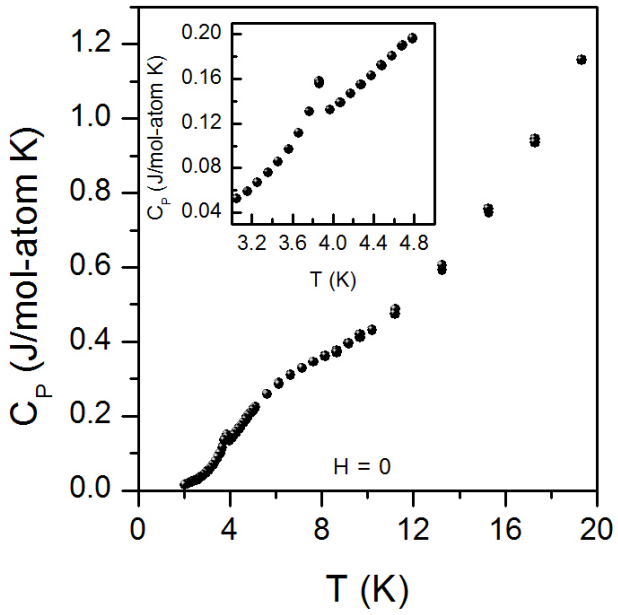


**Figure 7.6:** Temperature dependence of heat capacity in zero applied magnetic field. Inset shows the magnified plot of the lambda anamoly peak observed at the magnetic transition temperature.

Figure 7.8 shows the heat capacity measured with magnetic field applied perpendicular to the $c$ axis. In this case, the lambda peak is similarly suppressed as in the case of the field applied parallel to the $c$ axis but with much lower field. The lambda peak disappears even at 3.5 kOe, a field smaller than the spin reorientation field of 6.5 kOe [Fig. 7.8(a)]. With the further increase in the magnetic field the broad peak, as observed in the other orientation, appears and moves towards the higher temperature [Fig 7.8(b)]. Although the behavior of this latter peak is similar in the two orientations, they do not overlap at the corresponding fields.

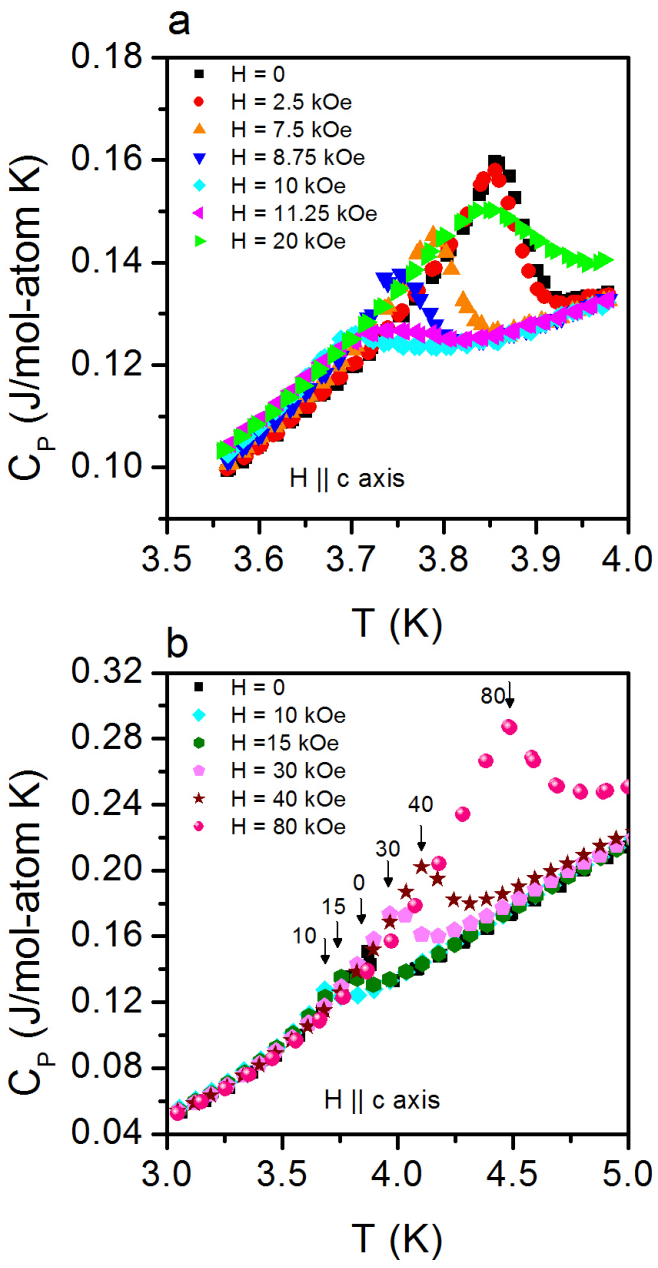


**Figure 7.7:** Heat capacity as a function of temperature measured at indicated magnetic fields applied parallel to the $c$ axis. The arrows in Figure (b) indicate the lambda anomaly peak. The numbers next to the arrow indicate the magnetic field in kOe.

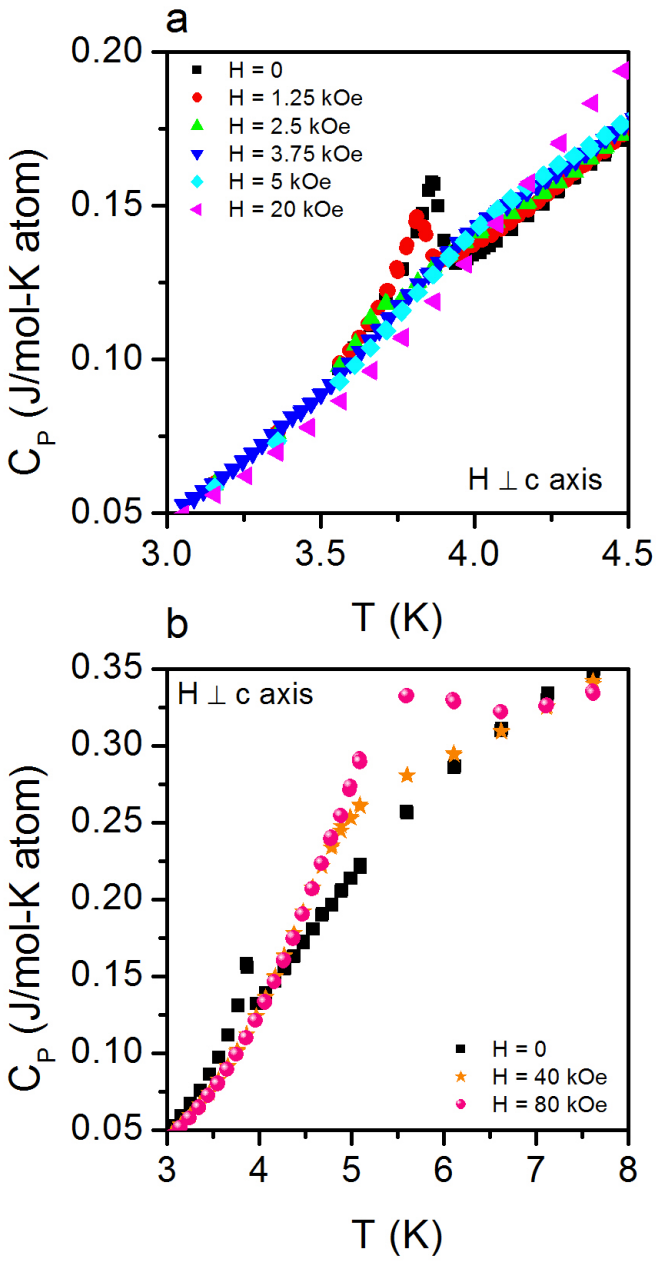


**Figure 7.8:** Heat capacity as a function of temperature measured at indicated magnetic fields applied perpendicular to the $c$ axis.

### 7.4.4 Summary

The observation in DC magnetization, AC susceptibility and heat capacity of the noncentrosymmetric tetragonal easy axis antiferromagnet $K_2V_3O_8$ is remarkable. The

spin flop and the spin reorientation transition perviously verified in the neutron scattering scattering experiment are clearly visible in all the measurements conducted. In addition, with the external magnetic field applied parallel to the $c$ axis, above 2.5 kOe and and up to $H_{SF}$ a continuously changing spin behavior is observed in the AC susceptibility and heat capacity measurements. Based on the symmetry arguments, a theoretical calculation shows that $K_2V_3O_8$ supports the formation of a cycloid [11]. The same paper makes a similar prediction in case of another noncentrosymmetric tetragonal easy axis antiferromagnet $Ba_2CuGe_2O_7$. An antiferromagnetic cycloidal structure has been experimentally observed in this material in absence of external field. With the field applied perpendicular to the pitch of the helix, the spiral gets gradually distorted into a soliton lattice and finally shows an IC transition above about 2.4 kOe. Heat capacity behavior of $K_2V_3O_8$ also shows a remarkable similarity with that of the $Ba_2CuGe_2O_7$ in case of magnetic field applied parallel to the $c$ axis. These observations thus suggest that a long period incommensurate spin structure with propagation vector perpendicular to the $c$ axis exists in $K_2V_3O_8$. The applied magnetic field along $c$ axis distorts this spiral continuously up to $H_{SF}$ where the spin flop occurs marking the IC phase transition.

Meanwhile, the DC magnetization measurements in the $ab$ plane suggest a nearly ferromagnetic helical behavior of spins below the transition temperature. The in-plane AC susceptibility measurements suggest that above about 1.5 kOe the spins rotate continuously, most likely as in the case of MnSi the conical state is formed where the helix gets unpinned and starts rotating along the direction of the magnetic field. The helix in zero applied field is along the $c$ axis. The rotation of this helix in the direction of the applied field may be responsible for the observed unusual spin reorientation from the $c$ axis into the $ab$ plane [155]. A recent prediction of a nearly ferromagnetic spiral state along the $c$ axis in $Ba_2CuGe_2O_7$ [154] supports a similar structure in $K_2V_3O_8$.

To sum up, the behavior of $K_2V_3O_8$ observed in DC magnetization, AC susceptibility and heat capacity measurements together with the theoretical support and

the observed magnetic structures in a similar uniaxial antiferromagnet $Ba_2CuGe_2O_7$ suggest that in addition to the weak ferromagnetism, $K_2V_3O_8$ can have two different types of helical structures parallel and perpendicular to the $c$ axis. Most likely, the spiral perpendicular to the $c$ axis forms a soliton lattice below $H_{SF}$ where as, the helix along the $c$ axis rotates gradually towards the direction of the external magnetic field below $H_{SR}$. Neutron scattering experiments are needed to verify the proposed modulated structures and can be studied with a high resolution diffractometer and small angle neutron scattering.

# Chapter 8

# Concluding remarks

Noncentrosymmetric magnets are a special class of materials. It is because the broken inversion center allows an additional relativistic term of the form $\boldsymbol{D}\cdot(\boldsymbol{S}_1\times\boldsymbol{S}_2)$ called the Dzyaloshinskii-Moriya (DM) interaction in the Hamiltonian and uniquely possess three different energy scales - the exchange interaction that favors parallel spin arrangement, the DM interaction that tends to rotate the spins in a perpendicular configuration and the magnetocrystalline anisotropy. Depending on the strength of the interactions, competition among these energy scales results in a chiral helical structure. The DM term ensures the chirality and hence makes the modulated spin structures in these class of materials different from those in the crystals having a center of symmetry. The DM term can be expressed in the form of invariants involving the first derivatives of the magnetization known as Lifshitz invariants. These Lifshitz invariants are considered to be responsible for stabilizing the complex magnetic structures like solitons and skyrmions. These modulated magnetic structures are believed to have potential for technological application in nanomagnetism and spintronics. Presence of the chiral helices in these materials has even made these materials a possible ground for the search of the magnetic blue phases, reminiscent of the blue phases observed in liquid crystals. Here, we extended the search and study

of these exotic magnetic structures using various techniques in $Cr_{11}Ge_{19}$, $Cr_{1/3}NbS_2$ and $K_2V_3O_8$.

$Cr_{11}Ge_{19}$ has a tetragonal crystal structure and belongs to the space group $P\bar{4}n2$. Polycrystalline sample of this material was investigated by means of DC and AC susceptibility, transport and thermal properties measurements, x-ray diffraction, resonant ultrasound spectroscopy and first principles calculations. Nonlinear conventional Arrott plot, unusual AC susceptibility and weak heat capacity anomaly near the Curie temperature indicated complex magnetic behavior. Strong magneto-elastic coupling was observed in the temperature dependence of the elastic moduli and lattice constants with a negative thermal expansion at lower temperatures. Strong evidence for the itinerant ferromagnetism and a possible noncollinear ground state was also obtained in the first principles calculations.

Soon after the observation of the soliton lattice in the hexagonal chiral helimagnet $Cr_{1/3}NbS_2$ by means of a Lorentz force transmission electron microscope [21], we did a detail investigation on the single crystals of this material. The signature of spin reorientation from the helical ground state to the commensurate ferromagnetic state was clearly observed in the magnetic, thermal, and low field magnetoresistive behaviors. A large magnetoresistance was observed at higher fields (55 % in 140 kOe) near the magnetic ordering temperature. By means of the measured field and temperature dependence of magnetization, we constructed the phase diagram in the vicinity of the magnetic transition. From neutron scattering experiments we were able to observe the evolution of the soliton lattice and the incommensurate to commensurate transition in accordance with the theoretical model.

Finally, we investigated an easy axis antiferromagnet $K_2V_3O_8$ having a tetragonal crystal structure by means of DC magnetization, AC susceptibility and heat capacity measurements. In the out-of-plane measurements we found a subtle magnetic ordering in the external magnetic field between the antiferromagnetic ground state and spin flop phase. Likewise, in-plane measurements indicate a possible helical ground state that rotates continuously along the direction of the applied magnetic field before

destabilizing above the spin reorientation field previously observed in the neutron scattering experiments. These predictions are made based on the comparison of the results with the well studied chiral helimagnets and the existing theoretical support.

The complex behavior observed in the magnetic properties of $Cr_{11}Ge_{19}$ deserves further study in the single crystal form. Although the diffraction experiments can be difficult because of the complicated structure, the possible modulated structures may be studied using small angle neutron scattering. Being a conductor $Cr_{1/3}NbS_2$ provides an ideal environment to study the behavior of soliton lattice. The magnetic soliton can act as a magnetic superlattice potential to the itinerant electrons and can show interesting magnetotransport properties [35, 36, 165]. Meanwhile, itinerant electrons can cause spin transfer torque on the soliton causing the translation of those solitons. Such subtle effects may be observed in topological Hall effect measurements [30] and also in small angle neutron scattering experiments [31]. Doping studies of $Cr_{1/3}NbS_2$ by Fe can open another interesting avenue. $Fe_{1/3}NbS_2$ is an easy axis antiferromagnet [150]. It would be interesting to see the the effect of a small amount Fe at the Cr site in $Cr_{1/3}NbS_2$ essentially preserving the crystal structure. Certainly, the complex behavior observed in the $K_2V_3O_8$ can be studied by means of neutron scattering experiments. The previous neutron experiments conducted were not focused to look for these kinds of (spiral) spin structures.

# Bibliography

[1] M. N. Baibich, J. M. Broto, A. Fert, F. Vguyen Van Dau, F. Petroff, P. Eitenne, G. Creuzet, A. Friederich, and J. Chazelas, Phys.Rev. Lett. **61**, 2472 (1988). 1

[2] G. Binasch, P. Grunberg, F. Saurenbach, and W. Zinn, Phys. Rev. B. **39**, 4828 (1989). 1

[3] H. D. Flack, Helvetica Chimica Acta **86**, 905 (2003). 2

[4] N. A. Spaldin, *Magnetic Materials Fundamentals and Applications* (Cambridge University Press, New York, 2003). xii, 4

[5] Y. A. Izyumov, Sov. Phys. Usp. **27**, 845 (1984). xii, 5, 7, 21, 72, 91, 92

[6] S. Blundell, *Magnetism in Condensed Matter* (Oxford University Press, New York, 2001). 6

[7] T. Moriya, Phys. Rev. Lett. **4**, 228 (1960). 6

[8] T. Moriya, Phys. Rev. **120**, 91 (1960). 6, 7, 84, 92

[9] I. Dzaloshinsky, J. Phys. Chem. Solids **4**, 241 (1958). 7, 84

[10] P. Bak and M. H. Jensen, J. Phys. C: Solid St. Phys. **13**, L881 (1980). 8, 17, 18

[11] A. N. Bogdanov, U. K. Rößler, M. Wolf, and K.-H. Müller, Phys. Rev. B **66**, 214410 (2002). 28, 31, 104, 111, 119

[12] U. K. Rößler, A. N. Bogdanov, and C. Pfleiderer, Nature **442**, 797 (2006. 13

[13] U. K. Rößler, A. A. Leonov, and A. N. Bogdanov, J. Phys: Conf. Ser. **303**, 012105 (2011). 8

[14] C. Pfleiderer, A. Neubauer, and S. Mühlbauer, J. Phys.: Condens. Matter **21**, 164215 (2009). xii, 8, 12, 114

[15] C. Pfleiderer, C. Thessieu, A. N. Stepanov, G. Lapertot, and M. Couach, Physica B **230**, 576 (1997).

[16] S. Mühlbauer, B. Binz, F. Jonietz, C. Pfleiderer, A. Rosch, A. Neubauer, R. Georgii, and P. Böni, Science **323**, 915 (2009). xiv, 8, 28, 29, 30, 31, 103

[17] K. Kadowaki, K. Okuda, and M. Date, J. Phys. Soc. Japan **51**, 2433 (1982). 9

[18] P. Pedrazzini, H. Wilhelm, D. Jaccard, T. Jarlborg, M. Schmidt, M. Hanfland, L. Akselrud, H. Q. Yuan, U. Schwarz, Y. Grin, et al., Phys. Rev. Lett. **98**, 047204 (2007). 9

[19] Y. Onose, N. Takeshita, C. Terakura, H. Takagi, and Y. Tokura, Phys. Rev. B **72**, 224431 (2005). 9, 69, 99, 108

[20] S. Seki, X. Z. Yu, S. Ishiwata, and Y. Tokura, Science **336**, 198 (2012). xii, 9, 13, 29, 103, 104

[21] Y. Togawa, T. Koyama, K. Takayanagi, S. Mori, Y. Kousaka, J. Akimitsu, S. Nishihara, K. Inoue, A. S. Ovchinnikov, and J. Kishine, Phys. Rev. Lett. **108**, 107202 (2012). xiv, 9, 12, 21, 26, 27, 66, 69, 84, 88, 93, 122

[22] D. Wright and N. Mermin, Rev. Mod. Phys. **61**, 385 (1989). 10, 33

[23] P. G. Gennes and J. Prost, *The Physics of Liquid Crystals* (Oxford University Press, New York, 1993). xv, 10, 32

[24] I. A. Fischer, Ph.D. thesis, Universität zu Köln (2006). xiii, 10, 18, 33, 34

[25] I. Fischer, N. Shah, and A. Rosch, Phys. Rev. B **77**, 024415 (2008). 10, 13

[26] A. Hamann, D. Lamago, T. Wolf, H. v. Löhneysen, and D. Reznik, Phys. Rev. Lett. **107**, 037207 (2011). xv, 10, 13, 33, 34, 35

[27] C. Pfleiderer and A. Rosch, Nature **465**, 880 (2010). xii, 11

[28] B. R. Holstein, Am. J. Phys. **57**, 1079 (1989). 11

[29] P. Bruno, V. K. Dugaev, and M. Taillefumier, Phys. Rev. Lett. **93**, 096806 (2004). 11

[30] A. Neubauer, C. Pfleiderer, B. Binz, A. Rosch, R. Ritz, P. G. Niklowitz, and P. Böni, Phys. Rev. Lett. **102**, 186602 (2009). 11, 123

[31] F. Jonietz, S. Mühlbauer, C. Pfleiderer, A. Neubauer, W. Münzer, A. Bauer, T. Adams, R. Georgii, P. Böni, R. . A. Duine, et al., Science **330**, 1648 (2010). 12, 123

[32] B. Roessli, J. Schefer, G. Petrakovskii, B. Ouladdiaf, M. Boehm, U. Staub, A. Vorotinov, and L. Bezmaternikh, Phys. Rev. Lett. **86**, 1885 (2001). xiii, 12, 21, 26, 104

[33] A. Zheludev, S. Maslov, G. Shirane, Y. Sasago, N. Koide, and K. Uchinokura, Phys. Rev. Lett. **78**, 4857 (1997). xiii, 12, 21, 25, 104, 111

[34] I. G. Bostrem, J.-i. Kishine, and A. S. Ovchinnikov, Phys. Rev. B **78**, 064425 (2008). 12, 24, 66, 92

[35] J.-i. Kishine, A. Ovchinnikov, and I. Proskurin, Phys. Rev. B **82**, 1 (2010). 12, 123

[36] J.-i. Kishine, I. V. Proskurin, and A. S. Ovchinnikov, Phys. Rev. Lett. **107**, 017205 (2011). 12, 21, 24, 66, 123

[37] P. Chandra, P. Coleman, J. A. Mydosh, and V. Tripathi, Nature **417**, 831 (2002). 12

[38] F. M. Grosche, P. Agarwal, S. R. Julian, N. J. Wilson, R. K. W. Haselwimmer, S. J. S. Lister, N. D. Mathur, F. V. Carter, S. S. Saxena, and G. G. Lonzarich, J. Phys.: Condens. Mat. **12**, L533 (2000). 12

[39] E. Dagotto, T. Hotta, and A. Moreo, Phys. Rep. **344**, 1 (2001). 12

[40] J. Zaanen, O. Y. Osman, H. V. Kruis, Z. Nussinov, and J. Tworzydlo, Philosophical Magazine B **81**, 1485 (2001).

[41] S. Sachdev, Rev. Mod. Phys. **75**, 913 (2003).

[42] S. A. Kivelson, I. P. Bindloss, E. Fradkin, V. Oganesyan, J. M. Tranquada, A. Kapitulnik, and C. Howald, Rev. Mod. Phys. **75**, 1201 (2003). 12

[43] C. Pfleiderer, D. Reznik, L. Pintschovius, H. v. Löhneysen, M. Garst, and A. Rosch, Nature **427**, 227 (2004). 12

[44] B. Binz, A. Vishwanath, and V. Aji, Phys. Rev. Lett. **96**, 207202 (2006). 13

[45] C. Pfleiderer, J. Phys.: Condens. Matter **17**, S987 (2005). xiii, 13

[46] H. Katsura, N. Nagaosa, and A. V. Balatsky, Phys. Rev. Lett. **95**, 057205 (2005). 13

[47] I. A. Sergienko and E. Dagotto, Phys. Rev. B **73**, 1 (2006).

[48] S. Picozzi, K. Yamauchi, B. Sanyal, I. Sergienko, and E. Dagotto, Phys. Rev. Lett. **99**, 227201 (2007). 13

[49] J. H. Yang, Z. L. Li, X. Z. Lu, M.-H. Whangbo, S.-H. Wei, X. G. Gong, and H. J. Xiang, Phys. Rev. Lett. **109**, 107203 (2012). 14

[50] P. M. Chaikin and T. C. Lubensky, *Principles of condensed matter physics* (Cambridge University Press, Cambridge, 1995). 16

[51] F. Schwabl, *Statistical Mechanics*, vol. 2 of *Statistical Mechanics* (Springer, Heidelberg, 2006). 16

[52] O. Nakanishi, A. Yanase, A. Hasegawa, and M. Kataoka, Solid State Commun. **35**, 995 (1980). 17

[53] L. Debnath, in *Nonlinear Partial Differential Equations for Scientists and Engineers* (Springer, Boston, 2012). 19

[54] C. S. Gardner, J. M. Greene, M. D. Kruskal, and R. M. Miura, Phys. Rev. Lett. **19**, 1095 (1967). 19

[55] J. S. Russell, Tech. Rep., British Assoc. for the Adv. of Science (1937). 19

[56] J. S. Russell, Royal Society of Edinburgh, Transactions **14**, 47 (1838). 19

[57] N. J. Zabusky and M. D. Kruskal, Phys. Rev. Lett. **15** (1965). 19

[58] A. T. Flippov, *The Versatile Soliton* (Birkhauser, Boston, 2000). 19, 91

[59] A. J. Heeger, S. Kivelson, J. R. Schreiffer, and W. P. Su, Rev. Mod. Phys. **60**, 781 (1988). 19

[60] A. S. Davydov, Physica 3D **1 & 2**, 1 (1981). 19

[61] J. M. Hyman, D. W. Mclaughlin, and A. C. Scott, Physica 3D **1 & 2**, 23 (1981). 19

[62] S. Aubry and P. Y. Le Daeron, Physica **8D**, 381 (1983). 19

[63] E. Trías, J. J. Mazo, and T. P. Orlando, Phys. Rev. Lett. **84**, 741 (2000). 19

[64] A. J. Sievers and S. Takeno, Rhys. Rev. Lett. **61**, 970 (1988). 19

[65] H. Haus and W. Wong, Rev. Mod. Phys. **68**, 423 (1996). 19

[66] A. R. Bishop, J. A. Krumhansl, and S. E. Trullinger, Physica D **1**, 1 (1980). 19

[67] H. J. Mikeska, J. Phys. C: Solid State Phys. **11**, L29 (1978). 19, 20

[68] K. Kjems and M. Steiner, Phys. Rev. Lett. **41**, 1137 (1978). 19, 21

[69] J. P. Boucher, L. P. Regnault, J. Rossat-Mignod, J. P. Renard, J. Bouillot, and W. G. Stirling, Solid State Commun. **33**, 171 (1980). 19, 20, 21

[70] J. P. Boucher, J. Appl. Phys. **52**, 1956 (1981). 19

[71] L. J. de Jongh, J. Appl. Phys. **53**, 8018 (1982). xiii, 20

[72] K. M. Leugn, D. W. Hone, D. L. Mills, P. S. Riseborough, and S. E. Trullinger, Phys. Rev. B **21**, 4017 (1980). 20

[73] U. Enz, Helv. Phys. Acta **37**, 245 (1964). 20

[74] I. E. Dzyaloshinskii, Sov. Phys. JETP **20**, 665 (1965). 21, 72, 91, 92, 104

[75] Y. A. Izyumov and V. M. Laptev, Sov. Phys. JETP **58**, 1267 (1983). 21, 72, 92

[76] J. Kishine, K. Inoue, and Y. Yoshida, Prog. Theor. Phys. Suppl. **159**, 82 (2005). 21, 24, 65, 91, 92, 93, 99

[77] T. H. R. Skyrme, Proc. Roy. Soc. Lond. A **260**, 127 (1961). 27

[78] T. H. R. Skyrme, Nucl. Phys. **31**, 556 (1962). 27

[79] S. L. Sondhi, A. Karlhede, S. A. Kivelson, and E. H. Rezayi, Phys. Rev. B **47**, 16419 (1993). 27

[80] G. E. Volovik, *The Universe in a Helium Droplet* (Clarendon Press, Oxford, 2003). 27

[81] L. S. Leslie, A. Hansen, K. C. Wright, B. M. Deutsch, and N. P. Bigelow, Phys. Rev. Lett. **103**, 250401 (2009). 28

[82] J.-y. Choi, W. J. Kwon, and Y.-i. Shin, Phys. Rev. Lett. **108**, 035301 (2012). 28

[83] S. D. Bader, Rev. Mod. Phys. **78**, 1 (2006). 28

[84] T. Shinjo, T. Okuno, R. Hassdorf, K. Shigeto, and T. Ono, Science **289**, 930 (2000). 28

[85] T. Adams, S. Mühlbauer, A. Neubauer, W. Münzer, F. Jonietz, R. Georgii, B. Pedersen, P. Böni, A. Rosch, and C. Pfleiderer, J. Phys.: Conf. Ser. **200**, 032001 (2010). xiv, 29, 30

[86] W. Münzer, A. Neubauer, T. Adams, S. Mühlbauer, C. Franz, F. Jonietz, R. Georgii, P. Böni, B. Pedersen, M. Schmidt, et al., Phys. Rev. B **81**, 041203 (2010). 29, 103

[87] X. Z. Yu, Y. Onose, N. Kanazawa, J. H. Park, J. H. Han, Y. Matsui, N. Nagaosa, and Y. Tokura, Nature **465**, 901 (2010). xiv, 29, 30, 31

[88] X. Z. Yu, N. Kanazawa, Y. Onose, K. Kimoto, W. Z. Zhang, S. Ishiwata, Y. Matsui, and Y. Tokura, Nat. Mater. **10**, 106 (2011). 29, 31, 103

[89] E. Moskvin, S. Grigoriev, V. Dyadkin, H. Eckerlebe, M. Baenitz, M. Schmidt, and H. Wilhelm, Phys. Rev. Lett. **110**, 077207 (2013). 29

[90] C. Pfleiderer, T. Adams, A. Bauer, W. Biberacher, B. Binz, F. Birkelbach, P. Böni, C. Franz, R. Georgii, M. Janoschek, et al., J. Phys.: Condens. Matter **22**, 164207 (2010). 29, 31, 103

[91] T. Adams, A. Chacon, M. Wagner, A. Bauer, G. Brandl, B. Pedersen, H. Berger, P. Lemmens, and C. Pfleiderer, Phys. Rev. Lett. **108**, 237204 (2012). 29, 99, 108

[92] A. N. Bogdanov and D. A. Yablonskii, Sov. Phys. JEPT **68**, 101 (1989). 30, 31, 32, 45, 103

[93] A. N. Bogdanov, M. V. Kudinov, and D. A. Yablonskii, Sov. Phys. Solid State **31**, 1707 (1989). 45

[94] A. N. Bogdanov and D. A. Yablonskii, Sov. Phys. JEPT **69**, 142 (1989). 30, 31, 32, 103

[95] A. Bogdanov and A. Hubert, J. Magn. Magn. Mater **138**, 255 (1994). 31, 65, 103

[96] G. L. Squires, *Introduction to the thoery of thermal neutron scattering* (Cambridge University Press, London, 1978). xv, 38

[97] D. L. Price and K. Skold, *Methods of Experimental Physics-Neutron Scattering-Part A* (Academic Press, Inc., Orlando, 1986). 38, 39

[98] T. Chatterji, *Neutron Scattering From Magnetic Materials* (Elsevier, New York, 2006). xv, 43

[99] A. Furrer, J. Mesot, and T. Strassle, *Neutron Scattering in Condensed Matter Physics* (World Scientific, New Jersey, 2010). xv, 43

[100] H. Völlenkle, A. Preisinger, H. Nowotny, and A. Wittmann, Z. Kristallogr. **124**, 9 (1967). 45, 48, 49, 62

[101] V. L. Zagryazhskii, P. V. Gel'd, and A. K. Shtol'ts, Soviet Physics Journal **11**, 23 (1968). 45, 50, 54, 57

[102] M. Kolenda, J. Stoch, and A. Szytula, J. Magn. Magn. Mater **20**, 99 (1980). 45

[103] P. Pécheur, G. Toussaint, H. Kenzari, B. Malaman, and R. Welter, J. Alloy. Compd. **262-263**, 363 (1997). 46, 50, 62

[104] T. Caillat, J.-P. Fleurial, and A. Borshchevsky, J. Alloy. Compd. **252**, 12 (1997). 46, 48, 57

[105] A. Migliori and J. D. Maynard, Rev. Sci. Instrum. **76**, 121301 (2005). 48

[106] D. C. Fredrickson, S. Lee, and R. Hoffmann, Inorg. Chem. **43**, 6159 (2004). 48

[107] E. P. Wohlfarth, Physica B + C **91**, 305 (1977). 51

[108] E. P. Wohlfarth, J. Appl. Phys. **39**, 1061 (1968).

[109] D. M. Edwards and E. P. Wohlfarth, Proc. Roy. Soc. A. **303**, 127 (1968). 51

[110] A. Arrott and J. E. Noakes, Phys. Rev. Lett. **19**, 786 (1967). 51

[111] M. K. Chattopadhyay, P. Arora, and S. B. Roy, J. Phys.:Condens. Matter. **21**, 296003 (2009). 51, 69, 99, 108

[112] H. Ohta and K. Yoshimura, Phys. Rev. B **79**, 1 (2009). 51

[113] Y. Takahashi, J. Phys. Soc. Japan **55**, 3553 (1986). 51, 53

[114] K. Shimizu, H. Maruyama, H. Yamazaki, and H. Watanabe, J. Phys. Soc. Japan **59**, 305 (1990). 53

[115] S. C. Ho, I. Maartense, and G. Williams, J. Phys. F:Met. Phys **699** (1981). 53

[116] M. Vannette, A. Sefat, S. Jia, S. Law, G. Lapertot, S. Budko, P. Canfield, J. Schmalian, and R. Prozorov, J. Magn. Magn. Mater **320**, 354 (2008). 53

[117] C. Thessieu, C. Pfleiderer, A. N. Stepanov, and J. Flouquet, J. Phys.: Condens. Mat. **9**, 6677 (1997). 53, 54

[118] H. Wilhelm, M. Baenitz, M. Schmidt, U. K. Rößler, A. A. Leonov, and A. N. Bogdanov, Phys. Rev. Lett. **107**, 127203 (2011). 53, 54, 104, 114

[119] P. Mohn and G. Hilscher, Phys. Rev. B **40**, 9126 (1989). 55, 56

[120] J. G. Huber, M. B. Maple, and D. Wohlleben, Solid State Commun. **16**, 211 (1975). 56

[121] S. Ogawa and N. Sakamoto, J. Phys. Soc. Japan **22**, 1214 (1967). 56

[122] P. Mohn, R. Merlin, and H. Stormer, *Magnetism in the Solid State* (Springer, Heidelberg, 2006). 56

[123] E. Schreiber, O. L. Anderson, and N. Soga, *Elastic constants and their measurement* (McGraw-Hill, New York, 1973). 59

[124] O. L. Anderson, J. Phys. Chem. Solids **24**, 909 (1963). 59

[125] Y. P. Varshni, Phys. Rev. B **2**, 3952 (1970). 61

[126] S. C. Lakkad, J. Appl. Phys. **42**, 4277 (1971). 61

[127] U. Kawald, O. Mitze, H. Bach, J. Pelzl, and G. A. Saunders, J. Phys.: Condens. Matter **6**, 9697 (1994). 61

[128] P. Blaha, K. Schwarz, G. K. H. Madsen, D. Kvasnicka, and J. Luitz, *WIEN2k, An Augmented Plane Wave + Local Orbitals Program for Calculating Crystal Properties* (Karlheinz Schwarz, Techn. Universitat Wein, Austria, 2001). 61, 84

[129] J. Perdew, K. Burke, and M. Ernzerhof, Phys. Rev. Lett. **77**, 3865 (1996). 61, 84

[130] J. F. Janak, Phys. Rev. B **16**, 255 (1977). 62, 87

[131] B. Van Laar, J. Solid State Chem. **3**, 154 (1971). 65

[132] F. Hulliger and E. V. A. Pobitschka, J. Solid State Chem. **1**, 117 (1970). 65, 66, 67

[133] T. Miyadai, K. Kikuchi, H. Kondo, S. Sakka, K. Arai, and Y. Ishikawa, J. Phys. Soc. Japan **52**, 1394 (1983). 65, 66, 67, 68, 69, 84, 93, 96

[134] S. S. P. Parkin and R. H. Friend, Philosophical Magazine B **41**, 96 (1980). 66, 68, 76, 80, 93

[135] S. S. P. Parkin and R. H. Friend, Physica B + C **99**, 219 (1980). 65, 66

[136] Y. Kousaka, Y. Nakao, J. Kishine, M. Akita, K. Inoue, and J. Akimitsu, Nucl. Instrum. Methods Phys. Res., Sect. A **600**, 250 (2009). 65

[137] J.-i. Kishine and A. S. Ovchinnikov, Phys. Rev. B **79**, 220405(R) (2009). 66

[138] N. S. Kiselev, A. N. Bogdanov, R. Schäfer, and U. K. Rößler, J. Phys. D: Appl. Phys. **44**, 392001 (2011). 66

[139] T. Moriya and T. Miyadai, Solid State Commun. **42**, 209 (1982). 66

[140] A. R. Beal, in *Intercalated Layered Materials*, edited by F. A. Levy (D. Reidel Publishing Company, Dordecht, Holland, 1979), pp. 251–305. 68, 93

[141] S. S. P. Parkin and R. H. Friend, Philosophical Magazine B **41**, 65 (1980). 68, 69

[142] L. Ludgren, O. Beckman, V. Attia, S. P. Bhattacheriee, and M. Richardson, Phys. Scripta. **1**, 69 (1970). 69, 99, 108

[143] U. K. Rößler, Private Communication. 73

[144] R. A. Steeman, E. Frikkee, S. A. M. Mentink, A. A. Menovsky, G. J. Nieuwenhuys, and J. A. Mydosh, J. Phys.: Condens. Matter **2**, 4059 (1990). 76

[145] M. Barati, W. R. Datars, T. R. Chien, C. V. Stager, and J. D. Garrett, Phys. Rev. B **48**, 16926 (1993). 76

[146] T. T. M. Palstra, A. A. Menovsky, and J. A. Mydosh, Phys. Rev. B **33**, 6527 (1986). 76

[147] C. Kittel, *Introduction to Solid State Physics* (John Wiley & Sons, Inc, New York, 2005). 80

[148] M. A. McGuire, A. D. Christianson, A. S. Sefat, B. C. Sales, M. D. Lumsden, R. Jin, E. A. Payzant, D. Mandrus, Y. Luan, V. Keppens, et al., Phys. Rev. B **78**, 094517 (2008). 81

[149] L. J. Li, Y. K. Luo, Q. B. Wang, H. Chen, Z. Ren, Q. Tao, Y. K. Li, X. Lin, M. He, Z. W. Zhu, et al., New J. Phys. **11**, 025008 (2009). 81

[150] S. S. P. Parkin and R. H. Friend, Philosophical Magazine **35**, 1269 (1977). 93, 123

[151] B. C. Chakoumakos, H. Cao, F. Ye, A. D. Stoica, M. Popovici, M. Sundaram, W. Zhou, J. S. Hicks, G. W. Lynn, and R. A. Ridel, J. Applied Cryst. **55**, 655 (2011). 94

[152] L. M. DeBeer-Schmitt, Ph.D. thesis, Notre Dame University (2008). 94

[153] S. Mühlbauer, S. N. Gvasaliya, E. Pomjakushina, and A. Zheludev, Phys. Rev. B **84**, 180406 (2011). 104

[154] S. Mühlbauer, S. Gvasaliya, E. Ressouche, E. Pomjakushina, and A. Zheludev, Phys. Rev. B **86**, 024417 (2012). 104, 115, 119

[155] M. D. Lumsden, B. C. Sales, D. Mandrus, S. E. Nagler, and J. R. Thompson, Phys. Rev. Lett. **86**, 159 (2001). 104, 105, 106, 108, 119

[156] C. Thessieu, C. Pfleiderer, A. N. Stepanov, and J. Flouquet, J. Phys.: Condens. Matter **9**, 6677 (1997). 104

[157] J. Galy and A. Carpy, Acta Crystallogr. **B31**, 1794 (1975). 105

[158] B. C. Chakoumakos, R. Custelcean, T. Kamiyama, K. Oikawa, B. C. Sales, and M. .D Lumsden, J. Solid State Chem. **180**, 812 (2007). 105

[159] B. C. Sales, M. D. Lumsden, S. E. Nagler, D. Mandrus, and R. Jin, Physical Review Letters **88**, 095901 (2002). 105

[160] J. Choi, Z. Zhu, J. Musfeldt, G. Ragghianti, D. Mandrus, B. Sales, and J. Thompson, Physical Review B **65**, 054101. 105

[161] M. D. Lumsden, S. E. Nagler, B. C. Sales, D. A. Tennant, D. F. McMorrow, S.-H. Lee, and S. Park, Phys. Rev. B **74**, 214424 (2006). 107

[162] A. Zheludev, G. Shirane, Y. Sasago, N. Kiode, and K. Uchinokura, Phys, Rev. B **54**, 15163 (1996). 111

[163] A. R. King and D. Paquette, Phys. Rev. Lett. **30**, 662 (1973). 113

[164] N. J. Ghimire, M. A. McGuire, and D. Mandrus, *(unpublished)*. 114

[165] A. B. Borisov, J.-i. Kishine, I. G. Bostrem, and A. S. Ovchinnikov, Phys. Rev. B **79**, 134436 (2009). 123

[166] T. Hahn, ed., *International Tables for Crystallography, Vol. A: Space-Group Symmetry*, (2001). 141

# Appendix

# Appendix A

# Table of space groups

**Table A.1:** Space groups in 3 dimension

| Crystal system | Point group | | N/NC* | Space group number | Space groups (International short) |
|---|---|---|---|---|---|
| | Hermann-Maguin | Schönflies | | | |
| Triclinic | 1 | $C_1$ | NC | 1 | P1 |
| | $\bar{1}$ | $C_i$ | | 2 | $P\bar{1}$ |
| Monoclinic | 2 | $C_2$ | NC | 3-5 | P2, $P2_1$, C2 |
| | m | $C_s$ | N | 6-9 | Pm, Pc, Cm, Cc |
| | 2/m | $C_{2h}$ | | 10-15 | P2/m, $P2_1$/m, C2/m, P2/c, $P2_1$/c, C2/c |
| Orthorhombic | 222 | $D_2$ | NC | 16-24 | P222, $P222_1$, $P2_12_12$, $P2_12_12_1$, $C222_1$, C222, F222, I222, $I2_12_12_1$ |
| | mm2 | $C_{2\nu}$ | N | 25-46 | Pmm2, $Pmc2_1$, Pcc2, $Pma2$, $Pca2_1$, Pnc2, $Pmn2_1$, Pba2, $Pna2_1$, Pnn2, Cmm2, $Cmc2_1$, Ccc2, Amm2, Aem2, Ama2, Aea2, Fmm2, Fdd2, Imm2, Iba2, Ima2 |

**Table A.1:** Space groups in 3 dimension (cont.)

| Crystal system | Point group | | N/NC* | Space group number | Space groups (International short) |
|---|---|---|---|---|---|
| | Hermann-Maguin | Schönflies | | | |
| Orthorhombic | mmm | $D_{2h}$ | | 47-74 | Pmmm, Pnnn, Pccm, Pban, Pmma, Pnna, Pmna, Pcca, Pbam, Pccn, Pbcm, Pnnm, Pmmn, Pbcn, Pbca, Pnma, Cmcm, Cmce, Cmmm, Cccm, Cmme, Ccce, Fmmm, Fddd, Immm, Ibam, Ibca, Imma |
| Tetragonal | 4 | $C_4$ | NC | 75-80 | P4, $P4_1$, $P4_2$, $P4_3$, I4, $I4_1$ |
| | $\bar{4}$ | $S_4$ | N | 81-82 | $P\bar{4}$, $I\bar{4}$ |
| | 4/m | $C_{4h}$ | | 83-88 | P4/m, $P4_2$/m, P4/n, $P4_2$/n, I4/m, $I4_1$/a |
| | 422 | $D_4$ | NC | 89-98 | P422, $P42_12$, $P4_122$, $P4_12_12$, $P4_222$, $P4_22_12$, $P4_322$, $P4_32_12$, I422, $I4_122$ |
| | 4mm | $C_{4\nu}$ | N | 99-110 | P4mm, P4bm, $P4_2$cm, $P4_2$nm, P4cc, P4nc, $P4_2$mc, $P4_2$bc, I4mm, I4cm, $I4_1$md, $I4_1$cd |
| | $\bar{4}$2m | $D_{2d}$ | N | 111-122 | $P\bar{4}2m$, $P\bar{4}2c$, $P\bar{4}2_1m$, $P\bar{4}2_1c$, $P\bar{4}m2$, $P\bar{4}c2$, $P\bar{4}b2$, $P\bar{4}n2$, $I\bar{4}m2$, $I\bar{4}c2$, $I\bar{4}2m$, $I\bar{4}2d$ |
| | 4/mmm | $D_{4h}$ | | 123-142 | P4/mmm, P4/mcc, P4/nbm, P4/nnc, P4/mbm, P4/mnc, P4/nmm, P4/ncc, $P4_2$/mmc, $P4_2$/mcm, $P4_2$/nbc, $P4_2$/nnm, $P4_2$/mbc, $P4_2$/mnm, $P4_2$/nmc, $P4_2$/ncm, I4/mmm, I4/mcm, $I4_1$/amd, $I4_1$/acd |

**Table A.1:** Space groups in 3 dimension (cont.)

| Crystal system | Point group | | N/NC* | Space group number | Space groups (International short) |
|---|---|---|---|---|---|
| | Hermann-Maguin | Schönflies | | | |
| Trigonal | 3 | $C_3$ | NC | 143-146 | P3, $P3_1$, $P3_2$, R3 |
| | $\bar{3}$ | $C_{3i}$ | | 147-148 | $P\bar{3}$, $R\bar{3}$ |
| | 32 | $D_3$ | NC | 149-155 | P312, P321, $P3_112$, $P3_121$, $P3_212$, $P3_221$, R32 |
| | 3m | $C_{3\nu}$ | N | 156-161 | P3m1, P31m, P3c1, P31c, R3m, R3c |
| | $\bar{3}$m | $D_{3d}$ | | 162-167 | $P\bar{3}1$m, $P\bar{3}1$c, $P\bar{3}$m1, $P\bar{3}$c1, $R\bar{3}$m, $R\bar{3}$c |
| Hexagonal | 6 | $C_6$ | NC | 168-173 | P6, $P6_1$, $P6_5$, $P6_2$, $P6_4$, $P6_3$ |
| | $\bar{6}$ | $C_{3h}$ | N | 174 | $P\bar{6}$ |
| | 6/m | $C_{6h}$ | | 175-176 | P6/m, $P6_3$/m |
| | 622 | $D_6$ | NC | 177-182 | P622, $P6_122$, $P6_522$, $P6_222$, $P6_422$, $P6_322$ |
| | 6mm | $C_{6\nu}$ | N | 183-186 | P6mm, P6cc, $P6_3$cm, $P6_3$mc |
| | $\bar{6}$m2 | $D_{3h}$ | N | 187-190 | $P\bar{6}$m2, $P\bar{6}$c2, $P\bar{6}2$m, $P\bar{6}2$c |
| | 6/mmm | $D_{6h}$ | | 191-194 | P6/mmm, P6/mcc, $P6_3$/mcm, $P6_3$/mmc |
| Cubic | 23 | T | NC | 195-199 | P23, F23, I23, $P2_13$, $I2_13$ |
| | m$\bar{3}$ | $T_h$ | | 200-206 | Pm$\bar{3}$, Pn$\bar{3}$, Fm$\bar{3}$, Fd$\bar{3}$, Im$\bar{3}$, Pa$\bar{3}$, Ia$\bar{3}$ |
| | 432 | O | NC | 207-214 | P432, $P4_232$, F432, $F4_132$, I432, $P4_332$, $P4_132$, $I4_132$ |
| | $\bar{4}$3m | $T_d$ | N | 215-220 | $P\bar{4}$3m, $F\bar{4}$3m, $I\bar{4}$3m, $P\bar{4}$3n, $F\bar{4}$3c, $I\bar{4}$3d |
| | m$\bar{3}$m | $O_h$ | | 221-230 | Pm$\bar{3}$m, Pn$\bar{3}$n, Pm$\bar{3}$n, Pn$\bar{3}$m, Fm$\bar{3}$m, Fm$\bar{3}$c, Fd$\bar{3}$m, Fd$\bar{3}$c, Im$\bar{3}$m, Ia$\bar{3}$d |

**N stands for noncentrosymmetric and NC stands for noncentrosymmetric and chiral. All others have a center of symmetry. Source: International tables for crystallography, volume A* [166].

# List of publications and patent

- Ferromagnetism in $ZrFe_{12-x}Al_x$ and $HfFe_{12-x}Al_x$ (x = 6.0, 6.5, 7.0), Michael A. McGuire, Nirmal Ghimire, and David J. Singh, J. Appl. Phys. **111**, 093918 (2012).

- Complex itinerant ferromagnetism in noncentrosymmetric $Cr_{11}Ge_{19}$, N. J. Ghimire, M. A. McGuire, D. S. Parker, B. C. Sales, J.-Q. Yan, V. Keppens, M. Koehler, R. M. Latture, and D. Mandrus, Phys. Rev. B **85**, 224405 (2012).

- Hard ferromagnetism in melt-spun $Hf_2Co_{11}B$ alloys, Michael A. McGuire, Orlando Rios, Nirmal J. Ghimire, and Michael Koehler, Appl. Phys. Lett. **101**, 202401 (2012).

- Magneitc phase transition in chiral helimagnet $Cr_{1/3}NbS_2$, N. J. Ghimire, M. A. McGuire, D. S. Parker, B. Sipos, S. Tang, J.-Q. Yan, B. C. Sales, and D. Mandrus, Phys. Rev. B **85**, 104403 (2013).

- Electrical control of neutral and charge excitons in a monolayer semiconductor, Jason S. Ross, Sanfeng Wu, Hongyi Yu, Nirmal J. Ghimire, Aaron M. Jones, Grant Aivazian, Jiaqiang Yan, David G. Mandrus, Di Xiao, Wang Yao & Xiaodong Xu, Nature Commus. **4**, 1471 (2013).

- One provisional patent filed.

# Vita

Nirmal was born in the western district Lamjung of the Himalayan country Nepal. He completed his bachelor's and master's degrees in physics from Tribhuvan University in Kathmandu. He then worked as a lecturer of physics, teaching undergraduate physics and materials science courses in Nepal for about two years. In August 2008 he came to Knoxville as a graduate student in Department of Physics and Astronomy at the University of Tennessee. He joined professor David Mandrus's research group in the spring of 2010. In addition to his dissertation research, he also worked in a project involving the search for new rare-earth-free permanent magnets under the supervision of Dr. Michael McGuire in Correlated Electron Materials group at Oak Ridge National Laboratory. He is graduating with PhD degree in August 2013.